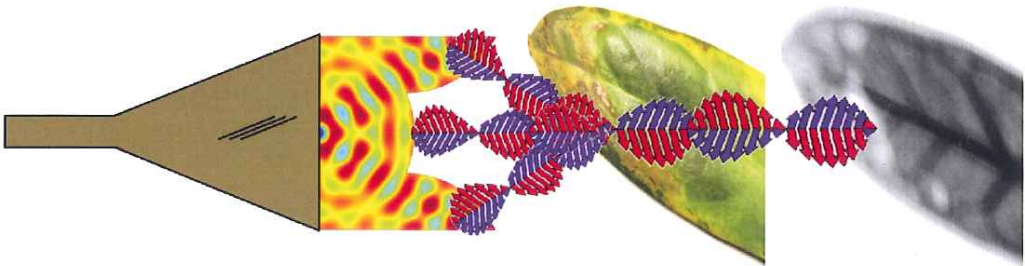


Diss. sv. 6620



Photonic THz Generation and Quasioptical Integration for Imaging Applications

BIDDUT BANIK

Physical Electronics Laboratory
Department of Microtechnology and Nanoscience
CHALMERS UNIVERSITY OF TECHNOLOGY
Göteborg, Sweden 2009

THESIS FOR THE DEGREE OF DOCTOR OF PHILOSOPHY

Photonic THz Generation and Quasioptical Integration for Imaging Applications

Biddut Banik



Physical Electronics Laboratory
Department of Microtechnology and Nanoscience
Chalmers University of Technology
SE-412 96 Göteborg, Sweden 2009

Photonic THz Generation and Quasioptical Integration for Imaging Applications

BIDDUT BANIK

ISBN 978-91-7385-319-4

© Biddut Banik, 2009

Doktorsavhandlingar vid
Chalmers tekniska högskola
Ny serie nr 3000
ISSN 0346-718X

ISSN 1652-0769
Technical Report MC2-151
Physical Electronics Laboratory

Department of Microtechnology and Nanoscience – MC2
Chalmers University of Technology
SE-412 96 Göteborg, Sweden
Phone: +46 (0) 31 772 1000

Cover: THz imaging of a partially dead leaf employing a catadioptric lens coupled WR-10 horn antenna in a transmission-mode CW imaging setup at 108 GHz.

Printed by
Chalmers Reproservice,
Göteborg, Sweden
September, 2009.

Abstract

This thesis deals with the analysis and optimisation of the uni-travelling-carrier photodiode (UTC-PD) for continuous-wave generation in terahertz (THz) frequency range. Photonic THz generation using UTC-PDs is extremely promising as it offers wide tunability, adequate output power and room temperature operation. Furthermore, a novel and compact catadioptric lens is proposed and investigated for realising compact sensing systems. Radiating elements and components can be physically coupled to the lens in order to achieve short-range focusing and sensing ability.

Using physical device modelling, the limitations and optimisation of InGaAs/InP based UTC-PDs for attaining higher bandwidth as well as higher output power are discussed. A hydrodynamic (HD) carrier transport model is used to analyse the device. Optimising for output power requires trade-offs involving the epitaxial layer design, optical coupling, circuit design and antenna design. An example of UTC-PD epitaxial layer optimisation for continuous-wave THz generation at 340 GHz is shown using the HD model. The output power and the optimum embedding impedance for the UTC-PD, as a function of device parameters, are also studied at different optical injection levels. Several plausible integration schemes and antenna design examples at 340 GHz are explored.

A novel catadioptric lens, suitable for microwave and terahertz applications, is presented. The focusing property of the lens is investigated using 3D full-wave electromagnetic solvers. The proposed catadioptric lens is designed and fabricated from Delrin and Macor. Simulation and characterisation results are presented at microwave and terahertz frequencies (108 GHz). The results show that although being a few wavelengths (λ) in dimension, the catadioptric lens provides short-range focusing in the close vicinity ($\sim\lambda$) and therefore provides a compact solution for short-range imaging systems. Finally, several short-range imaging examples at 108 GHz, employing the catadioptric lenses, are also presented and discussed.

Keywords: III-V semiconductors, catadioptric lens, dielectric loaded antennas, lens antennas, microwave imaging, millimetre wave and submillimetre wave generation, millimetre wave and submillimetre wave imaging, nondestructive evaluation, photomixers, semiconductor device modelling, uni-travelling-carrier photodiodes, terahertz imaging, terahertz sources.

List of appended papers

The thesis is based on the following papers:

- [A] B. Banik, J. Vukusic, H. Hjelmgren, and J. Stake, "Optimization of the UTC-PD Epitaxy for Photomixing at 340 GHz," *International Journal of Infrared and Millimeter Waves*, vol. 29, pp. 914-923, 2008.
- [B] B. Banik, J. Vukusic, and J. Stake, "Millimeter Wave Characterization of a Catadioptric Lens for Imaging Applications", *to appear in IEEE Microwave and Wireless Component Letters*, Nov, 2009.
- [C] B. Banik, J. Vukusic, and J. Stake, "Microwave Characterization of an Antenna-Coupled Catadioptric Lens", *submitted to IEEE Antennas and Wireless Propagation Letters*.
- [D] B. Banik, J. Vukusic, and J. Stake, "Catadioptric Dielectric Lens for Imaging Applications," *33rd International Conference on Infrared, Millimeter and Terahertz Waves*, pp. 255-256, 2008.
- [E] B. K. Banik, J. Vukusic, H. Merkel, and J. Stake, "A novel catadioptric dielectric lens for microwave and terahertz applications," *Microwave and Optical Technology Letters*, vol. 50, pp. 416-419, 2008.

Other papers

The following publications are not included due to the overlap in contents or the contents are beyond the scope of this thesis:

- [R1] B. Banik, J. Vukusic, H. Hjelmgren, H. Sunnerud, A. Wiberg, and J. Stake, "UTC-PD Integration for Submillimetre-wave Generation", *19th International Symposium on Space Terahertz Technology*, pp. P7-1, 2008.
- [R2] B. Banik, J. Vukusic, H. Hjelmgren, H. Sunnerud, A. Wiberg, and J. Stake, "High Power Photonic MW/THz Generation Using UTC-PD". *GigaHertz Symposium*, pp. 45, 2008.
- [R3] B. Banik, J. Vukusic, and J. Stake, "Design of Antenna Integrated Photomixers and Catadioptric Lenses for Emerging THz Applications", *ANSYS Regional Conference*, 2008.

- [R4] J. Stake, H. Zirath, A. Tang, B. Banik, V. Drakinskiy, P. Sobis, J. Vukusic, S. Cherednichenko, A. Emrich, S. Rudner, T. Bryllert, P. Siegel, “Terahertz technology and applications”, *International Symposium on Terahertz between Japan and Sweden*, 2008.
- [R5] M. R. Rafique, T. Ohki, B. Banik, H. Engseth, P. Linner and A. Herr, “Miniaturized superconducting microwave filters”, *Supercond. Sci. Technol.*, vol. 21, pp. 075004, 2008.
- [R6] B. Banik, J. Vukusic, S. Rahman, H. Sunnerud, J. Stake, “Development and Design of a 340 GHz Photomixer Source”, *18th International Symposium on Space THz Technology*, pp. 75, 2007.
- [R7] R. Rafique, P. Linner, B. Motlagh, B. Banik, T. Ohki, A. Herr, “Miniaturization of superconducting passive filters for on-chip applications”, *11th International Superconducting Electronics Conference*, pp. P-V09, 2007.
- [R8] B. Banik, H. Merkel, “Catadioptric Microlenses for Submillimeter and Terahertz Applications”, *17th International Symposium on Space Terahertz Technology*, pp. P2-16, 2006.
- [R9] B. Banik, H. Merkel, “VO₂ TES as Room Temperature THz Detectors”, *17th International Symposium on Space Terahertz Technology*, pp. P1-01, 2006.
- [R10] H. Merkel, B. Banik, V. Drakinskiy, “Twodimensionally distributed Model for HEB based on Random Phase Transitions”, *17th International Symposium on Space Terahertz Technology*, pp. TH3-8, 2006.
- [R11] H. Merkel, B. Banik, “Quantum Noise in Resistive Mixers”, *17th International Symposium on Space Terahertz Technology*, pp. P1-13, 2006.

Notations

A	Device area
C	Differential capacitance
D_e	Diffusivity of electrons in the absorption layer
f	Frequency
f_{3dB}	3-dB bandwidth
I_{ph}	Photocurrent
L_C	Length of the catadioptric portion
P_{inj}	Injected optical power
P_{THz}	THz power
R	Responsivity
R_A	Radiation resistance of the antenna
R_C	Radius of curvature of the catadioptric part
R_L	Radius of curvature of the hemispherical part
R_L	Radius of the lens
V_b	Bias voltage
V_r	Reverse Bias Voltage
V_{ri}	Built-in Voltage
v_{th}	Electron thermionic emission velocity
w	Width of the depleted layers
W_A	Absorption layer thickness
W_C	Collection layer thickness
ϵ_r	Dielectric Constant
η	Quantum efficiency
λ_0	Wavelength in free-space
λ_{del}	Wavelength in Delrin
λ_{MACOR}	Wavelength in Macor
λ_{si}	Wavelength in silicon
ν	Frequency
τ_A	Carrier travelling time in the Absorption layer
τ_C	Carrier travelling time in the collection layer
τ_{RC}	RC-time constant
τ_{tr}	Transit time
v_{os}	Overshoot velocity of the electrons

List of acronyms

μm	Micrometre
ADS	Advanced Design System
ALMA	Atacama Large Millimetre/submillimetre Array
BWO	Backward Wave Oscillator
CMOS	Complementary Metal Oxide Semiconductor
CPS	Coplanar Stripline
CPW	Coplanar Waveguide
CW	Continuous Wave
DD	Drift Diffusion
E-field	Electric-field
EM	Electromagnetic
FDTD	Finite-difference time-domain
FEL	Free Electron Laser
FEM	Finite Element Method
fF	Femto Farad
FIR	Far Infrared Laser
FMCW	Frequency Modulated Continuous-wave
GaAs	Gallium Arsenide
GHz	Gigahertz
GO	Geometrical Optics
HD	Hydrodynamic
HDTV	High-Definition Television
HFSS	High Frequency Structure Simulator
HPBW	Half Power Beam Width
InGaAs	Indium Gallium Arsenide
InP	Indium Phosphide
LD	Laser Diode
LO	Local Oscillator
LSI	Large-Scale Integration
LT-GaAs	Low-Temperature Grown GaAs
MHz	Megahertz
MSM	Metal-Semiconductor-metal
mil	Milli-inch (10^{-3} inch or $25.4 \mu\text{m}$)
mmw	Millimetre wave
MOM	Method Of Moment
MSL	Microstrip Line
MW	Microwave
NDE	Nondestructive evaluation
nm	Nanometre
PD	Photodiode
PDE	Partial differential equations
pF	Pico Farad
PIN	<i>p</i> -doped-intrinsic- <i>n</i> -doped (<i>p-i-n</i>)

pJ	Pico Joule
PO	Physical Optics
POM	Polyoxymethylene
ps	Pico second
QCL	Quantum Cascade Laser
SEM	Scanning Electron Microscope
SIS	Superconductor-Insulator-Superconductor
SMA	SubMiniature version A
SNR	Signal-to-noise ratio
submmw	Sub Millimetre wave
TCAD	Technology Computer Aided Design
TE	Transverse Electric
THz	Terahertz (10^{12} Hz)
UTC-PD	Uni-Travelling-Carrier Photodiode
VNA	Vector Network Analyser
VSWR	Voltage Standing Wave Ratio
WG	Waveguide
WLAN	Wireless Local Area Network

Table of contents

CHAPTER 1. INTRODUCTION	1
CHAPTER 2. PHOTONIC THZ GENERATION.....	5
2.1 UNI-TRAVELLING-CARRIER PHOTODIODE	6
2.1.1 Basic principles.....	7
2.1.2 Material and epitaxial structure	9
2.1.3 Equivalent circuit.....	10
2.1.4 Performance factors.....	10
2.1.5 Device fabrication.....	12
2.1.6 Parameter extraction	13
2.2 DEVICE MODELLING	14
2.2.1 Carrier transport modelling	14
2.2.2 Drift-Diffusion model.....	15
2.2.3 Hydrodynamic model	15
2.2.4 Thermodynamic model.....	16
2.2.5 Simulation results	16
2.3 DEVICE OPTIMISATION	18
2.3.1 Limiting factors and optimisation scopes.....	18
2.3.2 Device structure optimisation.....	19
2.4 OPTIMUM EMBEDDING IMPEDANCE.....	22
2.5 CIRCUIT AND DEVICE INTEGRATION.....	24
2.5.1 Circuit design.....	24
2.5.2 Antenna design	25
2.5.3 UTC-PD integrated antenna design examples.....	26
CHAPTER 3. QUASIOPTICAL INTEGRATION.....	31
3.1 QUASIOPTICAL COMPONENTS.....	32
3.2 THE CATADIOPTRIC LENS	33
3.3 DESIGN AND ANALYSIS OF THE CATADIOPTRIC LENS.....	33
3.3.1 Basic principles of the lens.....	33
3.3.2 3D EM analysis	35
3.3.3 Design issues	36
3.3.4 Lens fabrication	36
3.4 CHARACTERISATION TECHNIQUES	37
3.4.1 Microwave characterisation.....	39
3.4.2 Millimetre-wave characterisation	42
3.4.3 Thermal mapping.....	43

CHAPTER 4. IMAGING APPLICATIONS	45
4.1 INTRODUCTION	45
4.2 IMAGING SYSTEMS.....	46
4.3 A SHORT-RANGE IMAGING SYSTEM	47
4.4 IMAGING SYSTEM CHARACTERISATION	48
4.5 APPLICATION EXAMPLES	51
4.5.1 Microwave applications.....	51
4.5.2 Terahertz applications.....	53
CHAPTER 5. CONCLUSION AND FUTURE DIRECTIONS.....	57
REFERENCES.....	61

Chapter 1. Introduction

The 19th century is considered as a historical landmark in the electromagnetics area with the numerous discoveries and inventions by J.C. Maxwell, N. Tesla, A.S. Popov, J. C. Bose and many others. In 1896, Marconi was awarded the British patent “Improvements in transmitting electrical impulses and signals and in apparatus therefor”, for inventing the radio. After a year, he established the world's first radio station on the Isle of Wight, England. Contemporaneously, J.C. Bose carried out studies on plant physiology and other fields in India employing a type of spark gap generator to produce high frequency radiation. It took only about a century to find ourselves submerged in electromagnetic waves. From communication systems to imaging systems, from proximity detectors to security systems, the electromagnetic spectrum is being utilised for countless applications. This is especially true for the microwave (MW) regime which has been extensively utilised for communication, imaging and remote sensing. With the increasing demand for bandwidth and resolution, the MW regime does not seem to accommodate the fast pacing wide variety of applications.

Caught in between, the Terahertz (10^{12} hertz) frequency band is like the neglected middle child in the electromagnetic spectrum. Terahertz (THz) refers to the electromagnetic waves and radiation between 0.1 THz ($\lambda = 3$ mm, photon energy = 0.41 meV) and 10 THz ($\lambda = 30$ μ m, photon energy = 41 meV), a widely agreed-upon definition. The terahertz regime lies between the MW and far-infrared regions in the electromagnetic spectrum. The THz band partially covers the millimetre-wave frequencies (30 GHz – 300 GHz) and spans beyond the submillimetre-wave frequencies (300 GHz – 3 THz). Terahertz technology has been primarily used in the radio astronomy, high-resolution spectroscopy and remote sensing areas [1-3]. The interest in the terahertz technology is being fuelled by the fact that this range of frequencies accommodates unique physical phenomena with interesting characteristic features. Terahertz wavelengths are longer than infrared and optical radiation, so scattering is comparatively small. However, the terahertz wavelength is sufficiently short to achieve a submillimetre lateral resolution [4]. Terahertz imaging sensors bridge the gap between microwave radar and infrared camera.

Terahertz is able to penetrate most non-metallic and non-polar mediums. Terahertz systems are able to ‘see through’ concealing barriers such as packaging, clothing, shoes, baggage, etc in order to probe the potentially dangerous materials contained within. Terahertz radiation is non-ionising and the power levels used do not cause any detrimental effects. Many explosives, chemicals and biological agents have characteristic terahertz spectra. Therefore, terahertz systems can be used to identify those objects. Apparently, THz technology holds high potential for numerous “down to earth” applications [5] such as imaging, spectroscopy, nondestructive testing, stand-off detection of concealed weapons, explosives and narcotics [6, 7], automobile radar systems [8] and biomedical applications [9, 10].

Despite the exceptional potential, the THz region is commonly known as the THz-gap due to the lack of tunable, high power and room temperature sources and detectors. The atmospheric attenuation of THz radiation is also much stronger than for MW or infrared. Traditional electronic solid-state sources based on semiconductors, such as oscillators and amplifiers, are limited by reactive parasitics, carrier transit times, resistive losses and self-heating which in turn cause high-frequency roll-off and dominate the device functionality in the THz region [11, 12]. At the other end of the spectrum, infrared photonics cannot be extended down to frequencies less than several THz as phonon energy becomes comparable with photon energy. THz QCLs have been shown to operate down to 1.2 THz but at 10 K [13]. Gyrotron, BWO, FIR laser, FEL etc have been used for THz generation [14]. These sources have inherent limitations such as lower or upper limits in achievable frequency, high power requirements, bulkiness and operating temperature. An alternative and common approach for THz generation at a specified frequency is up-conversion from MW frequencies using frequency multipliers and/or mixers [15]. However, intrinsic conversion losses and difficulties in handling large input powers cause a multiplier's output power to drop rapidly with increasing frequency [1, 5]. Consequently, bridging the THz-gap still remains a formidable challenge [16].

The quest for room temperature and compact THz systems has been further challenged by the overall system integration. For most applications, an essential part of THz systems are the quasioptical components, used for beam collimation and focusing in order to attain a high resolution and signal-to-noise ratio for the system. Those components include substrate lenses, objective lenses and mirrors etc. These accompanying quasioptical components coerce sacrificing the system integration and compactness.

This thesis deals with the analysis and optimisation of the uni-travelling-carrier photodiode (UTC-PD) for CW THz generation. Photonic THz generation using UTC-PDs is extremely promising as it offers wide tunability, adequate output power and room temperature operation. Furthermore, a novel and compact catadioptric lens is proposed and investigated for realising compact systems.

In recent years, photonic generation of THz-waves at room temperature by photomixing has been one of the most promising and fostering techniques. Preliminarily, photomixing was used on the principle of translating ultrashort optical pulses into electrical pulses for THz generation [17]. However, this technique involves bulky and expensive laser sources. CW photomixing relies on the mixing of two closely spaced laser wavelengths generating a beat oscillation at the difference frequency [18, 19]. This technique offers wide tunability and enables to obtain high spectral purity. Photodiodes (PD) are the key component for photomixing. Being first reported in 1997 by Ishibashi *et al.* [20], the Uni-Travelling-Carrier Photodiode (UTC-PD) has become very promising by demonstrating output powers of 20 mW at 100 GHz [21] and 25 μ W at 1 THz [22].

With the intent to realise a compact sensor, a novel and compact catadioptric lens has been proposed for quasioptical integration and imaging applications. The catadioptric lens, presented in this thesis, provides an alternative solution to be used as a focusing element utilising reflection and refraction caused by the difference in permittivity of the lens and the surrounding medium. The lens and its focal length are electrically small (in

the order of few wavelengths). Radiating elements and sensors can be physically coupled to the lens in order to achieve short-range focusing ability, therefore, enabling a compact sensing system. Thus, the lens provides greater ease of system integration compared to the conventional quasioptical components.

The thesis is basically divided into the following parts.

In Chapter 2, the limitations and optimisation scopes of the InGaAs/InP based UTC-PDs for attaining higher bandwidth as well as higher output power are discussed. A hydrodynamic (HD) carrier transport model is used to analyse the device. An example of UTC-PD epitaxial layer optimisation for continuous-wave THz generation at 340 GHz is shown using the HD model. The output power and the optimum embedding impedance for the UTC-PD, as a function of device parameters, are also studied at different optical injection levels. Several plausible integration schemes and antenna design examples at 340 GHz are explored.

Chapter 3 focuses on the catadioptric lens. The focusing property of the lens is investigated using 3D full-wave electromagnetic solvers. The proposed catadioptric lens is designed and fabricated from Delrin and Macor. Simulation and characterisation results are presented at microwave and terahertz frequencies (108 GHz).

Chapter 4 presents several short-range imaging examples employing catadioptric lenses.

Chapter 5 contains brief discussions on the previous chapters and presents a number of scopes for future work.

Chapter 2. Photonic THz Generation

With the ability to translate the input optical signal to an output electrical signal, photodetectors are one of the key optoelectronic devices that have led to the innovation of many emerging technologies, such as photo receivers, millimetre wave generators, fibre-optic communication systems, wireless communications, and high frequency measurement systems. Photonic CW THz generation relies on the photomixing of two closely spaced laser wavelengths producing a beat oscillation at the difference frequency, as exemplified in Figure 2.1. By changing the incident wavelength(s), the frequency of the generated electrical signal can be varied. Heterodyne photomixing was first demonstrated in 1947 by Forrester *et al.* [19] using a phototube combined with a RF cavity. Due to advances in high-speed III-V materials, the photomixing technique is being extensively utilised using photodiodes or photoconductors for RF signal generation even up to THz frequencies [23]. However, photonic THz generation technique was first developed using femtosecond optical laser pulses [17] which paved the way for terahertz time-domain spectroscopy [24].

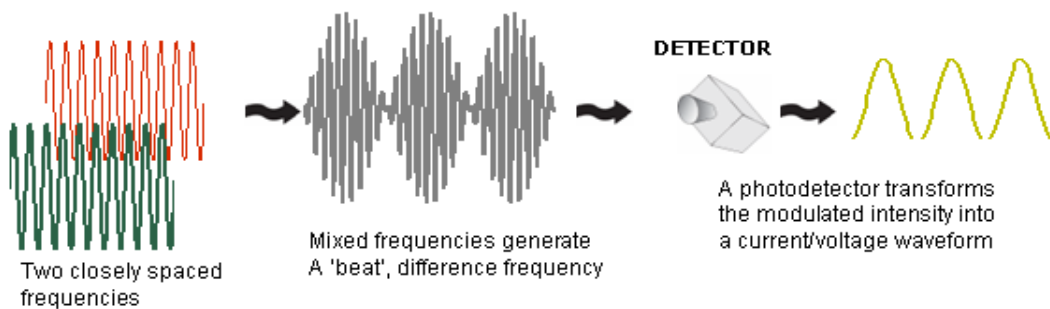


Figure 2.1: The mixing of two closely spaced laser wavelengths generates a beat oscillation at the difference frequency and the photodetector translates the optical signal to electrical signal.

A lightweight, compact, robust and room-temperature THz generation technique has become a must in many applications. THz generation using photomixing technique is very promising as it can fulfil the afore-mentioned criteria. A scheme for THz generation is shown in Figure 2.2 (a). Photomixer based THz sources can provide wide tunability and high spectral resolution. The photomixing technique is being seriously evaluated for future WLAN and other telecommunication applications. Researchers have already reported a gigabit Ethernet [25] utilising the photomixing technique. According to a recent study [26] initiated by the European Space Agency (ESA), photomixers are considered as one of the most promising candidates for the generation of THz signals.

Transmission losses through an optical fibre is very small (≤ 1 dB/km) [27]. By up-converting the THz signal to the optical domain, the signal can be easily distributed through an optical fibre, as shown in Figure 2.2 (b). At the receiving end, a photomixer can be used to translate the signal from the optical to the electrical domain. The

photomixing technique is particularly interesting for LO distribution over a large distance. The technique has also been considered for use in the Atacama Large Millimetre/submillimetre Array (ALMA) [28].

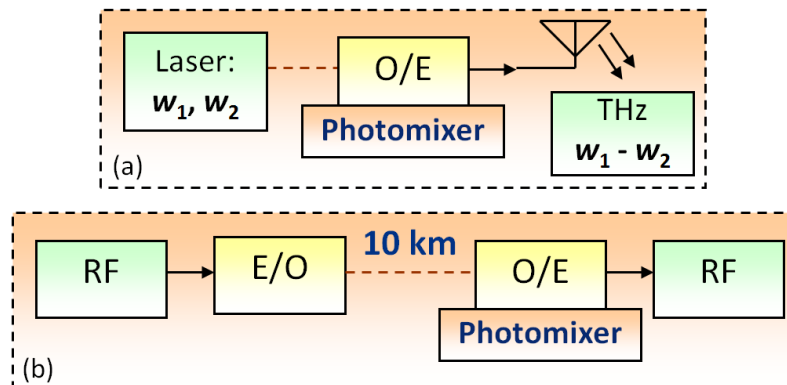


Figure 2.2: (a) THz-wave generation scheme using a photomixer. (b) A scheme for LO distribution where the signal is converted from electrical domain to optical domain and guided through an optical fibre. At the other end, the optical signal can be converted to electrical domain using a photomixer.

The two most common approaches to realising photonic THz generation are to use low-temperature grown GaAs (LT-GaAs) and PIN-PD [29]. LT-GaAs photomixers can provide $\sim 2 \mu\text{W}$ at 1 THz [30] and their operation frequency can be as high as 5 THz [31]. LT-GaAs based photomixers can also be incorporated with metal-semiconductor-metal (MSM) structures [32]. However, the main drawbacks are the low responsivity, reliability issues [33]. Furthermore, as LT-GaAs photomixers utilise of $0.8 \mu\text{m}$ wavelength, those do not benefit from the abundant and less-expensive equipments working at $1.5 \mu\text{m}$ wavelength.

The conventional PIN-PD consists of a p - and n -doped layer with an intrinsic layer sandwiched in between. In addition to the built-in electric field across the intrinsic layer, a reverse bias is often applied to enhance the field gradient. Electron-hole pairs are generated at the PIN-PD when photons with energy equal to or higher than the bandgap energy are absorbed. In the 1960s, a number of researchers reported photomixing using PIN-PDs [29, 34-36]. However, due to its limitations concerning low saturation current and low bandwidth, the output power of a PIN-PD is limited to a few nW at 1 THz [37].

However, the general limitations of the photomixing technique include the required laser sources and their stability, optical coupling, device fabrication issues and low output power.

2.1 Uni-Travelling-Carrier Photodiode

In 1997, a new ultrafast photodiode, the uni-travelling-carrier photodiode (UTC-PD), was proposed by Ishibashi *et al.* [20]. The prime feature of this PD was a much higher output saturation current compared to conventional PIN-PDs. UTC-PDs have separate absorption and collection layers. The space charge effect is reduced by utilising only electrons as the charge carriers. In recent years, UTC-PDs have become very promising by demonstrating output powers of 20 mW at 100 GHz [21] and $25 \mu\text{W}$ at 1 THz [22].

Due to the high-speed and high power output characteristics, UTC-PDs are very attractive for millimetre and submillimetre wave generation, fibre-radio, wireless communication systems and wireless links, future WLAN, wireless HDTV transmission and so forth [38, 39].

2.1.1 Basic principles

For a conventional PIN-PD, the incident light is absorbed in the intrinsic region and electron-hole pairs are created. The velocity of electrons is 6 – 10 times faster than that of holes. The presence of holes in the intrinsic region leads to the build-up of the space-charge, band bending, and current saturation effects. A reduction in the absorption layer thickness decreases transit times while increasing device capacitance. On the other hand, UTC-PDs have separate absorption and collection layers. Therefore those layers can be optimised independently.

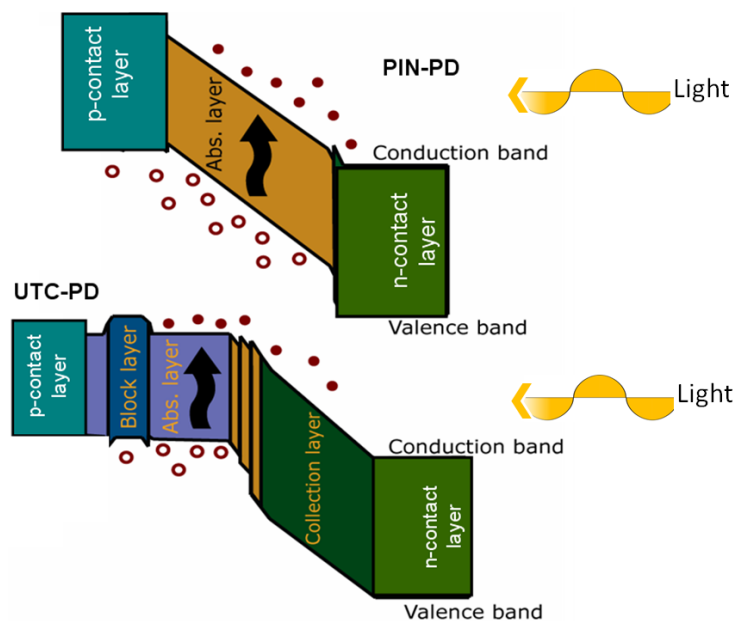


Figure 2.3: (a) Schematic band diagrams of the PIN-PD and UTC-PD.

Figure 2.3 shows a comparison between the operational principles of the PIN-PD and the UTC-PD. Except the absorption layer, the band gap of all the layers should be sufficiently large as compared to the photon energy of the optical illumination so that the optical absorption takes place in the absorption layer only. As light is absorbed in the p -doped region, the distance to the p -contact for the holes and the transit time can be significantly short. In this way the build-up of holes can be avoided, which would otherwise at some point screen the acceleration field normally present in the device. In the absorption layer, the minority electrons are moved to the edge of transport region by diffusion, photo-induced electric field and/or the built-in potential gradient in the absorption region.

The unidirectional motion of the electrons is achieved by a diffusion blocking layer at the p -contact side. The holes are confined to the absorption region by the appropriate choice of the band profile at the interface between the absorption and transport regions. On the other hand, the band profile for the electrons should be smooth enough so that it

does not hinder the electron transport between the absorption and transport regions. The electron travelling time can be effectively reduced by the quasi-field formed by the band gap grading and also by graded doping. In UTC-PDs, the space charge consists of only electrons whose velocity is much higher than that of holes and thus postpones current saturation offering higher operation current [40].

UTC-PDs can be realised with GaAs/AlGaAs for the optical wavelength of 0.8 μm . For the 1.5 μm wavelength, InGaAs/InP material system can be used. The latter one features high mobility, high overshoot, and high saturation velocities of electrons. Moreover, the 1.5 μm lasers and accompanying equipments are well developed and inexpensive due their extensive use in the optical telecommunication systems. Figure 2.4 depicts a typical layer structure and an example of the UTC-PD layer structure parameters.

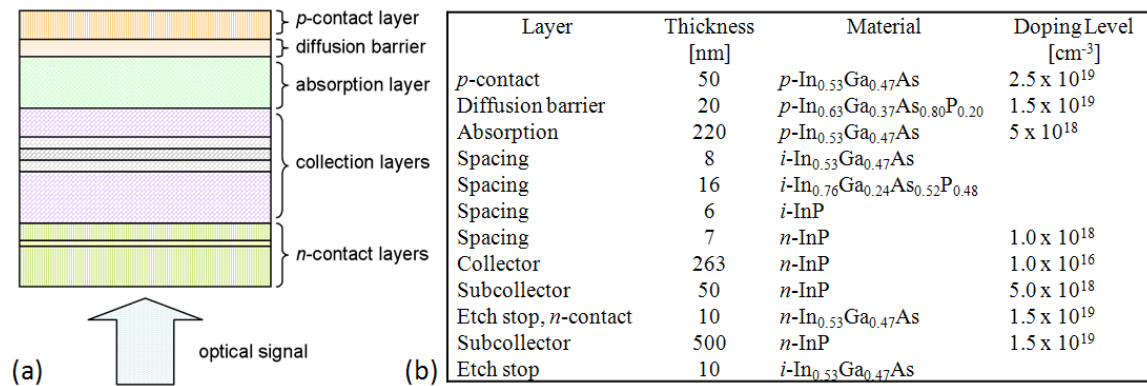


Figure 2.4: (a) Layer structure of a typical UTC-PD, and (b) an example of the layer structure parameters [41].

The electron transfer between different valleys in the conduction band is a multi-particle scattering process, involving phonons for momentum conservation. When an electric field is applied, some delay may occur before the average velocity of the carriers reaches a new equilibrium value. At a high enough field, the carriers are accelerated to a velocity higher than its long-term equilibrium value before the momentum and energy relaxation processes bring the velocity down to the equilibrium value. Thus, an average electron in a semiconductor device may travel a substantial distance reaching a velocity beyond its maximum value in a homogenous bulk material. This phenomenon is commonly referred to as velocity overshoot. When the photogenerated electrons of the UTC-PD enter the depletion region from the absorption region, they experience an almost instant change in the electric field and velocity overshoot occurs.

However, this velocity overshoot process is rather intricate in GaAs, InP and in similar materials [42, 43]. At relatively higher electric field, electrons in the lower valley (high mobility and low effective mass) can be excited to the normally unoccupied upper valley (low mobility and high effective mass). This is called transferred-electron effect. This effect, concerning intervalley electron transfer, causes a negative differential mobility and the drift velocity starts to decrease. Therefore, the velocity overshoot gets suppressed as soon as the electrons gain enough energy for the inter-valley scattering.

Monte Carlo simulations by Maloney and Frey [42] showed that the velocity overshoot due to an abrupt electric field change in InP may exceed 1 μm . In effect for submicron

distances, the overshoot phenomenon allows electrons to travel faster than its maximum saturation velocity. In other words, submicron devices can utilise the overshoot phenomenon in order to achieve higher device performance.

2.1.2 Material and epitaxial structure

The functionality of the UTC-PD largely relies on the high electron mobility. Semiconductor materials with high electron mobility are needed to realise the UTC-PD structure. A range of compound semiconductor materials offer many of these desired features and can be synthesised without too much difficulty. Heterojunctions have become essential for the design of high performance optoelectronic device. But in this case the materials must have similar lattice parameters to enable the epitaxial growth of a semiconductor on top of another and to minimise the number of defects.

InGaAs and InGaAsP have identical lattice constants as InP at certain mole fractions. Figure 2.5 (a) illustrates the bandgap energy and lattice constants of various semiconductor materials. The figure can be used to determine the available possibilities for the UTC-PD layer composition. For instance, the layer composition can be chosen as $\text{In}_{0.53}\text{Ga}_{0.47}\text{As}$ for the absorption layer, $\text{In}_{0.63}\text{Ga}_{0.37}\text{As}_{0.80}\text{P}_{0.20}$ for the diffusion blocking layer, and $\text{In}_{0.76}\text{Ga}_{0.24}\text{As}_{0.52}\text{P}_{0.48}$ for the graded layer. All these compositions have the same lattice constant as InP and can therefore be grown on the same substrate with InP as the collection layer.

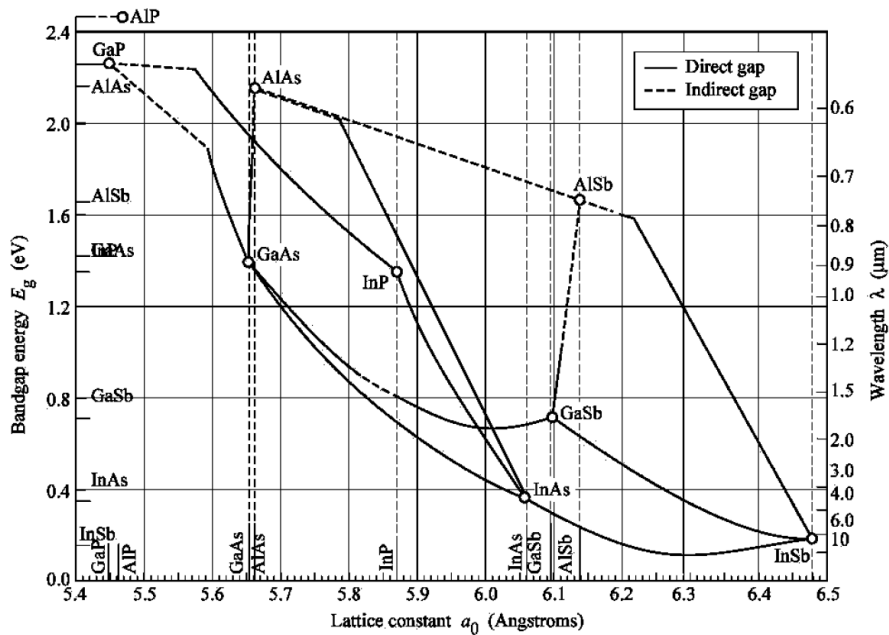


Figure 2.5: Bandgap energy and lattice constant of various semiconductor materials [44].

Materials	Bandgap (eV)
$\text{In}_{0.53}\text{Ga}_{0.47}\text{As}$	0.77
InP	1.35
$\text{In}_{0.63}\text{Ga}_{0.37}\text{As}_{0.80}\text{P}_{0.20}$	0.90
$\text{In}_{0.76}\text{Ga}_{0.24}\text{As}_{0.52}\text{P}_{0.48}$	1.05

Table 2.1: The energy bandgaps of the materials used in the UTC-PD [45].

The above mentioned layer composition enables the UTC-PD to work at 1.55 μm , which is a telecom standard. This specific wavelength suffers particularly small losses when propagating through an optical fibre. The wider bandgap of InP allows the incident light of 1.55 μm to reach the intended InGaAs absorption layer without being absorbed elsewhere. A higher bandgap (compared to InGaAs) material, InGaAsP, is used as a blocking layer to reduce diffusion of electrons towards the p -contact region. Table 2.1 lists the energy bandgaps of the materials used in the UTC-PD.

2.1.3 Equivalent circuit

The equivalent circuit of a UTC-PD, as shown in Figure 2.6, can be realised as a current source $I_{\text{UTC-PD}}$ in parallel with a resistance $R_{\text{UTC-PD}}$ and a capacitance $C_{\text{UTC-PD}}$. The R_s represents the series resistance. $R_{\text{UTC-PD}}$ is in the order of 10 $\text{k}\Omega$ [46] without illumination while R_s is in the order of few ohms. The value of $C_{\text{UTC-PD}}$ can be determined as if the layers of the UTC-PD were a parallel plate capacitor. The depleted layers of the UTC-PD acts as a parallel plate capacitor and the differential capacitance can be determined by (2.1) where ϵ denotes the permittivity of the depleted layers, A is the junction area. Here, w denotes the width of the depleted layers which are dependent [41] on reverse bias V_r and built-in voltage V_{ri} , as shown by (2.2).

$$C_{\text{UTC-PD}} = \frac{\epsilon A}{w(V_r, V_{ri})} \quad (2.1)$$

$$w \propto \sqrt[m]{V_{ri} + V_r} \quad (2.2)$$

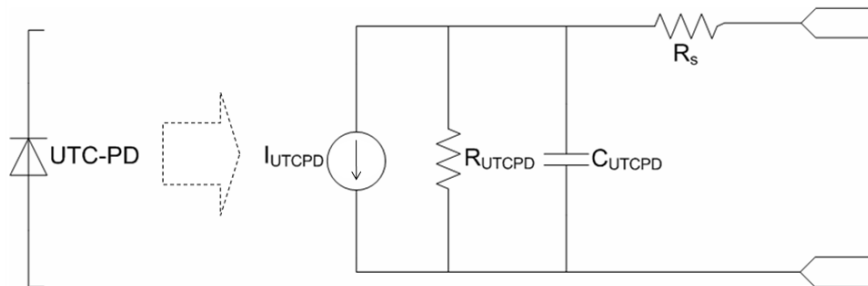


Figure 2.6: An equivalent circuit of the UTC-PD.

2.1.4 Performance factors

A number of factors exist that determine the performance of the UTC-PD [41]. In this section those performance factors are discussed together with possible strategies to improve and overcome the device limitations.

Quantum efficiency: Being a photodetector, the UTC-PD converts an injected optical signal to an electrical signal. This conversion of optical power into electrical power is dependent on the absorption coefficient of the semiconductor material and the thickness of the absorbing region. The effectiveness of this process can be expressed as the quantum efficiency, η , of a photodetector, and is given by (2.3), where, $h\nu$ is the photon energy, q is the elementary charge, P_{inj} is the injected optical power, and I_{ph} is the photocurrent.

$$\eta = \frac{I_{ph} / q}{P_{inj} / h\nu} \quad (2.3)$$

Responsivity: Responsivity, as denoted by R in (2.4), is a measure of the photodetector's ability to convert incident optical power into an output current. Here λ is wavelength of the incident photons. Since the diffusion length in the InGaAs absorption layer is much longer ($\sim 1 \mu\text{m}$) than the absorption layer thicknesses in general, the responsivity increases linearly with absorption layer thickness [47]. Therefore responsivity can be improved by increasing the thickness of the absorption layer.

$$R = \frac{I_{ph}}{P_{inj}} = \eta\lambda / 1.24 \quad (2.4)$$

Time constants: The response time of the UTC-PD is determined by the transit time across the device and the RC -time constant. The electron diffusion time in the absorption layer determines the total carrier transit time except for a thin absorption layer (less than 100 nm). The transit time, τ_{tr} , can be approximated [48] as (2.5) where W_A , D_e and v_{th} are the absorption layer thickness, diffusivity of electrons in the absorption layer and the electron thermionic emission velocity ($2.5 \times 10^7 \text{ cm/s}$), respectively. The carrier travelling time in the collection layer can be defined as $\tau_C = W_C / v_d$. Here W_C is the collection layer width and v_d is the drift velocity of the electrons.

$$\tau_{tr} = \tau_A + \tau_C = \frac{W_A^2}{3D_e} + \frac{W_A}{v_{th}} + \frac{W_C}{v_d} \quad (2.5)$$

The first term of equation (2.5) is responsible for the purely diffusive transport. This term dominates when the absorption layer thickness is comparatively large i.e., more than 100 nm. In this situation, $\tau_A \propto W_A^2$. On the other hand, the second term of the equation (2.5) dominates when the absorption layer is thinner. For absorption layer thicknesses less than 100 nm, $\tau_A \propto W_A$.

The RC -time constant, τ_{RC} can be expressed as (2.6) where R_{int} represents the internal resistance and R_{load} represents the load resistance. Since the absorption and collection layers in the UTC-PD are separate, τ_{tr} and τ_{RC} are decoupled. This effectively means that the device speed can be enhanced by reducing W_A without affecting the RC -time constant. But this will decrease responsivity and therefore a trade-off exists in this regard.

$$\tau_{RC} = RC = (R_{load} + R_{int}) \varepsilon A / w \quad (2.6)$$

Bandwidth: If the input optical power and the reverse bias are kept constant, the 3-dB bandwidth is defined as the frequency point when the output signal has decreased by 3 dB from its highest value. The 3-dB bandwidth can be determined by optical heterodyning or the impulse response method. The 3-dB bandwidth, f_{3dB} , can be expressed as (2.7). To achieve high bandwidth, both τ_{tr} and τ_{RC} should be kept low.

$$f_{3dB} = \frac{1}{2\pi\sqrt{\tau_{tr}^2 + \tau_{RC}^2}} \quad (2.7)$$

2.1.5 Device fabrication

The fabrication and characterisation of UTC-PDs at Chalmers have been published in [41, 49]. The devices had a $50\ \Omega$ coplanar waveguide leading up to the device itself to accommodate coplanar measurement probes, as shown in Figure 2.7.

A typical fabrication procedure includes the following sequential steps:

- I. p -contact formation.
- II. p -mesa and n -mesa formation.
- III. n -contact formation.
- IV. Thick metal deposition (e.g. transmission lines)
- V. Air-bridge formation.
- VI. Anti-reflective coating (SiN) at the bottom of the substrate (required for vertically illuminated UTC-PDs).

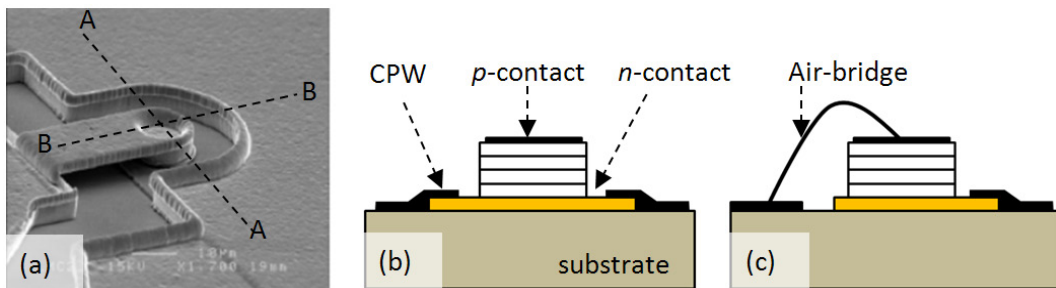


Figure 2.7: (a) SEM photograph of an UTC-PD, fabricated at Chalmers. Cross-sectional views along (b) AA and (c) BB.

Figure 2.8 shows the DC measurement plots for $13\ \mu\text{m}$ and $17.5\ \mu\text{m}$ diameter UTC-PDs without illumination. For both the devices, $W_A = 220\ \text{nm}$ and $W_C = 263\ \text{nm}$. Figure 2.8 (a) shows the DC current density versus applied voltage. The pinch-off voltage, as the figure shows, is around $0.5\ \text{V}$. While Figure 2.8 (b) shows the differential DC conductance. The reverse bias breakdown starts at around $8\ \text{V}$ and is not abrupt. The full breakdown voltage is beyond $15\ \text{V}$. According to a previous measurement, the breakdown voltage was $16.5\ \text{V}$ [41]. Further characterisations have been published in [41].

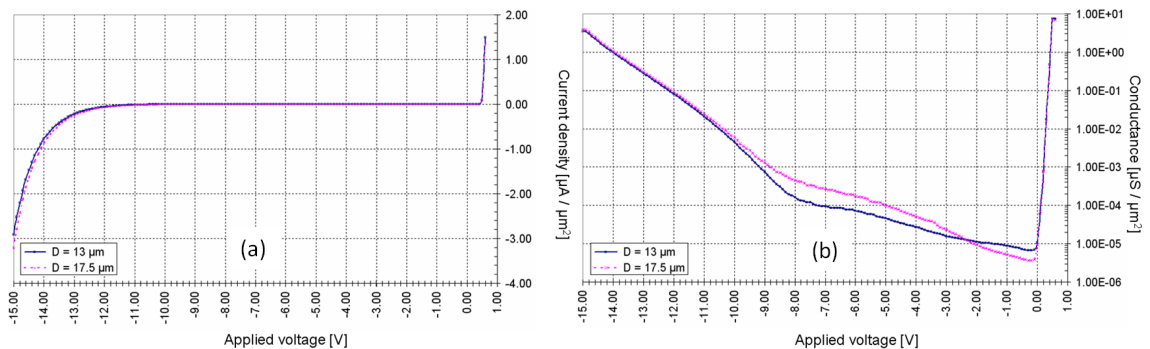


Figure 2.8: DC measurement plots (without illumination) for $13\ \mu\text{m}$ and $17.5\ \mu\text{m}$ UTC-PD devices. (a) DC current density versus applied voltage (IV plot), and (b) differential DC conductance versus applied voltage.

2.1.6 Parameter extraction

In order to understand the impedance behaviour of the photodetector, the measured S -parameters of the fabricated UTC-PDs were compared with an equivalent circuit model. The fabricated UTC-PDs have a short strip of coplanar waveguide (CPW) leading up to them to accommodate the measurement probes, as shown in Figure 2.9 (a). The CPW is modelled as a π – network with L_{CPW} and C_{CPW} . Figure 2.9 (b) shows the equivalent circuit of the fabricated UTC-PD.

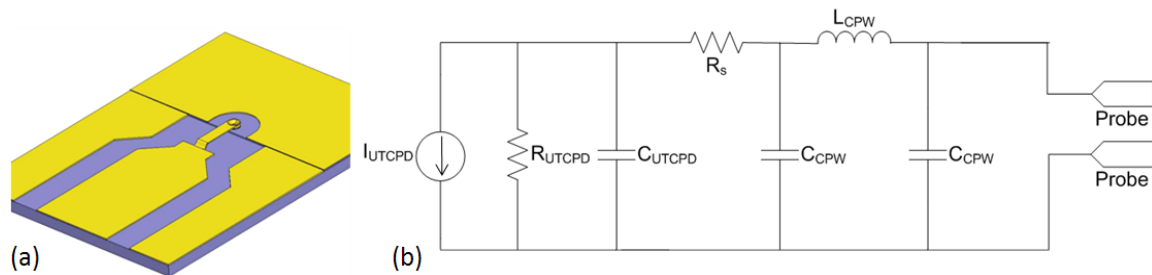


Figure 2.9: (a) Schematic of the air-bridged UTC-PD device with CPW striplines leading up to the detecting area (b) Equivalent circuit of the UTC-PD.

A set of measurements were performed to obtain the S_{11} data of a $10\ \mu\text{m}$ diameter UTC-PD at 1 V, 2 V, and 4 V reverse biased conditions without any optical injection. The equivalent circuit for UTC-PD and CPW, shown in Figure 2.9 (b), is modelled in Advanced Design System (ADS) [50] from Agilent. An optimiser based tool was used in ADS to fit the model with measurement results at a given reverse biased condition (1 V) and thus all the parameter values were extracted. Afterwards, the same model with the extracted parameters was used to evaluate the equivalent circuit model at other reverse bias conditions. The extracted values for the $10\ \mu\text{m}$ diameter UTC-PD at 1 V reverse bias are $R_{UTCPCD} = 20\ \text{k}\Omega$, $C_{UTCPCD} = 27\ \text{fF}$, $R_s = 5\ \Omega$. Figure 2.10 shows the S_{11} plot obtained by simulations and measurements from 10 GHz to 67 GHz for the $10\ \mu\text{m}$ diameter UTC-PD at 1 V bias conditions without any optical injection. The agreement between the measured and modelled results is quite good. However, the S_{11} plots for 2 V, and 4 V reverse bias conditions are almost the same as that of 1V bias. This can be attributed to the saturation of the photomixer capacitance when the reverse bias voltage is more than a specific value ($\sim 1\ \text{V}$).

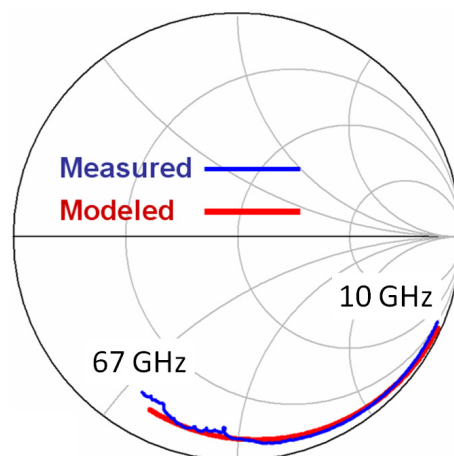


Figure 2.10: S_{11} plot obtained by modelled and measurement results from 10 GHz to 67 GHz for a $10\ \mu\text{m}$ diameter UTC-PD at 1 V reverse biased conditions.

2.2 Device modelling

In this section, UTC-PD modelling is discussed. Later, physical device models are discussed which were developed from the carrier transport physics and device geometry considerations. Finally, thermodynamic modelling is briefly discussed.

2.2.1 Carrier transport modelling

As for most semiconductor components, numerical simulations are important for the understanding and design of the UTC-PD for a specific application. By mapping the physical parameters like dimensions, doping, material, and incident optical power, the fundamental characteristics and trends in performance can be studied without costly split-lot experiments. This can also lead to more comprehensive insight and understanding of the device behaviour and optimisation.

In order to describe the carrier transport of semiconductor devices, the drift–diffusion (DD) approach [51] is widely used. However, it does not account for carrier temperatures and nonlocal effects like velocity overshoot which has been observed experimentally in UTC-PDs [52]. Different Monte Carlo methods [53] for solving the Boltzmann transport equation are available but require large computation time. The hydrodynamic (HD) carrier transport model [53, 54] is reasonably time efficient and well-suited for simulating heterostructure dimensions and doping profiles. In contrast to the conventional DD model, the HD model includes carrier temperatures and gives a more complete description of the carrier transport. Mobilities, diffusion coefficients etc. are functions of the carrier temperatures.

However, in order to model the UTC-PD epitaxy, both DD and HD models were developed and implemented using the commercial software package TCAD from Synopsis [55]. Figure 2.11 shows the graphical user interface describing the epitaxial layers of the device and the layer parameters. The developed models were mainly used for vertically illuminated UTC-PDs. However, with some modifications, the models can also be used for simulating other types of UTC-PDs as well.

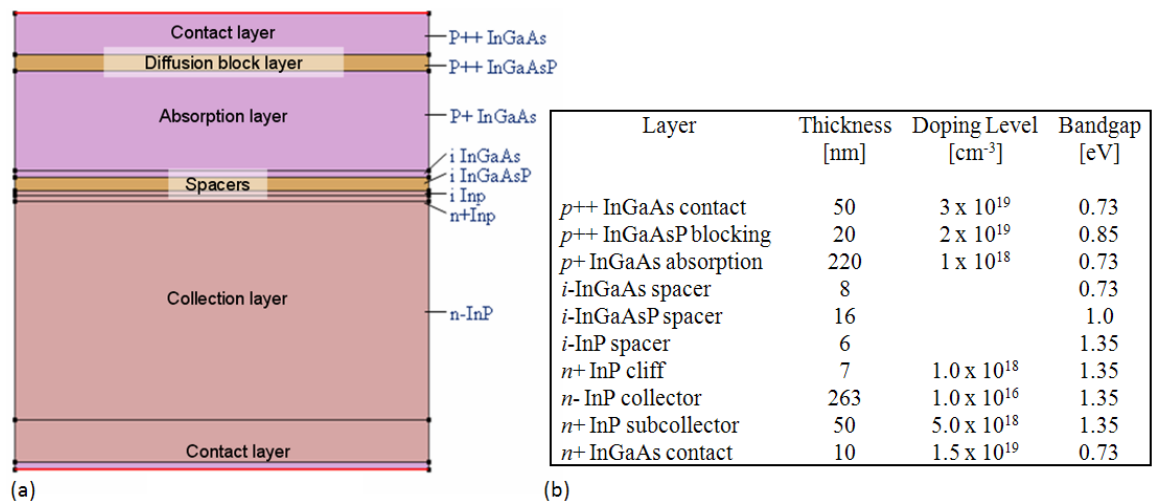


Figure 2.11: (a) The epitaxial layer structure of the simulated InGaAs/InP UTC-PD in TCAD, and (b) layer parameters.

2.2.2 Drift-Diffusion model

The Drift-Diffusion (DD) transport model [51] uses Poisson, electron and hole continuity equations to determine the carrier transport across the semiconductor device. The PDEs (Partial Differential Equations) are discretised and solved iteratively by Newton iterations. In case of the DD model, the electron and hole current densities are given by:

$$\vec{J}_n = -nq\mu_n\nabla\phi_n \quad (2.8)$$

$$\vec{J}_p = -pq\mu_p\nabla\phi_p \quad (2.9)$$

Here, q is the elementary charge, n and p are the electron and hole densities, μ_n and μ_p are the field dependent electron and hole mobilities, and ϕ_p and ϕ_n are the electron and hole quasi-Fermi potential, respectively.

2.2.3 Hydrodynamic model

The hydrodynamic (HD) carrier transportation model [53, 54] treats the propagation of electrons and/or holes in a semiconductor device as the flow of a charged compressible fluid producing hot electron effects and velocity overshoot in high-electric-field regions. The model also includes carrier temperature dependent parameters such as mobilities and diffusion coefficients and thereby accurately models the carrier transport. The simulated results of a UTC-PD using the HD model have been reported [56] in a detailed manner. The results suggest that the HD model is more accurate than the conventional DD model. The DD model underestimates device performance producing premature device saturation [56].

The HD model consists of the Poisson equation, continuity equations, and the energy conservation equations for electrons and holes. In the hydrodynamic model, the current densities can be represented as shown in (2.10 – 2.11), where T_n and T_p denote carrier temperatures while E_c and E_v are the conduction and valence band energies, respectively. The first term takes into account the contribution due to the spatial variations of electrostatic potential, electron affinity, and the band gap. The three remaining terms take into account the contribution due to the gradient of concentration, the carrier temperature gradients, and the spatial variation of the effective masses m_e and m_h . The energy balance equations are shown in (2.12 – 2.13) while (2.14 – 2.15) represent the energy flux equations. The collision terms in (2.12 – 2.13) are determined by energy dependent energy-relaxation times. The required values of transport coefficients for heat flux (f_n^{hf} and f_p^{hf}), thermal diffusion (f_n^{td} and f_p^{td}) and energy flux (r_n and r_p) were extracted from [57]. The hydrodynamic model used in this study doesn't include the gradient of the lattice temperature which depends on a number of factors including the overall dimension of the device, its integration with other structures and their thermal properties. In the model, a constant lattice temperature is assumed and this assumption is reasonable for relatively low P_{inj} . The HD model is discussed in more detail in [56, 58, 59]. The model was compared with the work reported by Ito *et al.* [60] and showed good agreement with the measured result (20.8 mW) by producing the saturated output power of ~ 20 mW at 100 GHz with photocurrent of 25 mA.

$$\vec{J}_n = q\mu_n \left(n\nabla E_C + k_B T_n \nabla n + f_n^{td} k_B n \nabla T_n - 1.5 n k_B T_n \nabla \ln m_e \right) \quad (2.10)$$

$$\vec{J}_p = q\mu_p \left(p\nabla E_V - k_B T_p \nabla p - f_p^{td} k_B p \nabla T_p - 1.5 n k_B T_p \nabla \ln m_h \right) \quad (2.11)$$

$$\frac{\partial W_n}{\partial t} + \nabla \cdot \vec{S}_n = \vec{J}_n \cdot \nabla E_C + \left. \frac{dW_n}{dt} \right|_{coll} \quad (2.12)$$

$$\frac{\partial W_p}{\partial t} + \nabla \cdot \vec{S}_p = \vec{J}_p \cdot \nabla E_V + \left. \frac{dW_p}{dt} \right|_{coll} \quad (2.13)$$

$$\vec{S}_n = -\frac{5r_n}{2} \left(\frac{k_B T_n}{q} \vec{J}_n + f_n^{hf} \hat{\kappa}_n \nabla T_n \right) \quad (2.14)$$

$$\vec{S}_p = -\frac{5r_p}{2} \left(\frac{-k_B T_p}{q} \vec{J}_p + f_p^{hf} \hat{\kappa}_p \nabla T_p \right) \quad (2.15)$$

$$\hat{\kappa}_n = k_B^2 n \mu_n T_n / q \quad (2.16)$$

$$\hat{\kappa}_p = k_B^2 p \mu_p T_p / q \quad (2.17)$$

2.2.4 Thermodynamic model

The UTC-PD is particularly interesting for high-power operation, which requires high input optical power. On the other hand, catastrophic failures of UTC-PDs occur under a high optical input condition and constant power dissipation [61]. Therefore its power dissipation tolerance is of great interest. The power dissipation and self-heating effect of a UTC-PD can be calculated self-consistently by incorporating the thermodynamic method with the DD and HD models by solving the lattice heat flow equation. However, the thermal properties of the UTC-PD are highly influenced by the surrounding geometry. Therefore, a simplified self-heating model can be used to include the surrounding geometry.

The heat dissipation of the UTC-PD is determined by the thermal resistance and the power dissipated across the device. The dissipated power can be computed by the current through and the voltage across the device. The self-heating effect in the UTC-PD was modelled in Comsol Multiphysics [62]. A full 3D FEM thermal analysis was carried out to estimate the amount of manageable input power. According to the analysis, the thermal resistance of a typical device was found to be approximately 2.5 K/mW. However, the thermal resistivity of InGaAs (16 cmK/W at 300K) is about a magnitude higher than that of InP (1.5 cmK/W at 300K) [63]. Therefore, the temperature increase in the InGaAs absorption layer is higher than the InP collection layer.

2.2.5 Simulation results

In this section, several simulation results are presented using the DD and HD model. Simulations were done using bottom illumination at 1.55 μm wavelength and using the layer structure shown in Figure 2.11 (b). Continuous wave DC simulations were performed varying bias voltage and input optical power. Large signal (nonlinear) stationary simulations were performed by looking at the transient response in the time-domain. The injected optical signal (1.55 μm) was modulated with a Gaussian pulse train.

The standard deviation of the temporal of the Gaussian distribution was set to such values that the pulse train mimics a sinusoidal pulse train at a specified frequency with a modulation index of 1. Steady-state results were obtained within a few cycles.

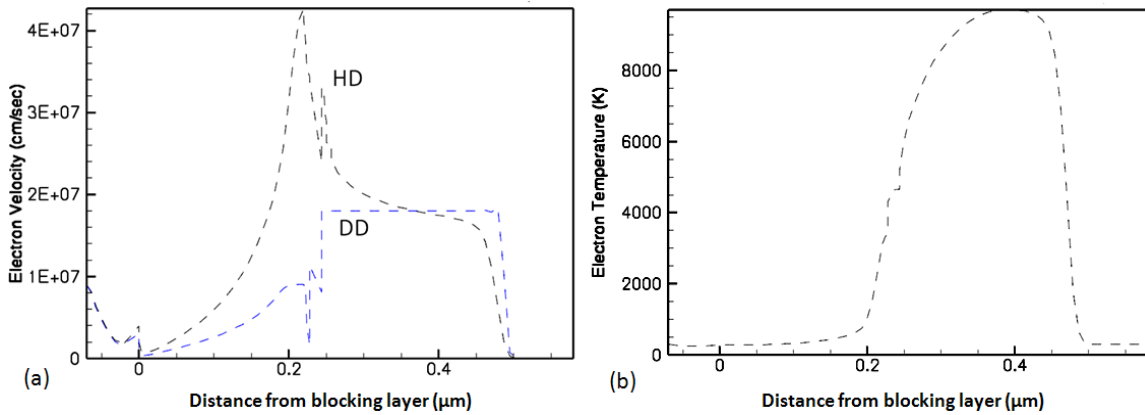


Figure 2.12: (a) Electron velocity distribution, and (b) electron temperature across the UTC-PD ($W_A = 220$ nm, $W_C = 263$ nm) at 4 V reverse bias.

Figure 2.12 (a) shows the electron velocity using the DD and the HD model. The device had $W_A = 220$ nm and $W_C = 263$ nm while the reverse bias was set to 4V. It can be noticed from the figure that HD has been able to model the velocity overshoot of the electrons, unlike DD. Figure 2.12 (b) shows the simulated electron temperature profile across the device. The electron temperature increases from ambient temperature (300K) to high temperature when the electrons enter the depletion layer as they experience a high electric field. A comparative study of the HD and DD model, reported in [56], shows that the DD model underestimates device performance.

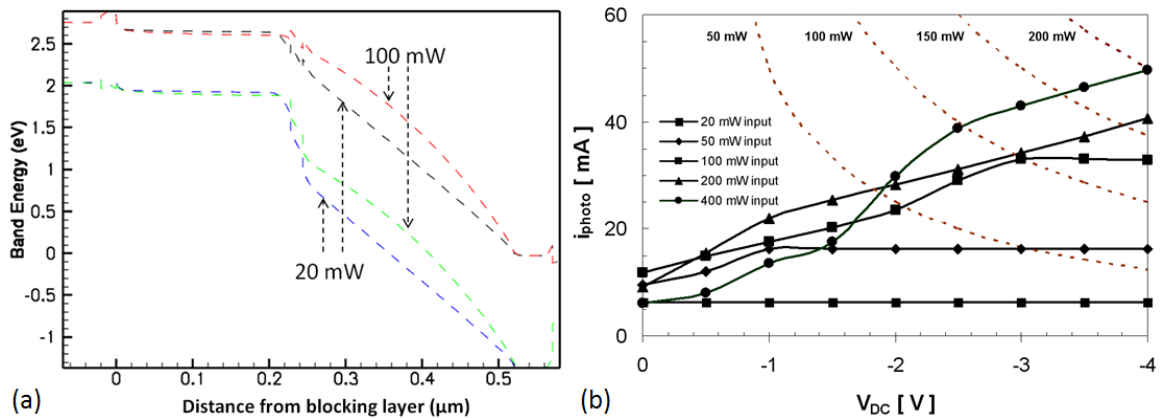


Figure 2.13: (a) Energy band-diagram for different optical injection levels at 2V reverse bias, and (b) simulated photocurrents of a 5 μ m diameter UTC-PD ($W_A = 220$ nm, $W_C = 263$ nm) at different optical injection levels and bias voltages. The dashed curves represent iso-power-dissipation curves.

Figure 2.13 (a) shows the energy band diagram of a 5 μ m diameter UTC-PD ($W_A = 220$ nm, $W_C = 263$ nm) under different optical injection levels at 2 V reverse bias. As can be seen in the figure, at relatively high injection level the carrier accumulation impairs the acceleration field in the collector region and thereby saturates the detector response.

Figure 2.13 (b) shows simulated photocurrents at different optical illumination levels and bias voltages. The dashed curves represent iso-power-dissipation curves. As can be seen from the figure, at high optical illumination levels, high bias voltage is necessary to avoid space charge effect and thereby to attain high current. However, a high bias voltage gives rise to a high dissipated power as shown by the iso-power-dissipation curves. Therefore the bias the voltage has to be carefully chosen in order to avoid burn out with a safe margin. Alternatively, thermal engineering is necessary to improve the thermal performance of the UTC-PD.

Figure 2.14 shows the differential capacitance of a 5 μm diameter UTC-PD ($W_A = 220$ nm, $W_C = 263$ nm). The voltage-dependent nonlinear capacitance of the UTC-PD affects the embedding impedance and will be discussed in the latter part of this chapter.

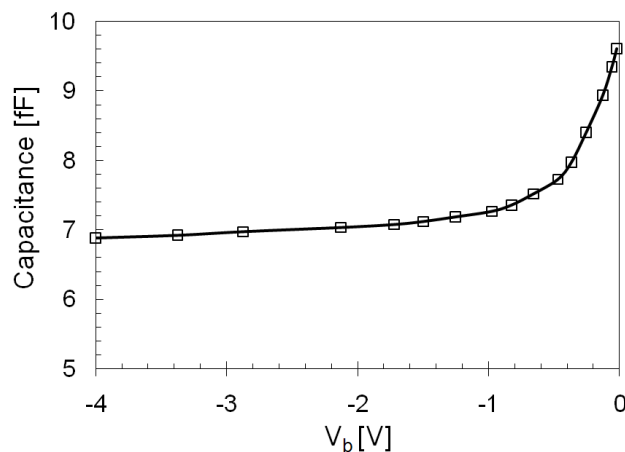


Figure 2.14: Differential capacitance of a 5 μm diameter UTC-PD ($W_A = 220$ nm, $W_C = 263$ nm).

2.3 Device optimisation

TCAD tools play a vital role in the development of new technology and to perform design of experiments (DOE). A realistic physical model of a certain semiconductor device enables to optimise it in TCAD. Due to the device physics of the UTC-PD, its efficient operation for a certain application requires optimisation. In this section, limiting factors and optimisation scopes are discussed. Later, the developed physical model is used to perform DOE and thereby to optimise a UTC-PD structure.

2.3.1 Limiting factors and optimisation scopes

The bandwidth and output power of the UTC-PD depends on layer alloy composition, dimensions and thicknesses, and other physical parameters such as doping concentration of absorption and collection layers, bias voltage, and level of optical injection.

In order to achieve higher output power and higher bandwidth from the UTC-PD, several trade-offs exist which require careful considerations regarding the UTC-PD design, its operating frequency and application. For higher output power (P_{out}), the responsivity can be improved by increasing the thickness of the absorption layer W_A . But this results in an increase in τ_A and thus a decrease in f_{3dB} . Higher output power is also achievable by increasing the device area.

However, for larger active areas, the devices become slower due to an increase in the capacitance and τ_{RC} . Therefore the f_{3dB} will be reduced in this case as well. On the other hand, the increase in the collection layer width W_C decreases the electric field E in the layer and increases τ_C . Evidently a trade-off exists regarding the choice of the optimum dimensions for W_A and W_C , as illustrated in Figure 2.15. Relevant discussion and implementation of this optimising technique are provided in the latter part of this chapter. However, UTC-PD area optimisation involves a number of factors including capacitance, series resistance, spreading resistance and thermal resistance that are dependent on the device area.

The output power is proportional to the square of the input optical power (when saturation does not occur). It has also been shown that the output power scales with the radiation resistance at the resonant frequency [40]. But the UTC-PD capacitance and the increase in the load resistance introduce higher τ_{RC} and in turn f_{3dB} is decreased. However, this can be resolved by using a load impedance that cancels out the device capacitance. Resonant type of antennas (e.g. dipole) offers this opportunity to cancel out the device capacitance and also provides higher resistance, and thus higher power. But the bandwidth is narrower compared to other antennas. In the latter part of this chapter, several antenna designs to maximise the output power will be discussed.

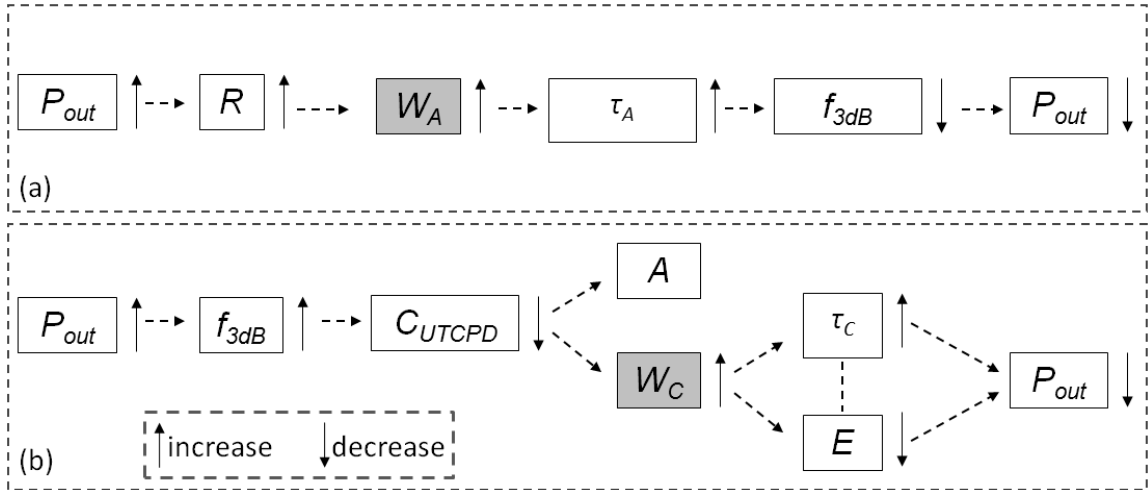


Figure 2.15: UTC-PD layer optimisation by (a) varying absorption layer thickness W_A and (b) collection layer thickness W_C .

2.3.2 Device structure optimisation

The bandwidth, output power and the overall performance of the UTC-PD are dependent on the responsivity and carrier transit times. In light of the previous discussion, W_A and W_C can be optimised to increase the output power. In the work, reported in Paper A, an InGaAs/InP UTC-PD with 5 μm diameter is optimised for continuous-wave (CW) THz generation at 340 GHz by varying W_A and W_C . The positions of these layers are shown in Figure 2.16 (a). The optimisation approach used is general in that it can be applied for any target frequency. The photodiode epitaxy is modelled and optimised using TCAD implementing the HD model. Large signal simulations were performed during the optimisation procedures.

The ~ 340 GHz band [1, 64] has interesting applications for the remote sensing of atmospheric gases, thus there is a need for the development of tunable local oscillator sources for sensitive detection.

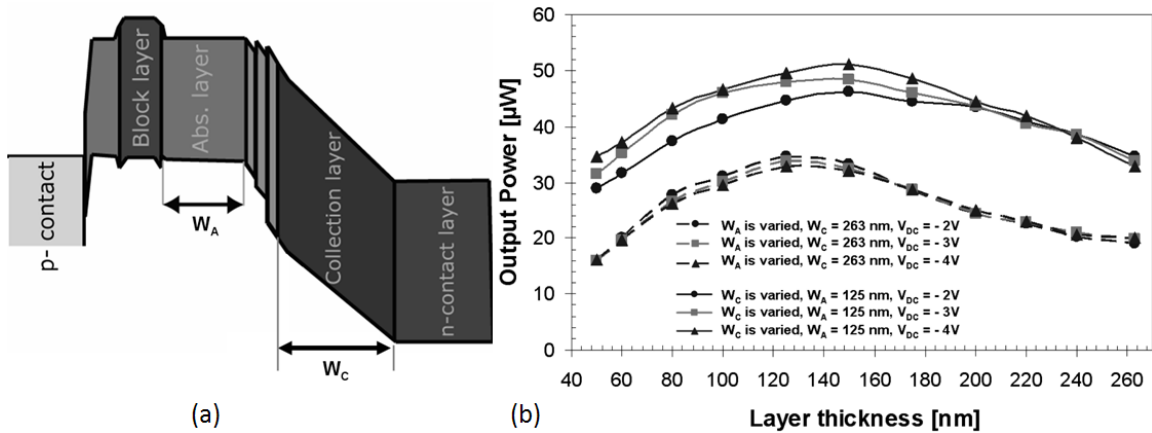


Figure 2.16: (a) Schematic of the UTC-PD band diagram and the two layers that were varied in the simulations (W_A and W_C) have been marked. (b) Calculated output power varying the absorption layer (W_A), collection layer thicknesses (W_C) and bias voltage (V_{DC}). Input optical power is 50 mW (17 dBm).

In this study, W_A and W_C were optimised consecutively. As can be seen from Figure 2.16 (b), the optimised W_A is 125 nm for $W_C = 263$ nm. Subsequently, with W_A determined, the device was optimised by varying the collection layer thickness W_C . As shown in Figure 2.16 (b), the optimised value for W_C was found to be 150 nm. However, the optimised values of W_A (and W_C) are the same for all the specified bias voltages. The optimised device, with $W_A = 125$ nm and $W_C = 150$ nm, was then simulated varying the input optical power at different DC bias conditions.

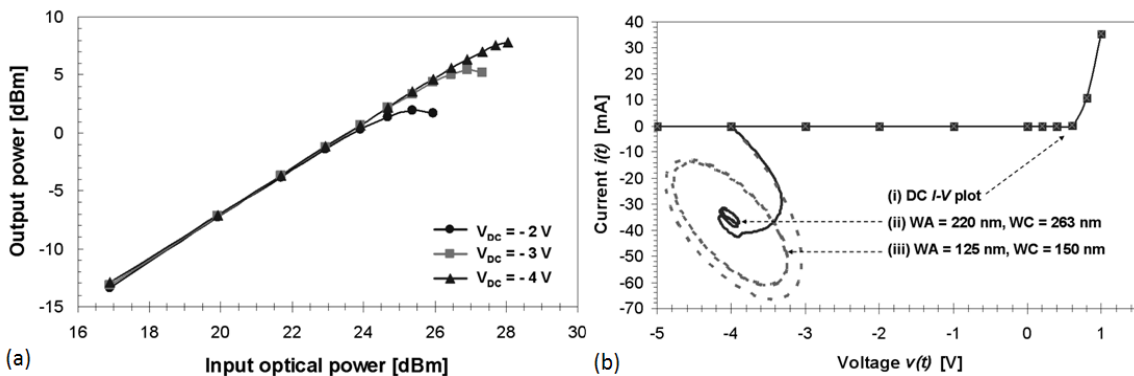


Figure 2.17: (a) Simulated output power of the optimised UTC-PD layer structure, obtained by varying the input optical power for different bias voltages (V_{DC}). (b) DC I - V plot of the optimised device and the phase portrait of the device at 27 dBm input optical power before and after optimisation. Here, $V_{DC} = -4$ V.

Figure 2.17 (a) illustrates the simulated output power versus input optical power. However, these simulations do not include any self-heating effects. As can be seen from Figure 2.17 (a), the output power of the optimised UTC-PD saturates at different optical injection levels depending on V_{DC} . The maximum saturated output power of ~ 6 mW is achieved at $V_{DC} = -4$ V and at 28 dBm input optical power. In order to validate the performance of the optimised UTC-PD, an example of the simulated phase portraits $v(t)$

Vs $i(t)$ for the 5 μm diameter device has been presented in Figure 2.17 (b) before and after the optimisation with 27 dBm (0.5 W) input optical power. Before optimisation, the device layer thicknesses were $W_A = 220$ nm and $W_C = 263$ nm [7]. Here $v(t)$ and $i(t)$ are the time varying voltage across and current through the UTC-PD at $V_{DC} = -4$ V. The phase portrait and the DC I - V plot, shown in Figure 2.17 (b), indicate the shift of the UTC-PD operating point. The figure also shows that the optimised device provides higher AC component in $i(t)$ and higher output power.

The thermal resistance of a typical device was found to be approximately 2.5 K/mW, which depends on the layer structure and surrounding geometry. The temperature rise depends on the photocurrent and the bias voltage. The analysis also shows that the maximum temperature inside the active region is expected to be significant ($\geq 150^\circ\text{C}$) for input optical powers above ~ 0.25 W and at $V_{DC} \geq -2$ V (average photocurrent ≈ 18 mA), thereby degrading the overall device performance. As can be seen in Figure 2.17 (a), at 0.25 W (24 dBm) input optical power, the output power is almost the same for all three bias conditions while $V_{DC} = -2$ V bias condition should be chosen as it offers the least heat dissipation. Hence, the maximum theoretical output power at 340 GHz for the optimised UTC-PD structure will be ~ 1 mW assuming a maximum allowable optical excitation of 0.25 W. However, with efficient thermal management, the optimised device is able to handle higher optical injection and thereby provide higher output power avoiding device failure.

The findings and results regarding UTC-PD epitaxy optimisation have been reported in Paper A.

2.4 Optimum embedding impedance

An UTC-PD, as discussed before, can be regarded as a current source in parallel with a capacitor and a resistor. The device capacitance can be estimated as a parallel plate capacitor and therefore the capacitance depends on the device area and the collection layer thickness W_C . Moreover, the capacitance also depends on the voltage across it, as shown in Figure 2.14. For maximum power transfer from the UTC-PD to the load impedance, matching is required. However, the photocurrent generated by the UTC-PD creates a time varying voltage drop across the load impedance and thus shifts the bias point. Therefore it is important to know the optimum embedding impedance at different optical illumination levels.

In order to investigate the dependence of device parameters of the UTC-PD on high optical injection, a study was carried out where contour plots were obtained for a $5\mu\text{m}$ diameter UTC-PD at different optical input levels from 0.5 mW to 500 mW. The device layer thicknesses were $W_A = 125\text{ nm}$ and $W_C = 150\text{ nm}$. Figure 2.18 (a) shows the equivalent circuit setup in TCAD. The extrinsic series resistance, $R_s = 15\ \Omega$, represents the spreading resistance and ohmic contact resistance, which are not included in the physical device model. V_b is the bias voltage and Z_L represents the load impedance. V_b was set to 4V and Z_L was varied in order to obtain contour plots. The load impedance points (Z_L) on Smith chart are shown in Figure 2.18 (b).

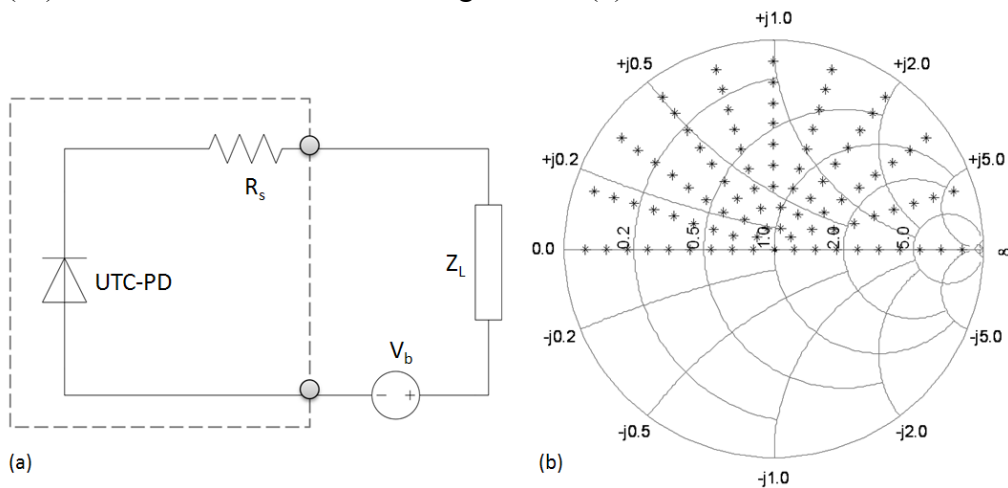


Figure 2.18: (a) Equivalent circuit setup for simulating CW THz generation by photomixing in TCAD, and (b) load impedance points (Z_L) on Smith chart.

Figure 2.19 shows the contour plots. The contours are spaced at 0.5 dB from each other. As can be seen from the figures, the optimum load impedance for maximum output power at different input optical power levels does not vary significantly. Figure 2.19 (j) shows the maximum available output power (for matched condition) at different optical injection levels. The figure also shows the 1-dB compression point. However, the device parameters of the UTC-PD change with optical injection. At high optical injection, voltage drop at the load impedance decreases the voltage across the device. This in turn results device saturation limiting the output power. The change of the voltage across the device also changes the device capacitance. This phenomenon can be observed from the denser contour plots at high impedance regions in Figure 2.19 (a - i).

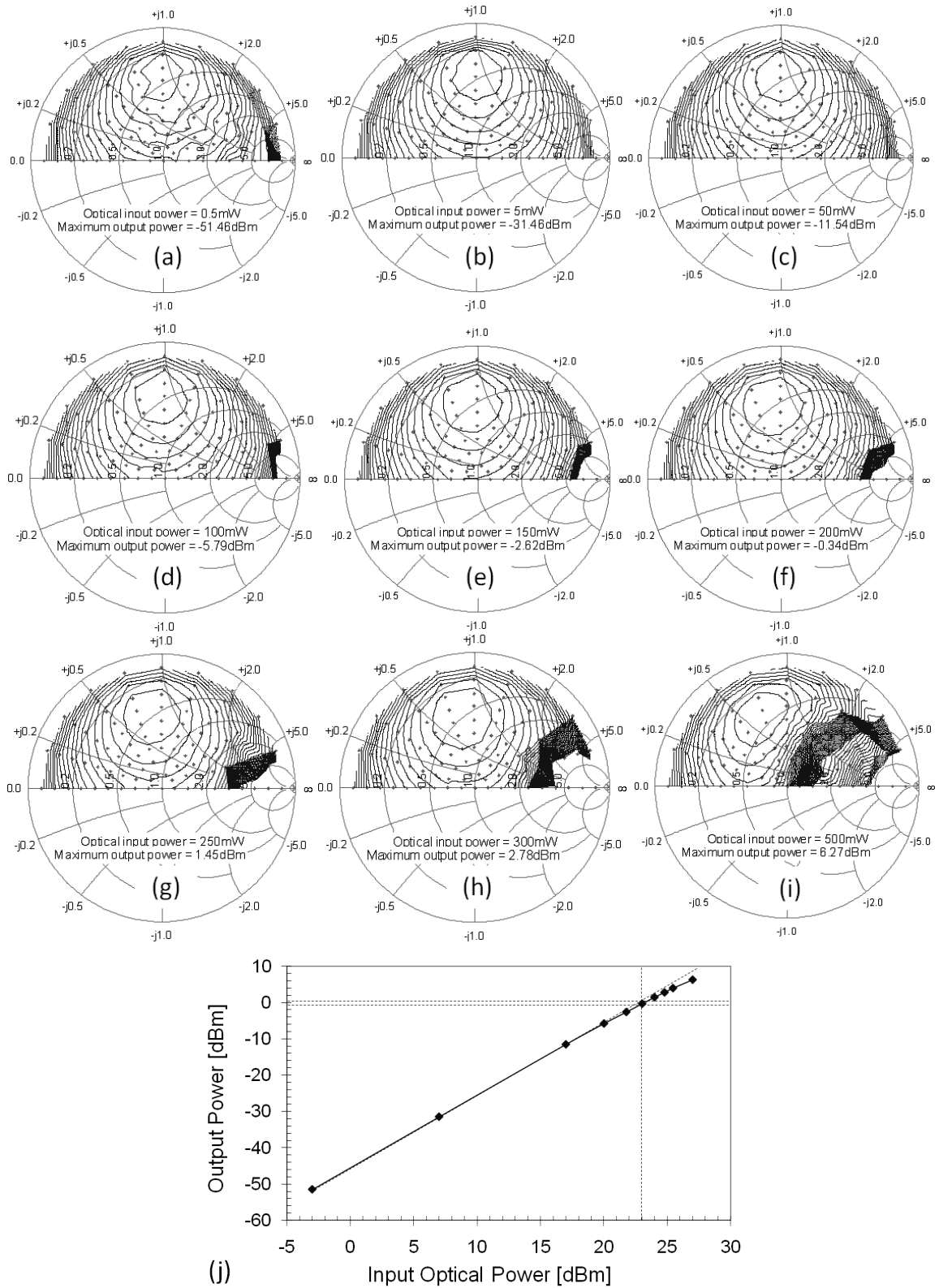


Figure 2.19: (a-i) Contour plots of output power of a 5 μm diameter UTC-PD at different optical input levels. (j) Simulated output power of the UTC-PD by varying the input optical power from 0.5 mW to 500 mW.

2.5 Circuit and device integration

The output power of the UTC-PD is comparatively low at higher frequencies. Optimising a design for output power requires trade-offs involving the epitaxial layer design, optical coupling, circuit design and antenna design. Carefully designed UTC-PD circuits are able to deliver a decent amount of output power for many applications. UTC-PD based circuits for free-space applications require compact planar antennas. Generally, lenses made of silicon, Macor etc are used to ensure efficient coupling of the THz radiation to the free space. Depending on the system bandwidth and power requirements, broadband or narrowband antennas are required. On the other hand, for several applications, for instance using UTC-PD as LO in heterodyne detection systems, the generated THz signal from the UTC-PD is coupled to a waveguide.

The trade-offs, concerning UTC-PD based photomixer circuits, are made based on the required power, bandwidth and system integration. Specific considerations are required if other structures (e.g. matching circuit, antennas) are monolithically grown with the UTC-PD. In order to achieve high power photonic THz generation from UTC-PDs, the following factors are important for realising photomixer circuits:

- Device structure, device area and embedding impedance
- Optical illumination
- Biasing and thermal considerations

In this section, a brief review on photomixer circuit design methodologies is presented followed by several design examples.

2.5.1 Circuit design

Illumination techniques: UTC-PDs can be illuminated by a number of ways, as shown in Figure 2.20. Bottom illumination is the most widely used technique. The technique requires antireflection (AR) coating on the backside. Top illumination has also been reported [65]. In this case, AR coating is applied on the top side while high-reflection (HR) coating is applied at the bottom. Besides simple vertical illumination techniques, a relatively more complex illumination technique has been proposed [40] where two cascade-connected UTC-PDs are injected with a single optical fibre and an integrated 3-dB optical signal splitter. A number of other illumination techniques also exist [66] offering various advantages and disadvantages. In order to realise side illumination, lasers can be directly injected to the absorption layer or utilising the substrate as the optical waveguide, as shown in Figure 2.20 (b-c). Alternatively, a refracting facet can be used for side illumination.

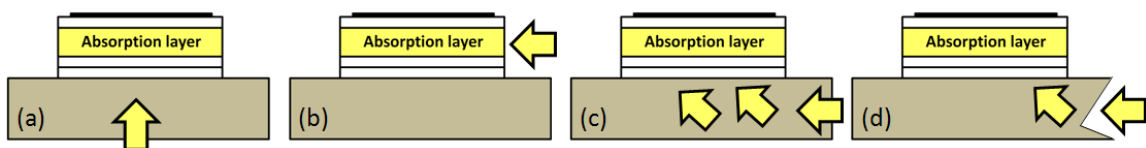


Figure 2.20: (a) Vertical, and (b-d) side illumination techniques for UTC-PDs.

For CW THz generation, the simplest way to obtain optical heterodyning is to use two tunable laser sources. However, the spectral quality of THz radiation generated by photomixing is determined by the quality of the optical beat, which in turn is determined by the frequency stability of the pump lasers. An optical frequency comb generator can also be used accompanied by an optical filter which selects two frequencies [67].

Planar guiding structures: The most common techniques for designing transmission lines include microstrip lines and coplanar waveguides [68]. Due to the illumination requirement of the vertically illuminated UTC-PD, microstrip lines are not suitable. Slot lines and coplanar waveguides (CPW) are widely used in the circuit designs for UTC-PDs. CPWs have lower parasitics than microstrips and are therefore a good choice for high-frequency operations where this is a primary design concern. However, compared to microstrip lines and CPWs, coplanar striplines (CPS) provide higher characteristics impedance [68, 69]. The CPS transmission line has two conductors on the top plane of the circuit, allowing series or shunt elements to be readily integrated into CPS circuits. CPS is often used in electro-optic circuits as well as in high-speed digital circuits. Due to its balanced nature, CPS also makes an ideal feed for radiating elements such as printed dipoles.

Matching circuit: It is possible to implement a matching circuit [40] to improve the output power by compensating for the imaginary part of the internal impedance in the UTC-PD at a particular frequency. However, since the matching circuit works best at a specific frequency, it limits the overall bandwidth of the system. Moreover, for centre-fed antenna designs (e.g. when the UTC-PD is placed at the centre of a twin-dipole antenna), the implementation of such matching circuits is not convenient.

2.5.2 Antenna design

The UTC-PD can be integrated with antennas for THz generation and emission. It has been shown that the output power of the UTC-PD can be maximised by increasing the antenna resistance [70-72]. The output THz power of a biased photomixer can be expressed as:

$$P_{THz}(\omega) = \frac{R_L \mathcal{R}^2 P_{inj}^2 M \mathcal{L}_{OE}}{2 [1 + (\omega\tau_w)^2] [1 + (\omega\tau_{RC})^2]} \quad (2.18)$$

Where R_L is the load resistance, \mathcal{R} is responsivity, P_{inj} is the input optical power, M is related to the modulation index, and \mathcal{L}_{OE} is related to optical and electrical losses [40]. Although the equation is valid only in the small signal limit, it signifies the possibility of getting higher output power with higher antenna resistance. Figure 2.21 exemplifies an equivalent circuit of a biased photomixer with the antenna.

For UTC-PD-antenna integration, different types of antennas such as log-spiral and log-periodic antenna have been reported. However, the impedance of those broadband antennas is relatively low [31, 71, 73, 74]. Resonant antennas such as dipole antennas offer relatively high impedance at the resonant frequency [70, 71]. Photomixing with a resonant twin-dipole antenna has also been reported [46]. If broadband operation is not a prerequisite, antennas having resonant structure can be used to maximise the THz output

power at a specified frequency. Twin-dipole antennas provide symmetric near-Gaussian beam pattern and high directive gain. On the other hand, bow-tie antennas provide relatively larger bandwidth. However, the antennas can be realised in CPW or CPS. In order to bias the UTC-PD, choke filters are required.

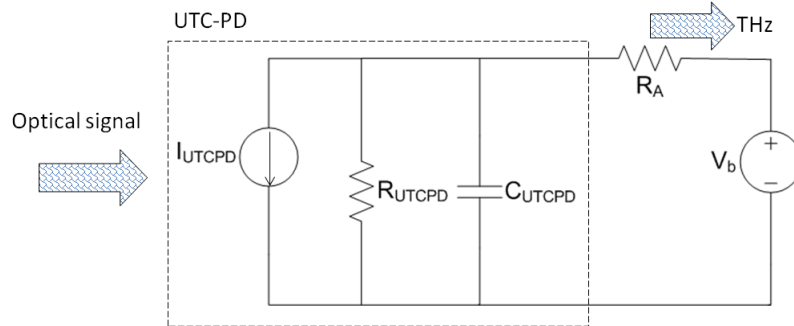


Figure 2.21: Equivalent circuit of a biased UTC-PD with an antenna.

2.5.3 UTC-PD integrated antenna design examples

Optimum embedding impedance ensures maximum power transfer. Therefore in order to generate the maximum power by a UTC-PD at a certain frequency, impedance matching is necessary. For UTC-PD integrated antenna designs, it is necessary that the antenna introduces the optimum embedding impedance to the UTC-PD.

In this section, examples of UTC-PD integrated antenna designs, using CPS, are described. The main motivation of designing the antennas was to have totally parametric designs which can be modified and optimised for a particular UTC-PD at a given operating frequency. The designs also contain choke filters to provide DC bias to the UTC-PD. The designs were performed at 340 GHz. Throughout the investigation, Ansoft HFSS [75] was used.

Example A: A twin-dipole CPS antenna on 150 μm thick InP substrate ($\epsilon_r = 12.5$) with gold conductor (2 μm thick) is designed at 340 GHz [37]. The design also included choke filters and biaspads. Figure 2.22 shows the centre-fed twin-dipole antenna and the corresponding design parameters.

At the first stage, a choke filter, having consecutive sections of high impedance and low impedance, was designed and optimised. This type of choke filter consists of a number of quarter-wave transmission line sections where transmission lines with high and low characteristic impedances are placed consecutively. The presented choke filter is very well suited for planar and single layer design. Since the antenna is of twin-dipole type, choke filters and bias pads are symmetrically placed to attain symmetric beam pattern. This symmetric arrangement will introduce symmetric impedance loading on both sides of the twin-dipole antenna. The choke filter was optimised to obtain the maximum return loss at the desired frequency by varying L_4 . After optimising the choke filter, it was integrated with the twin-dipole antenna and the integrated design was optimised by varying W_d , L_1 , L_2 and L_3 . Table 2.2 shows the optimised parameters for the antenna design. All parameters are in μm .

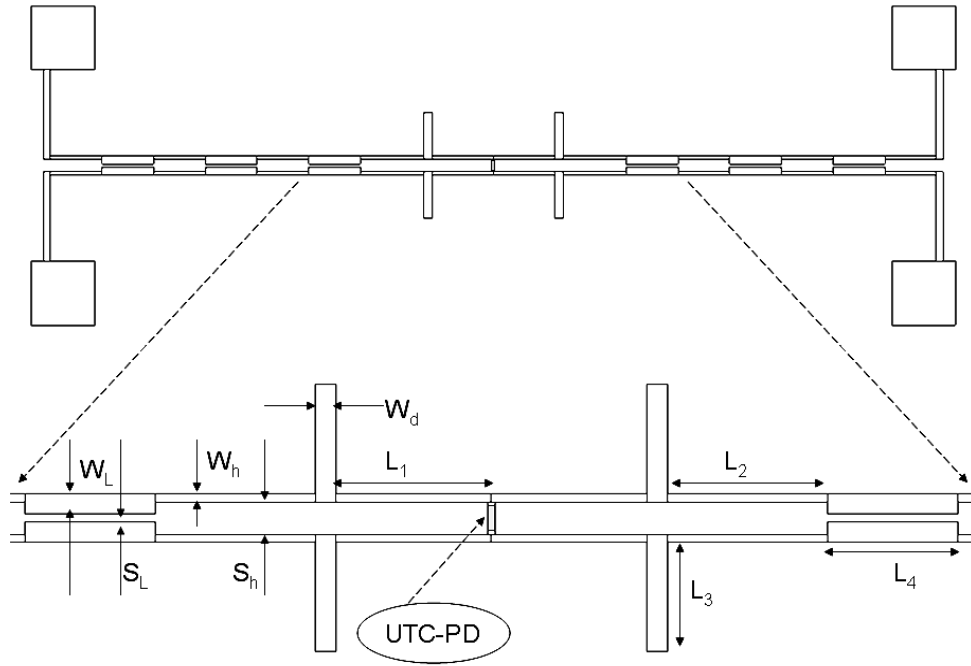


Figure 2.22: UTC-PD integrated twin-dipole antenna with choke filter and biaspads.

Frequency	W_h	S_h	W_L	S_L	W_d	L_1	L_2	L_3	L_4
340 GHz	5	20	12.5	5	10.5	98	111	71	82

Table 2.2: Design parameters (in μm) for the CPS twin-dipole antenna at 340 GHz.

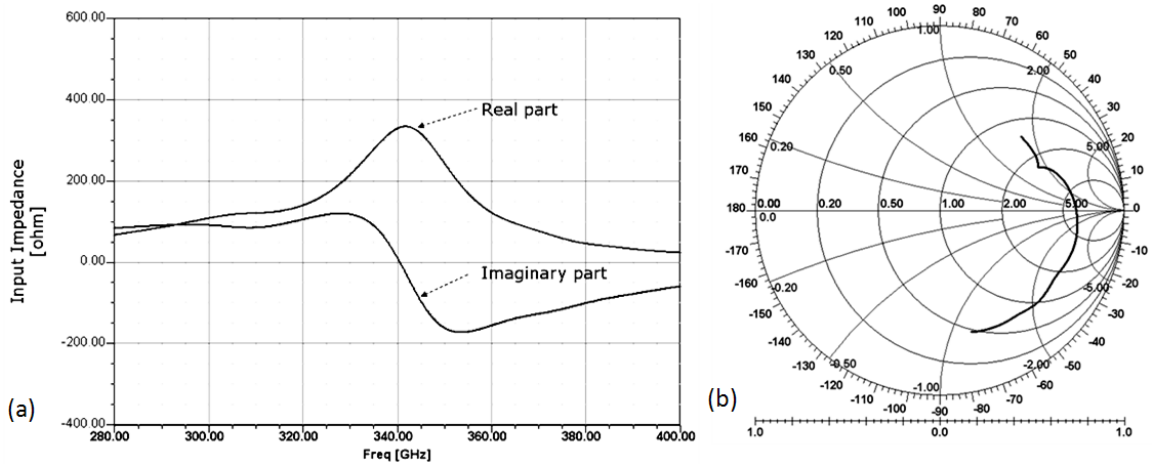


Figure 2.23: (a) Input impedance plot, and (b) Smith plot of the 340 GHz twin-dipole antenna.

Figure 2.23 (a) shows the input impedance of the antenna and pronounced resonance is observed at 340 GHz. Figure 2.23 (b) shows the Smith plot, normalised to 50Ω . The optimised antenna design, hence, provides the scope of eradicating the RC limitation that arises from UTC-PD capacitance. This capacitance can be computed or extracted from the equivalent circuit fit of the S -parameter measurements. The antenna designs then can be optimised to provide the required amount of inductance at a specific frequency and thereby cancel out the UTC-PD capacitance. The high resistance of the antenna will maximise the THz output power from the photomixer.

Several other CPS antennas on 150 μm thick InP substrate with 2 μm thick gold conductor are also designed at 340 GHz with integrated choke filters and biaspads. Figure 2.24 shows the designed bow-tie, dipole and twin-dipole antennas.

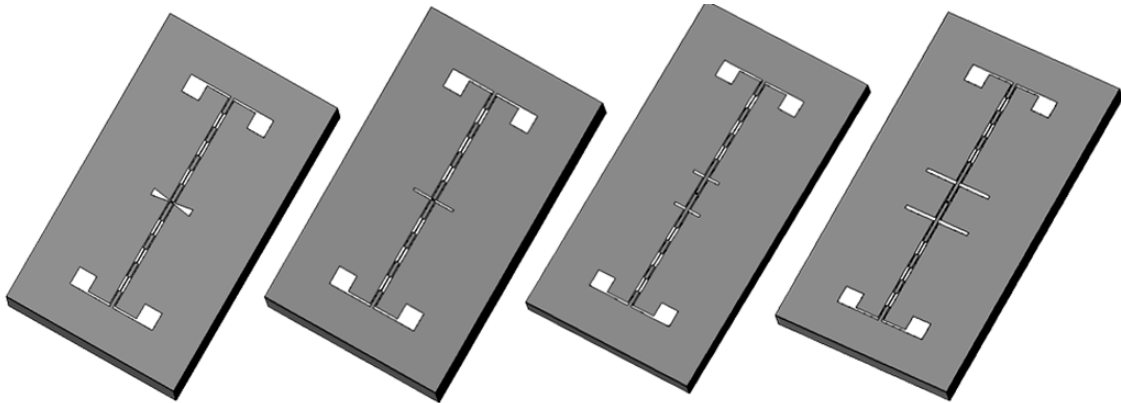


Figure 2.24: A number of designs showing antenna and choke filter integrated UTC-PDs.

Design Example B:

In addition to the above-mentioned antenna designs, an elliptically tapered CPS antenna was designed and analysed as a part of the feasibility study. The main motivation of this work is to establish the proof of concept of integrating UTC-PDs with antennas that can be integrated monolithically and to produce end-fire beam. The antenna is of travelling-wave type. The waves travel down the curved path of the flare along the antenna. In the region where the separation between the conductors is small, the waves are tightly bound and as the separation increases, the bond becomes progressively weaker and the waves get radiated away from the antenna. Figure 2.25 shows the preliminary design of the antenna at 340 GHz with the choke filter and biaspads. The figure also illustrates E-field on cross-sectional planes. The antenna provided $\sim 12\%$ bandwidth ($\text{VSWR} \leq 2$) and $\sim 3\text{dB}$ directivity at 340 GHz. The port impedance was set to 200 Ω . Figure 2.26 shows the return loss and directivity of the antenna.

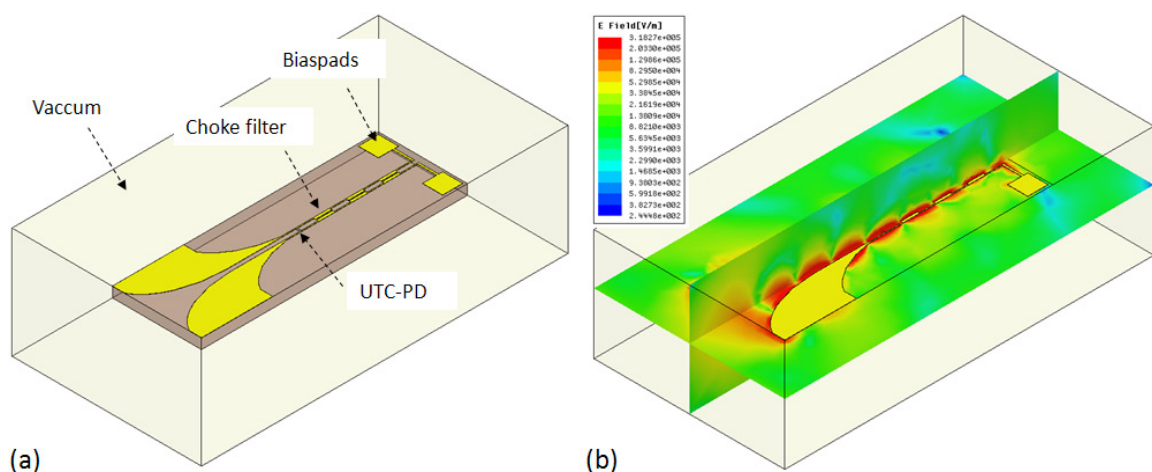


Figure 2.25: (a) The 340 GHz tapered CPS with the choke filter and biaspads (b) E-field distribution at 340 GHz on cross-sectional planes.

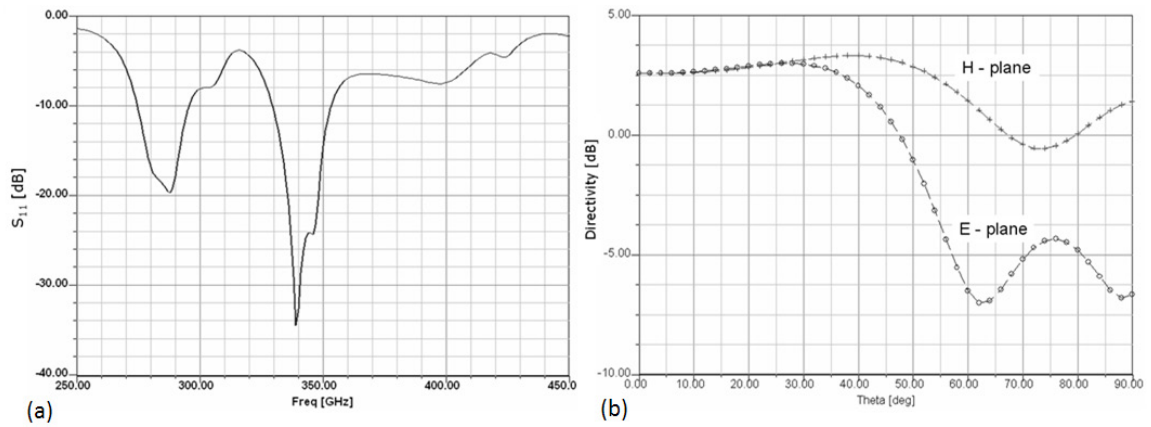


Figure 2.26: (a) Return loss of the tapered antenna, and (b) plot of directivity in E-plane and H-plane at 340 GHz.

Chapter 3. Quasioptical Integration

The broad spectrum of THz applications has attracted researchers from different disciplines. As a result, the THz gap is now being bridged by separately developing research areas. The multidisciplinary nature of the research dealing with THz technologies has induced prompt attentions from various disciplines dealing with optics and photonics, microwave engineering and semiconductor physics. Irrespective the original discipline and for most applications, the essential parts of THz systems are the quasioptical components which facilitate effective THz radiation and/or focusing. Those components include substrate lenses, objective lenses, mirrors etc.

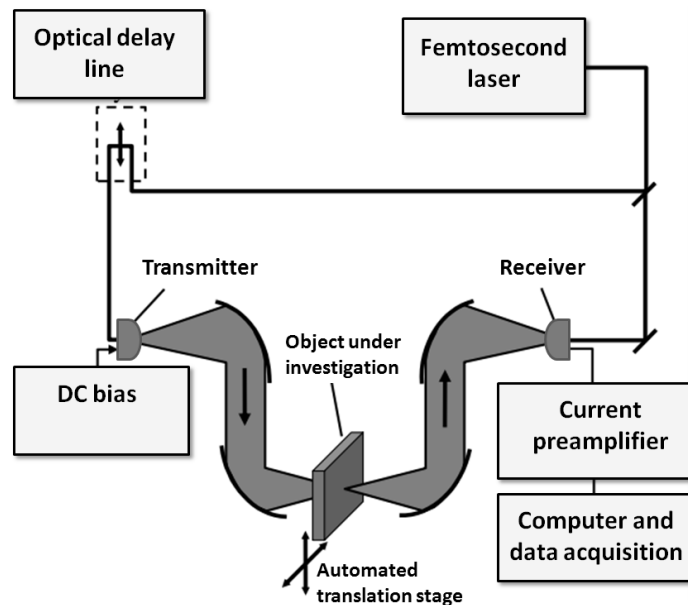


Figure 3.1: A schematic of a typical transmission-mode imaging system showing a number of quasioptical components including lenses and mirrors.

The history of quasioptical components dates back to the 19th century. During the late 1880s, Hertz made an unsuccessful attempt to observe focusing using cylindrical parabolic antennas at 50 MHz. Hertz's experiments were intended to show the similarity between radio waves and visible light. After an extensive modification of the components in 1888, Hertz succeeded in operating at 500 MHz. Compared to his first attempt, the latter involved smaller wavelength which was several times smaller than the dimensions of his apparatus. The emitted radiation could therefore be collimated to a certain extent. With this apparatus Hertz studied polarisation, reflection from a metal surface and refraction by dielectric materials. Few years later, J.C. Bose employed lenses for beam collimation for various experiments at MW frequencies. Bose was in favour of using MW frequencies in order to realise directed beams with relatively small apparatus. Both the scientists had, in principle, constructed the very first quasioptical systems. Their results proved that radio waves (RF/MW) and visible light are similar and are subject of

reflection, refraction, and polarisation etc. At present, quasioptical components often form the substantial part for MW and THz systems. An example of a typical transmission-mode THz imaging system is illustrated in Figure 3.1 showing a number of quasioptical components including lenses and mirrors. In such systems, the EM beam must be collimated and focused with the quasioptical components in order to attain a high resolution and *SNR* for the system. However, the quest for compact THz systems is hindered by conventional quasioptical components due to lack of integration.

3.1 Quasioptical components

THz imaging systems usually employ lenses, parabolic or elliptical mirrors, to create a focus point at a distance [76]. The maximum resolution of these systems is limited by the apertures and the distance. The well-known Abbe limit sets the ultimate spatial resolution to $\sim \lambda/2$ [77] and generally it is not possible to resolve objects less than few wavelengths. The size of the finest detail that can be resolved is proportional to λ/NA , where *NA* is the numerical aperture. As the resolution of an imaging system depends on the wavelength and optics, large *NA* lenses are used at a distance to create a focus [78, 79]. Mirrors are also used to focus or collimate a beam. However, the required optical path, bulky quasioptical components and stringent setups do not favour compact THz systems.

Planar THz antennas are almost always accompanied by lenses, made from suitable dielectric materials. Dielectric lenses can be integrated with planar radiating or receiving elements [80, 81]. Antenna- or detector-lens configurations are an attractive solution for THz technologies and therefore their use has become a common practice to improve the power coupling from/to the antennas. However, the existing substrate lenses are not capable of creating any focus. Therefore, additional collimating and focusing components are required sacrificing the system integration and compactness.

In contrast to the focusing modalities in the THz frequencies, lenses and mirrors loose applicability in the MW regime due to large dimensions and lack of integration. The focusing, in this case, is usually obtained synthetically by space-time beamforming employing a number of antennas [126]. The antennas should efficiently focus the MW signal onto the target and collect the back-scattered energy. However, the use of quasioptical focusing components in MW frequencies hinders compactness and system integration. Although technologies such as metamaterials [82] are interesting, those pose practical challenges regarding manufacturing and integration.

A compact, integrated and robust solution to focus the EM beam is highly desirable in order to achieve greater ease of system construction and integration. It is apparent from the previous discussion that the existing solutions do not favour compact THz systems. Therefore, an advantageous approach is exploring the possibilities of redesigning the quasioptical components for MW or THz applications. Latest engineering materials have interesting electrical, mechanical and thermal properties. Although those materials are primarily being designed and manufactured for mechanical applications, other application areas are reaping the benefits. Many of those materials are machinable and provide moderate permittivity as well as low dielectric loss. Therefore, a new possibility has arisen to design and optimise quasioptical components for MW or THz applications.

3.2 The catadioptric lens

A catadioptric optical system [83] combines refraction and reflection usually via lenses (dioptrics) and curved mirrors (catoptrics). Catadioptric combinations are used in search lights, early lighthouse focusing systems, optical telescopes, and telephoto lenses etc.

The proposed catadioptric lens, shown in Figure 3.2, utilises reflection and refraction caused by the difference in permittivity of the lens and surrounding medium. Thus lens is able to focus a beam in the close vicinity and provides an alternative solution to be used as a focusing element. The lens and its focal length are electrically small (in the order of few wavelengths). Radiating elements and sensors can be physically coupled to the lens in order to achieve short-range focusing ability, therefore, enabling a compact system. Thus, the lens provides greater ease of system integration compared to the conventional quasi-optical components. The lens is circularly symmetric and facilitates the possibility of achieving symmetric beam pattern, which is important for imaging purposes.

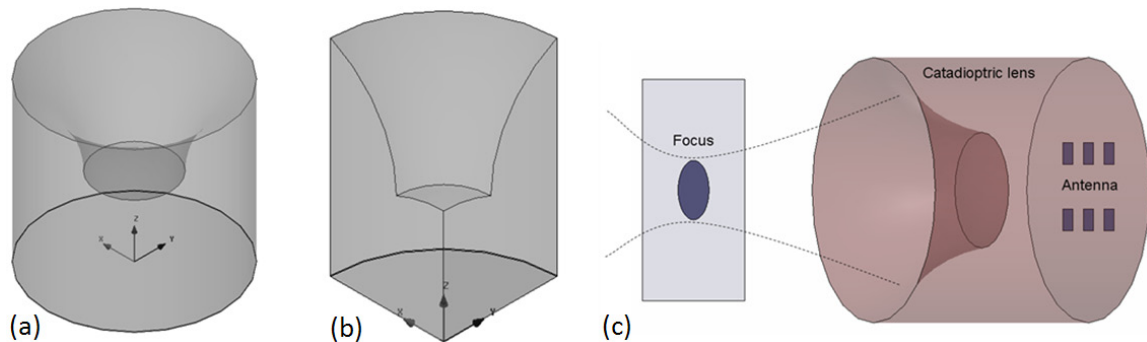


Figure 3.2: (a) 3-D view of the catadioptric lens, (b) cross-sectional view, and (c) Catadioptric lens coupled imaging antenna array.

3.3 Design and analysis of the catadioptric lens

In this section, the catadioptric lens geometry and its dimensions are discussed. In the first part of this section, a simple approach is taken to describe the working principle of the catadioptric lens. The well known Snell's law and the total internal reflection are used to illustrate the focusing of the catadioptric lens. In the latter part, a brief overview of the performed 3D EM analysis is presented.

3.3.1 Basic principles of the lens

The proposed catadioptric dielectric lens consists of a hemispherical part with a “horn like” extension on top of it, as shown in Figure 3.3. This extension causes total internal reflection due to the differences in the permittivity of the lens material and the surrounding medium. The reflected beams are then refracted at the conical interface. Therefore the extension is referred as the catadioptric portion. Figure 3.3 shows the catadioptric lens geometry where the lens is placed at the origin of the Cartesian coordinate system and the surrounding medium is assumed to be vacuum/air. The catadioptric portion is realised as a part of a circle which is referred as “catadioptric circle”. This circle is located at an offset (L_{offset}) from the outer boundary of the lens. As

the outer boundary is the interface between two mediums, reflections and refractions occur at the interface. Therefore the interface is denoted as the “reflection plane”. The radius of curvature of the hemispherical part and the catadioptric part are denoted as R_L and R_C , respectively. The length of the catadioptric portion is denoted as L_C . When $A1$, $A2$, $A3$ rays are launched from the source, they face total internal reflection at the “reflection plane” and the reflected rays are denoted as $B1$, $B2$, $B3$ respectively. These rays are refracted along the interface of lens or air and the refracted rays are denoted as $C1$, $C2$, and $C3$.

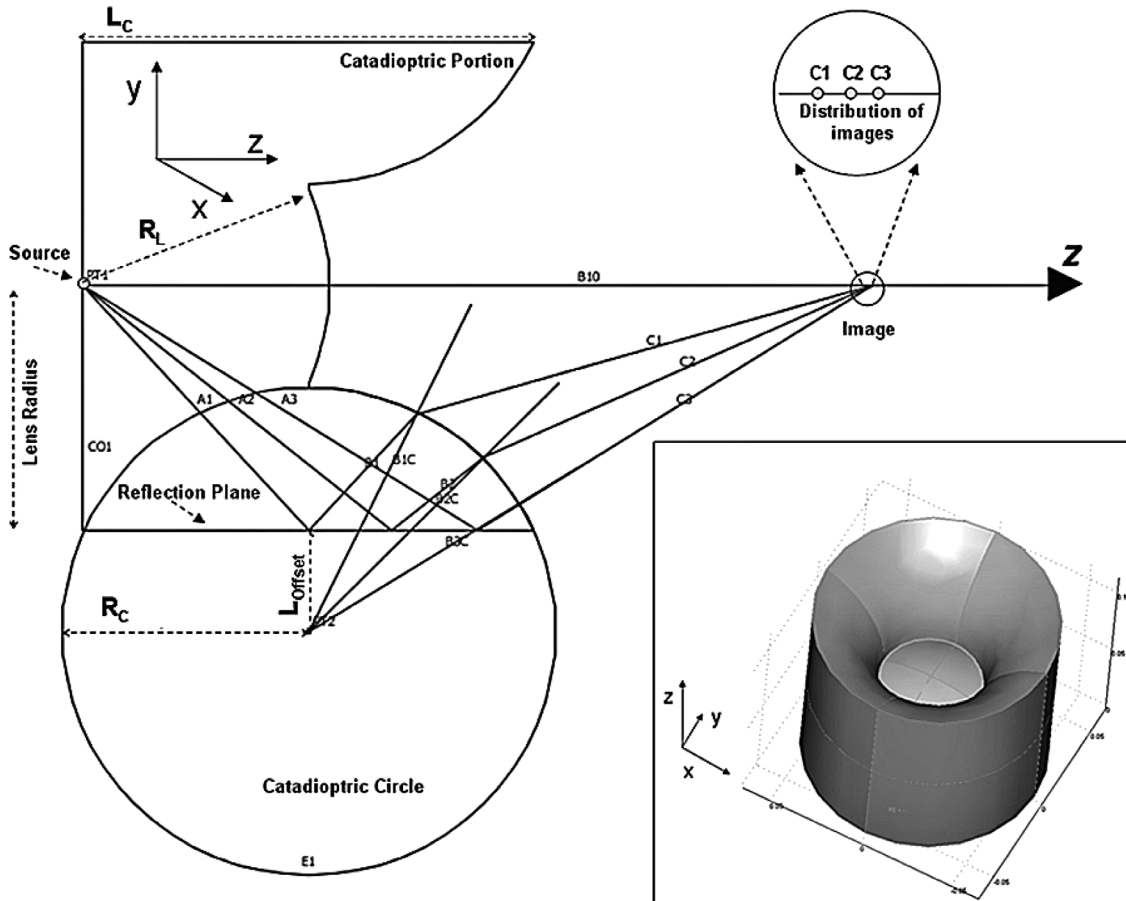


Figure 3.3: Catadioptric lens geometry and distribution of images. Inset is the 3D view of the catadioptric lens.

For certain placement of the catadioptric circle and its radius, the refracted rays will converge to a point along Z axis. In principle it's possible to determine an elliptic extension as the catadioptric portion but for simplicity only circular extensions are considered here. As a circular extension has been used, the refracted rays may not necessarily converge to a single point. Rather a distribution of closely spaced intersection points of refracted rays and symmetry axis (Z) will produce a focus region. The relative intensity and the area of the focus region are highly dependent on the location of the catadioptric circle (L_{offset}), its radius (R_C), and on the location of the reflection plane which is defined by the radius of the lens R_L .

3.3.2 3D EM analysis

Different kinds of computational techniques have been developed based on geometrical or physical optics for determining near-field [84, 85] and far-field pattern [86, 87], internal reflections [88], input impedance [89], S parameters, focusing property [90] and the imaging properties [91] of dielectric lenses. A common practice for designing dielectric lens loaded antennas is to replace the lens with a semi-infinite dielectric half-space. A number of approximations are made while analysing lenses and lens-antennas. Compared to electrically large or moderately large lenses, electrically small lenses pose greater challenge in terms of computational complexities.

3D full-wave EM solvers have been used to analyse the performance of the catadioptric lens. A 3D full-wave Finite Element Method (FEM) software package, Ansoft HFSS [75], was used to determine the performance of the catadioptric lenses. At a later stage of the study, a Finite-difference time-domain (FDTD) software package, CST Microwave Studio [92], was used.

Numerical techniques such as FEM and FDTD involve volume meshing. Therefore, the number of unknowns increases with the cube of the linear meshing density. Computational time and required resources scale with number of unknowns. FDTD is a popular computational electrodynamics modelling technique. Since it is a time-domain method, solutions can cover a wide frequency range with a single simulation run. For certain cases, FEM methods are claimed to be more accurate [93] than FDTD. For resonant structures, FEM is particularly efficient. On the other hand, FDTD can solve large computational domains which are extremely challenging for FEM. Therefore the FDTD method was found to be more time efficient in analysing the catadioptric lens.

3D EM analysis Example: A simulation example of a catadioptric lens is presented here briefly. A silicon catadioptric lens ($\epsilon_r = 11.9$) of $R_L = R_C = 6$ mm and $L_C = 11$ mm was analysed in Ansoft HFSS and the focusing property of the lens was studied from 50 GHz – 60 GHz.

The nearfield and farfield properties of a lens are highly dependent on the feeding antennas. In the present case, a dielectric filled ($\epsilon_r = 11.9$) circular waveguide was used as a source which was coupled to the back of the catadioptric lens in order to realise a benchmark setup and also to reduce computational complexities. The setup has been illustrated in Figure 3.4. The waveguide was excited at the fundamental mode (TE_{11}) and symmetry boundaries were used in the analysis. Within the considered frequency span, the lens produced the most intense focus region at 51.8 GHz. At this frequency the lens diameter D_{lens} ($2R_L$) is $\sim 2\lambda_0$ or $\sim 7\lambda_{si}$ where λ_0 is free-space wavelength and λ_{si} is the wavelength in silicon. The length (L_C) of the lens is 11mm which corresponds to $\sim 2\lambda_0$ at 51.8 GHz.

Further discussions and results regarding 3D EM analysis of the lenses are provided in the following sections.

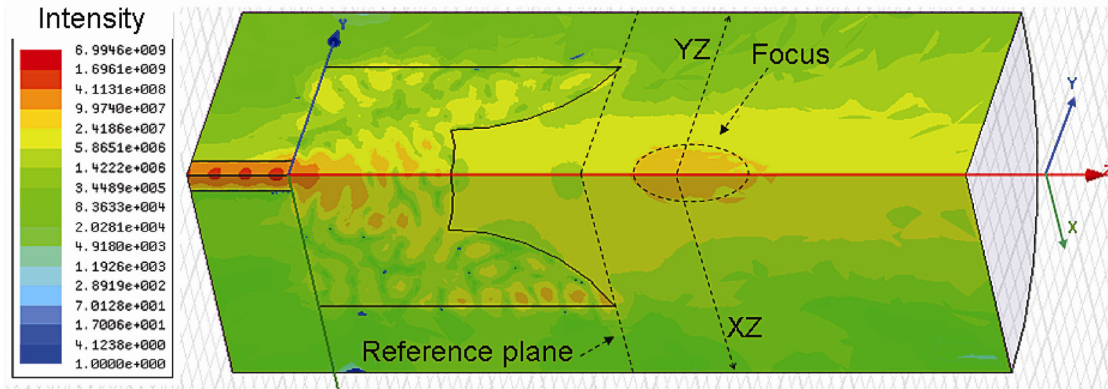


Figure 3.4: Intensity plot at 51.8 GHz and the focus point of a silicon catadioptric lens with $R_L = R_C = 6$ mm.

3.3.3 Design issues

As discussed before, focusing is obtained in catadioptric lenses using both reflection and refraction. Ideally, if the catadioptric lens is fabricated from a suitable material, e.g. glass, and has arbitrarily large dimension, the lens will effectively focus the incoming light. This can be visualised in Figure 3.3. When the lens is coupled to a RF source (e.g. an antenna), the focusing of the lens will depend on how the fields are being coupled to the lens and the electrical dimension of the lens at that particular frequency. Furthermore, the electrical dimension, which is related to the dielectric constant of the lens material and the physical dimension, is a determining factor for the focus intensity at a particular frequency. Although electrically small catadioptric lenses are able to focus, the focus in fact becomes more intense at higher frequencies when the lens dimension becomes electrically large. Therefore there is a correlation between the intensity of the focus and the electrical dimension of the lens. Furthermore, as the lens utilises reflection, the permittivity of the lens material should be high in order to obtain a large difference in refractive indexes in relation to the surrounding medium (air). Therefore, it is necessary to use materials having high permittivity in order to realise compact lenses. Moreover, the material should be machinable, which is usually in contradiction to the materials with high permittivity.

3.3.4 Lens fabrication

In the recent years, a broad spectrum of engineering materials is being used in different disciplines. Many of these engineering materials are machinable. However, a few machinable materials provide moderate permittivity and low dielectric loss. These materials are of particular interest for fabricating catadioptric lenses and discussed below.

Within the framework of this thesis, Delrin and Macor were used in fabricating catadioptric lenses. Delrin [94], also known as polyoxymethylene (POM) and polyacetal, is a polymer. Delrin is a lightweight, low-friction, and wear-resistant thermoplastic with good physical and processing properties. Its relative permittivity is 3.8 while the dielectric dissipation factor is 0.008. Macor [95] is a machinable glass-ceramic and has similar mechanical properties as Delrin. However, the relative permittivity of Macor is

5.6 while the dielectric dissipation factor is 0.007. Both Delrin and Macor are machinable using ordinary tools and extremely high accuracy can be achieved. In addition to Delrin and Macor, a catadioptric lens was fabricated from silicon. However, the machining silicon is extremely challenging and requires special tools. Therefore, more elaborate investigations were carried out using lenses fabricated from Delrin and Macor. Figure 3.5 shows the fabricated catadioptric lenses.

The losses of those materials become significant at higher frequencies. Although no measurement data is available, it is reasonable to extrapolate that the losses of the materials will hinder the performance of a catadioptric lens at higher frequencies.

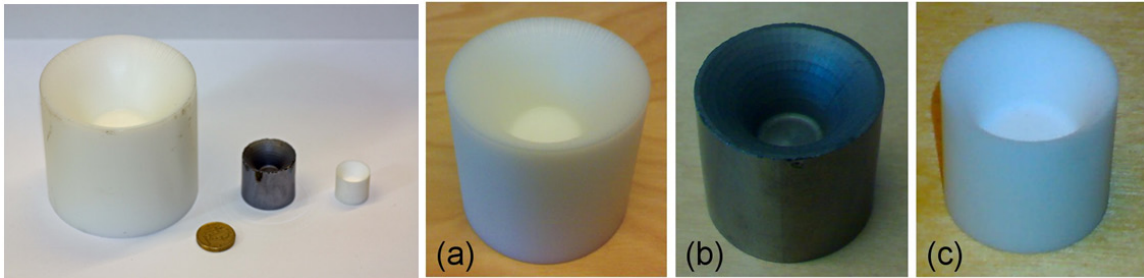


Figure 3.5: Fabricated catadioptric dielectric lenses (a) Delrin, $D = 80$ mm (b) silicon, $D = 28$ mm and (c) Macor, $D = 18$ mm. Here D is the diameter of the lens.

3.4 Characterisation techniques

Microwave and millimetre-wave field probing are being used for determining performance and failure analysis in antennas, microwave circuits etc. Monopoles, dipoles, horns etc. are usually used as probe. Coaxial probes have shown promising results [96]. Electrooptical probing systems provide a very wide bandwidth and a good resolution [97]. However, MW and mmw field probing are challenging due to the complicated methods and complex probes.

Within the framework of this thesis, two simple characterisation techniques were implemented for field probing of the lens coupled antenna. The first technique is a qualitative approach where a metallic reflector was placed at different positions in front of the lens-antenna and 1-port measurements were performed using a VNA. The main approach of this characterisation setup was to determine the amount of reflected power by the metallic reflector at different positions. The approach is similar to the monostatic radar. The received power of a radar can be written as:

$$P_r = \frac{P_t G_t}{4\pi R^2} \cdot \frac{\sigma}{4\pi R^2} \cdot A_e \quad (3.1)$$

The first factor on the right represents the power density at a distance R from an antenna that radiates a power P_t with gain G_t . The numerator, σ , of the second factor is the radar cross section of the target. The denominator of the second factor accounts for the divergences of the reflected signal on its return path back to the antenna. A_e is the effective area of the antenna. Although the formula is valid at farfield, it provides insight regarding the characterisation setup. P_r decreases with R^4 . Therefore, the roll-off of P_r for

a certain target should be monotonous. For the lens-antenna, if there is no focus, the P_r would roll off with distance. On the other hand, a focus perturbs the roll-off profile.

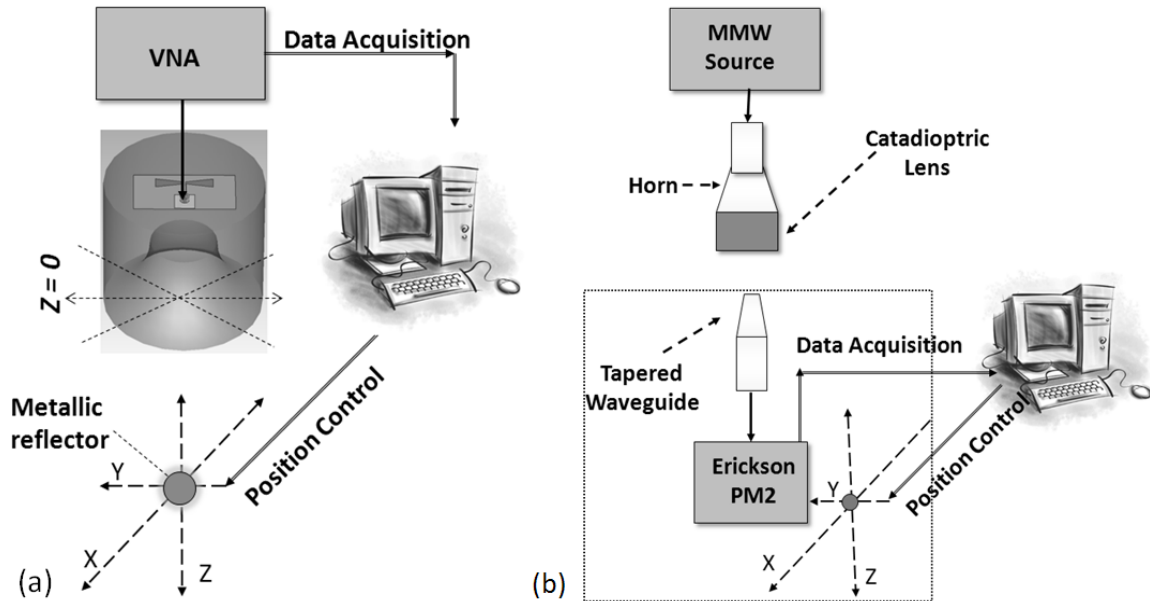


Figure 3.6: (a) Reflection-mode, and (b) transmission-mode characterisation techniques.

Figure 3.6 (a) shows the reflection-mode characterisation setup. A 10 SEK metal coin (diameter = 20 mm) was used as the reflector and was placed in front of the lens-antenna at different positions using an automated 3-axis stage. 1-port measurements were performed using a VNA. Measured data were acquired by a computer for post-processing.

For high frequency characterisation, a transmission-mode technique was used. Figure 3.6 (b) shows the setup. An open-ended rectangular waveguide probe, connected to an Erickson Power Meter (PM2), was used as the RF-detector. In order to reduce standing waves, a knife-edge profile for the waveguide probe was realised by thinning the sidewalls using a file. For field mapping, the probe and the power meter were mounted on a computer-controlled 3-axis stage. Measured data were acquired by a computer for post-processing.

3.4.1 Microwave characterisation

With a view to study the focusing properties of the catadioptric lens in MW frequencies, the 80 mm diameter catadioptric lens made of Delrin ($\epsilon_r = 3.8$) was coupled to bow-tie slot antennas, as shown in Figure 3.7. In this section, simulations and characterisation results are presented. Furthermore, preliminary characterisation results are also presented for a lens coupled WR22 horn antenna.

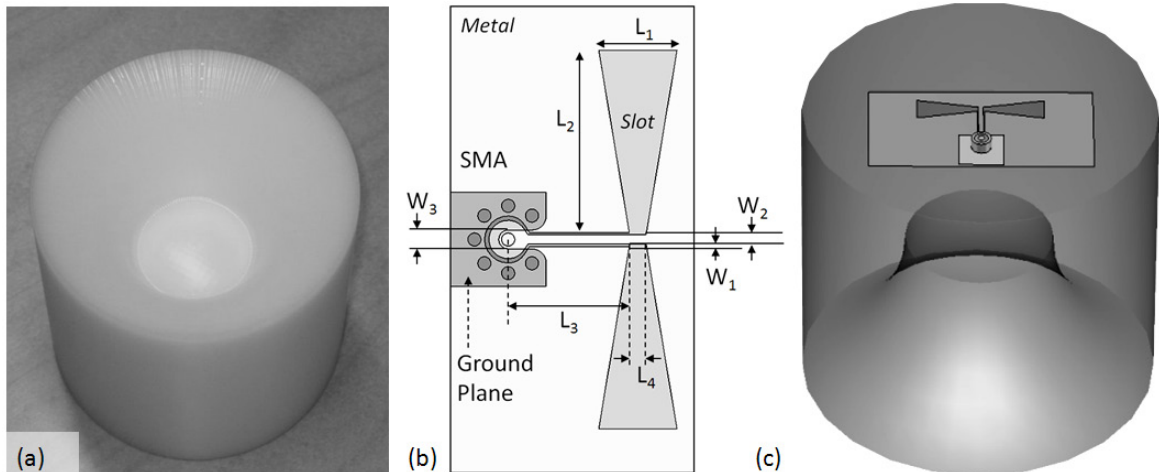


Figure 3.7: (a) Photograph of the fabricated 80 mm diameter Delrin lens. (b) Design of the bow-tie slot antenna, and (c) the bow-tie antenna coupled catadioptric lens.

Lens coupled 5 GHz bow-tie antenna: As a preliminary feasibility test, an 80 mm diameter Delrin lens was coupled to a 5 GHz bow-tie slot antenna. Simulations and measurements of the far-field at 5 GHz and return loss versus frequency using the bow-tie antenna are presented in Paper E.

The investigation was limited to low frequencies (<10 GHz) in order to be able to compare simulation and measurement results. The lens was analysed in the frequency domain by using Ansoft HFSS at around 5 GHz. At this frequency, the lens diameter D_{lens} ($2R_L$) is $\sim 1.3\lambda_0$ or $2.6\lambda_{\text{del}}$ where λ_0 is free-space wavelength and λ_{del} is the wavelength in Delrin.

The lens is small in terms of the wavelength and the permittivity of the lens material is quite low. The focusing property of the catadioptric lens, however, was not determined. The far-field radiation patterns are investigated and presented at 5 GHz.

The findings and results have been reported in Paper E.

Lens coupled 8.5 GHz bow-tie antenna: At this stage, the 80 mm diameter Delrin lens was coupled to an 8.5 GHz bow-tie slot antenna. The focusing property of the lens is studied experimentally.

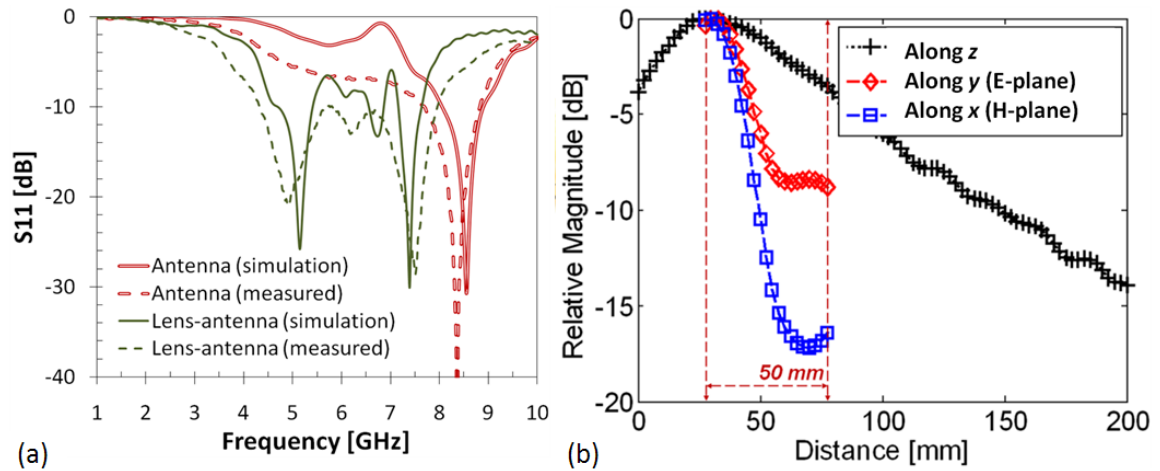


Figure 3.8: (a) Simulated and measured return loss of the antenna and the lens-antenna, and (b) measured axial and spatial profiles of the lens-antenna.

CST Microwave Studio was used to analyse and predict the performance of the lens. The simulations were done from 1 GHz to 10 GHz for both the antenna and the lens-antenna. The simulated and measured return loss of the antenna and the lens-antenna are shown in Figure 3.8 (a). The results show good agreement. The bow-tie antenna provides $\sim 15\%$ bandwidth. Due to the permittivity of the Delrin lens, a frequency shift can be observed for the lens-antenna configuration. The measurement results show that the lens-antenna provides $\sim 60\%$ bandwidth while simulations predicted $\sim 50\%$ bandwidth, both centred at ~ 6 GHz. At this frequency ($\lambda_0 \sim 50$ mm), the lens diameter D_{lens} is $\sim 1.6 \lambda_0$ or $\sim 3.1 \lambda_{\text{Delrin}}$ where λ_0 is free space wavelength and λ_{Delrin} is the wavelength in Delrin. The results indicate that the lens-antenna provides 4 times wider bandwidth than that of bow-tie antenna. The discrepancies between the simulation and measured results are mainly attributed to the uncertainty in permittivity of the Delrin lens and mode conversion from microstrip to CPW in the bow-tie antenna.

The characterisation setup, shown in Figure 3.6 (a), was used to study the focusing of the lens-antenna both in frequency and time domain. The S_{11} parameters from 1 GHz – 10 GHz, obtained by the 1-port measurements placing the coin at different x , y and z positions, were converted into time domain by inverse Fourier transformation. The time domain signals were then used to determine the amplitude of the reflected power by the coin at different positions. The axial and spatial profiles, illustrated in Figure 3.8 (b), indicate that the lens-antenna provides a focus at $z \sim 30$ mm while maintaining a 3-dB spatial discrimination at ~ 10 mm.

With a view to study the focusing at different frequencies, reflected signals at different discrete frequencies were studied from 1 GHz to 10 GHz with 1 GHz step. The lens-antenna provides broadband focusing from 5 GHz – 10 GHz.

The findings and results have been reported in Paper C.

Lens coupled WR22 horn antenna: Preliminary measurements of a catadioptric lens in the WR22 (33 GHz – 50 GHz) frequencies were performed and reported in Paper D. The focusing property was determined by backscattering method using a metallic reflector. The characterisation setup was similar to the one shown in Figure 3.6 (a). Figure 3.9 (a) shows the catadioptric dielectric lens, WR22 horn antenna and the coin (diameter = 20 mm), used for backscattering measurements.

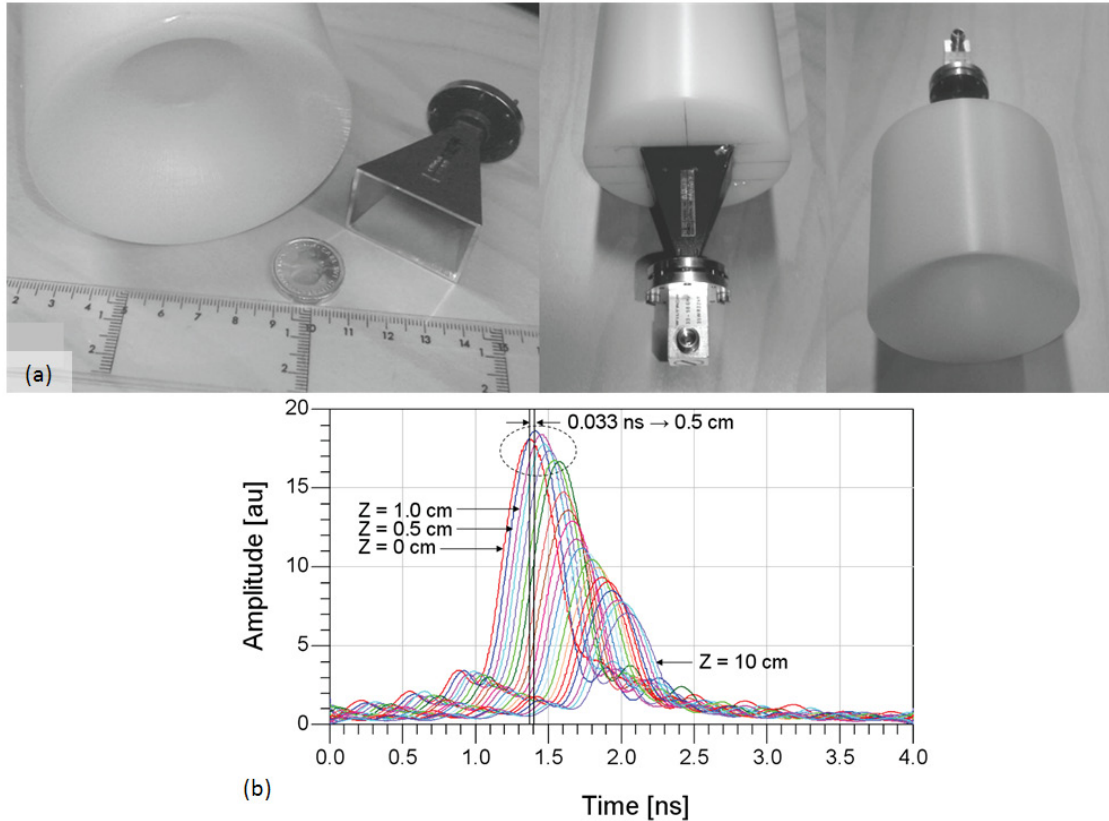


Figure 3.9: The catadioptric dielectric lens, WR22 horn antenna and the coin, used for backscattering measurements. (b) Reflected signals by the coin at different Z positions in time domain, obtained by inverse Fourier transformation of S_{11} parameters from 40 GHz to 43 GHz.

A HP 8510C VNA was used to perform 1-port measurements. Obtained S_{11} parameters were converted into time domain by inverse Fourier transformation and the amplitude of the reflected signal was investigated in time domain. Figure 3.9 (b) shows the amplitude of the reflected signal at different positions. The maxima of the reflected signals at different positions correspond to the positions of the coin along Z direction. For instance, the maxima of the reflected signals for $Z = 0$ cm and $Z = 0.5$ cm are 0.033 ns apart. This translates to a total distance of 1.0 cm which includes 0.5 cm distance of travel in forward direction and another 0.5 cm distance of travel in the backward direction. As can be seen in Figure 3.9 (b), when the coin is placed at relatively farther position the reflected amplitude decreases with the distance. However, a focus is observed between $Z = 0.5$ cm and 1.0 cm where the amplitude of the reflected signal is even higher than that of $Z = 0$ cm. Therefore, the figure provides qualitative information regarding the focus of the catadioptric lens.

The findings and results have been reported in Paper D.

3.4.2 Millimetre-wave characterisation

In the published work, Paper B, simulation and experimental characterisation results of an 18 mm diameter catadioptric lens at W band frequencies have been presented. The lens was fabricated from Macor ($\epsilon_r = 5.6$), shown in Figure 3.10 (a). The frequency 108 GHz ($\lambda_0 = 2.78$ mm) was chosen for characterisation and measurement purposes due to the available source.

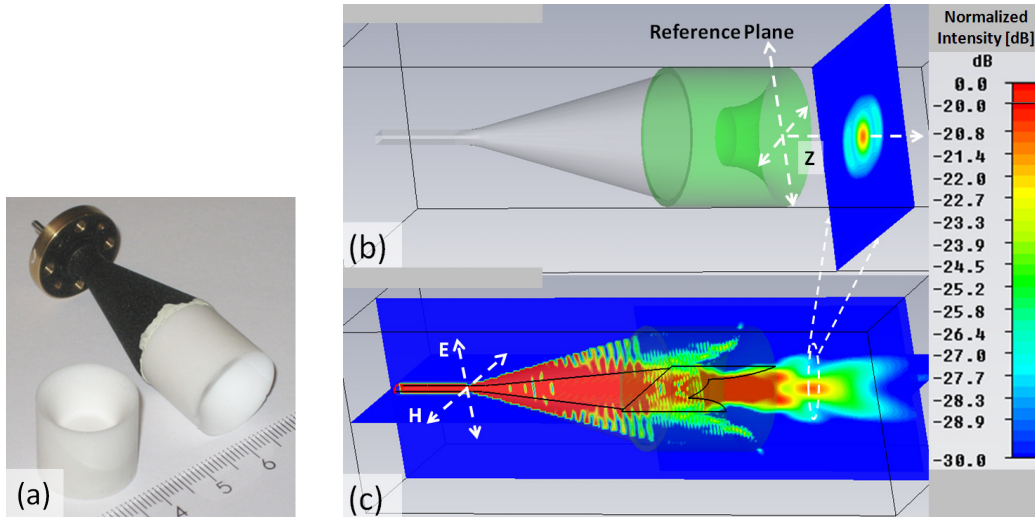


Figure 3.10: (a) the fabricated 18 mm diameter catadioptric lens along with the lens-horn (WR-10 standard gain conical horn) configuration. (b) Simulation setup for the lens-horn configuration and intensity plot at the focal plane. (c) Simulated intensity plot along E-plane and H-plane. The simulation was performed at 108 GHz.

Figure 3.10 (b) shows the simulation setup of the catadioptric lens fed by a WR-10 conical horn. Symmetry-planes along E-plane and H-plane were used in order to reduce computational time and complexities. Perfectly matched layer boundaries were used, otherwise. Figure 3.10 (c) illustrates the simulated normalised intensity plot at 108 GHz along E-plane and H-plane where a focus region is observed. Figure 3.10 (b) also shows the normalised intensity plot at the focal plane. At this frequency, the lens diameter D_{lens} is $\sim 6.5 \lambda_0$ or $\sim 15 \lambda_{\text{MACOR}}$ where λ_0 is free space wavelength and λ_{MACOR} is the wavelength in Macor.

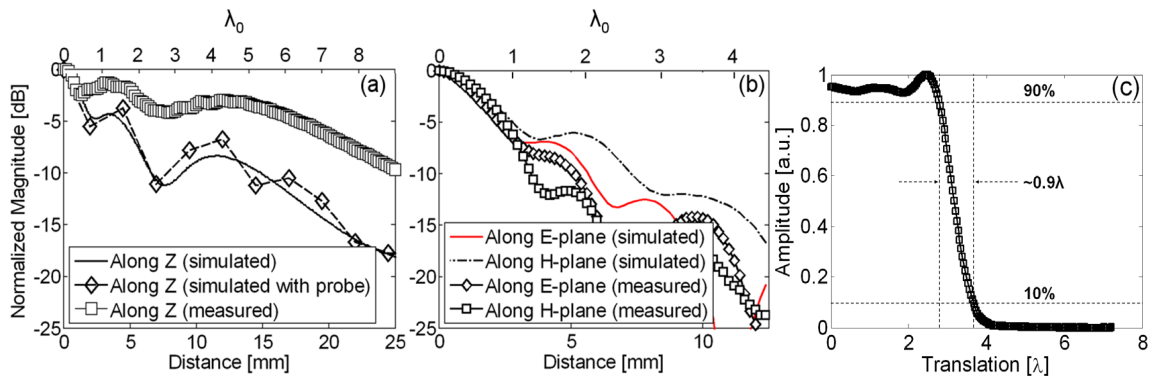


Figure 3.11: Simulated and measured field pattern at 108 GHz along (a) Z axis, and (b) E-plane and H-plane at $Z = 12$ mm. (c) Normalised power transmission during a scan of an aluminium screen edge across the focus.

The characterisation setup, shown in Figure 3.6 (b), was used for the lens-horn characterisation. The source consists of an Agilent E8257D PSG signal generator, a Spacek high power amplifier and a Heterostructure Barrier Varactor (HBV) tripler [98]. The source, set to 10 mW output power, was used to feed the lens, coupled via a conical standard gain horn (W-band). Figure 3.11 (a) shows the normalised intensity plot in dB at 108 GHz along Z axis attained by simulations and measurements. In order to account for the probe, simulations were also done placing a probe at different positions along Z axis and normalised S_{21} (in dB) is plotted. The measurements were done at 0.1 mm steps. Both the simulated and measured profiles indicate focus regions at $Z \sim 3.5$ mm and ~ 12 mm. However, from the practical application point of view, the foci at the farther points are more interesting. Moreover, the simulated intensity plot, shown in Figure 3.10 (c), indicates that the second focus is more radially symmetric and well-defined. Figure 3.11 (b) shows the simulated and measured lateral intensity profiles along E-plane and H-plane at $Z = 12$ mm ($\sim 4.5\lambda_0$). The figure indicates that the lens provides 3-dB spatial discrimination at ~ 2 mm or $\sim 0.7\lambda_0$. The agreement between measured and simulated intensity profiles is reasonable. The discrepancies can be attributed to the uncertainties of the material parameter (Macor), horn model, lens-horn interface and to perturbation of the nearfield while using the probe.

In order to determine the focal diameter of the lens-horn, the edge of an aluminium screen was moved across the focus ($Z = 12$ mm). The 10%–90% rise in the transmitted power occurs over $\sim 0.9\lambda_0$, which provides a measure for the focal spot size [99]. Figure 3.11 (c) shows the normalised power transmission during a scan of the aluminium screen edge across the focus.

The findings and results have been reported in Paper B.

3.4.3 Thermal mapping

Thermal mapping is a technique by which the spatial variation of the surface temperature is measured using a high resolution infrared thermometer. High resolution thermal mapping can be achieved by using liquid crystals (LC) and is primarily used for micro-thermography of integrated circuits [100]. LCs have a number of phases. The helical structure of the chiral nematic phase has the ability to selectively reflect light of wavelengths equal to the pitch length. However, the pitch is temperature dependent. A change in temperature results in an alteration of the wavelength of reflected light according to the temperature. This phenomenon enables to build a liquid crystal thermometer that displays the temperature of its environment by the reflected colour. LCs often used to create sensors with a wide variety of responses to temperature change. Such sensors can be used in the form of heat sensitive films to detect flaws in circuit board connections, fluid flow patterns, and the presence of radiation etc.

In addition to the previously presented characterisation techniques, the thermal mapping technique was explored in order to determine the focusing ability of the catadioptric lens. Figure 3.12 (a) shows characterisation setup. The 80 mm diameter Delrin catadioptric lens was coupled to a WR22 horn, as shown in Figure 3.9. An Agilent E8257D PSG signal generator and a Spacek high power amplifier were used to feed the lens coupled horn at 40 GHz. For thermal mapping, a commercially available liquid

crystal Mylar sheet ($20^{\circ}\text{C} - 25^{\circ}\text{C}$) was used. The LC sheet had 3 to 5 micron sized crystals dispersed within a polymer matrix and exhibits colour change in the visual spectrum. During the characterisation procedure, it was noticed that the LC sheet does not exhibit any colour change under 40 GHz high power radiations. This phenomenon is understandable since losses, introduced by the LC sheet, are small at such low frequency and therefore the corresponding change in temperature was not visible. However, the LC sheet was able to exhibit colour change when it was attached to a MW absorber, as shown in Figure 3.12 (b). This phenomenon can be explained by the losses introduced by the absorber. Under radiations, a localised temperature rise takes place due to the low thermal conductivity of the absorber. A LC sheet translates the spatial temperature variation when it is attached to the absorber. However, it is concluded from Figure 3.12 (b) that the lens-horn provides a focus.

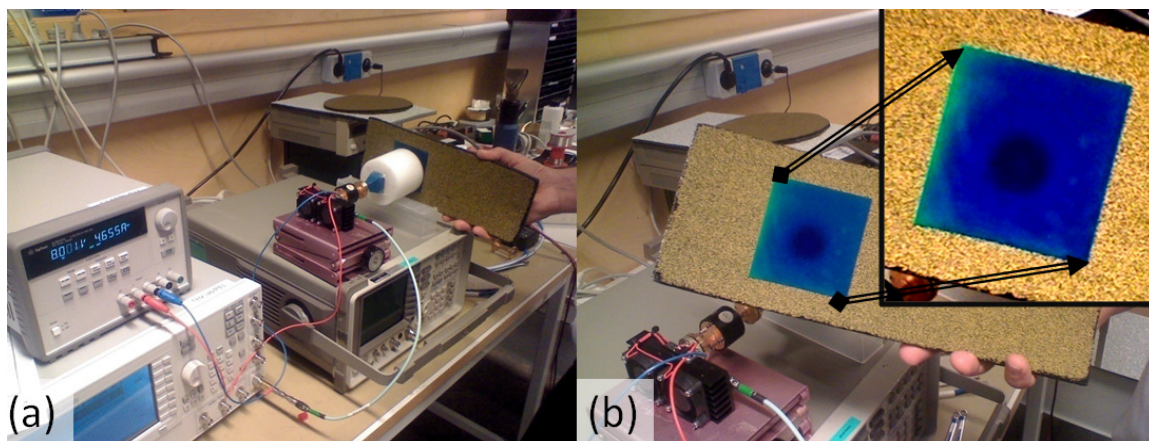


Figure 3.12: (a) An alternative for determining the focusing of a catadioptric lens at 40 GHz using liquid crystal Mylar sheet ($20^{\circ}\text{C} - 25^{\circ}\text{C}$). (b) Shows the focus.

Chapter 4. Imaging Applications

4.1 Introduction

The electromagnetic (EM) spectrum is the range of all possible frequencies of EM radiation. The EM spectrum of an object is the characteristic distribution of EM radiation emitted or absorbed by that particular object. The spectrum, shown in Figure 4.1, extends from low RF through to gamma radiation at the short-wavelength end. Different regimes of the EM spectrum have been utilised and coined, e.g., RF, MW, THz, FIR, IR, visible, UV, X-rays and Gamma-rays.

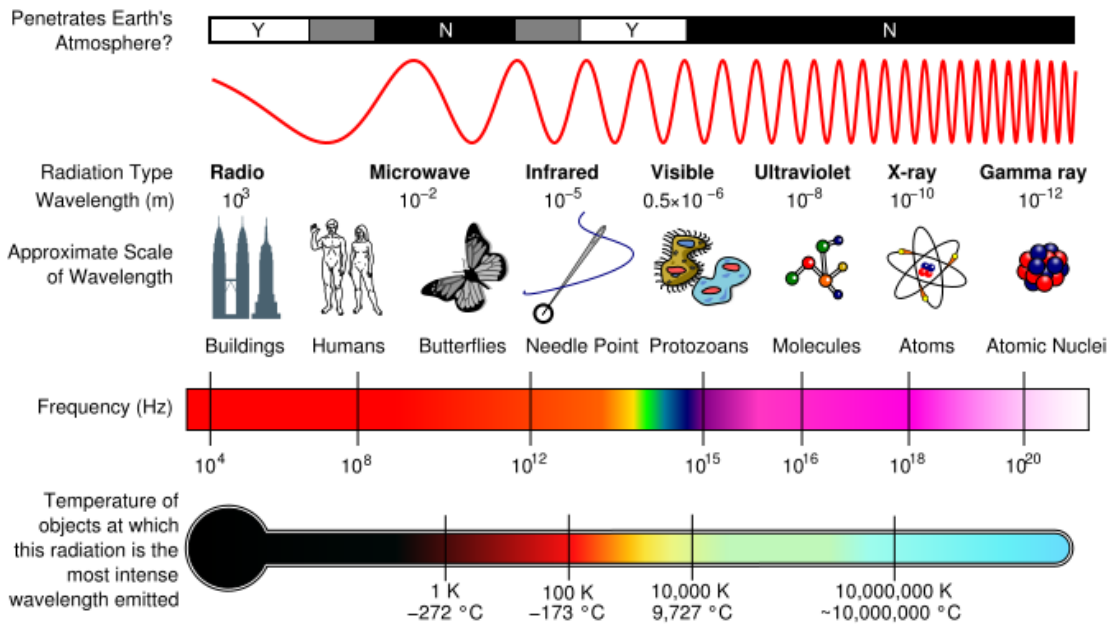


Figure 4.1: The electromagnetic spectrum [101].

However, we humans can see only a fraction of the spectrum. The visible spectrum, starting from red to violet, enables us to see the colours and provides the perception of vision. In contrast to our visible spectrum, there is plethora of information in the other frequency bands.

Wilhelm Röntgen wrote an initial report "On a new kind of ray: A preliminary communication" and on December 28, 1895 submitted it to the Würzburg's Physical-Medical Society journal. This was the first paper written on X-rays. Röntgen referred to the radiation as "X", to indicate that it was an unknown type of radiation. Till date, X-ray is one of the most dominant candidates for imaging. However, due to detrimental effects of X-ray, other techniques are becoming more popular these days.

The first mmw and submmw activity occurred in the 1890's [2] followed by numerous discoveries and inventions by Hertz, Lebedew, Lampa and J. C. Bose and others. Wiltse, in [2], made a nice attempt to identify many of the major events that have occurred in the development of mmw and submmw technology. The THz spectrum is an overlap between mmw and submmw frequencies and spans from 0.1 THz – 10 THz. THz regime combines the benefits of MW and IR regimes by offering low scattering and high lateral resolution. THz systems are able to 'see through' concealing barriers such as packaging, clothing, shoes, baggage, etc in order to probe the potentially dangerous materials contained within. THz radiation is non-ionizing and the power levels used do not cause any detrimental effects. In recent years, various applications have been developed in the THz frequencies. THz applications include imaging, spectroscopy, nondestructive testing, stand-off detection of concealed weapons, explosives and narcotics [6, 7], automobile radar systems [8] and biomedical applications [9, 10]. THz near field microscopy has shown the possibility to achieve micrometer resolution [102]. Real-time THz images have been obtained [103]. An all-optoelectronic imaging system has been reported with promising results [104]. Stand-off security screening has shown attractive results [6, 105, 106]. As reviewed by Tonouchi [5], the expected roadmap for THz applications includes indoor and outdoor communications, security screening, drug detection, biometrics, food, agriculture, medicine, DNA, medical, semiconductor wafer inspection, semiconductor LSI integration, and air pollution.

4.2 Imaging systems

THz imaging systems are mainly based on near-field and far-field imaging, passive radiometry, active direct detection, heterodyning. The techniques may involve scene-illumination. These different techniques for THz imaging also incorporate various components and sources. Operating temperature is of much importance and therefore state-of-the-art research trend is more focused on room temperature components. A brief overview has been presented in Figure 4.2 showing THz system modalities with examples of various systems. The THz system modalities include passive direct detection [107], active direct detection system [108], passive radiometric system [109], time-gated system [110] and active heterodyne system [105, 106]. Those systems can be single-pixel or multi-pixel and may incorporate mechanical movements and quasioptical components. However, high sensitivity can be achieved using active heterodyne systems.

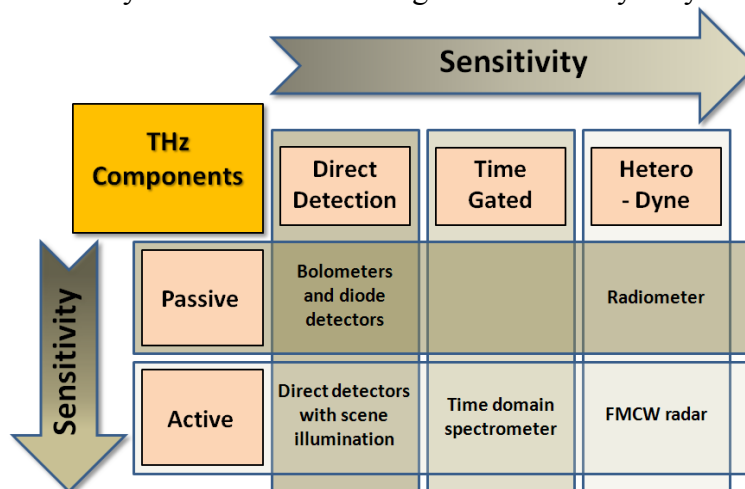


Figure 4.2: THz system modalities incorporating various components and techniques.

Terahertz time-domain spectroscopy (TDS) is one of the most popular techniques in which sub-picosecond pulses, typically generated by a femtosecond laser, are used to generate broadband terahertz radiation. The broad bandwidth of the THz radiation is advantageous in a reflection mode as it permits to obtain depth information and therefore construct a full 3D representation of an object. The first demonstration of 3D THz imaging, based on time-of-flight, was described in 1997 [110]. Contrary to time domain systems, CW imaging systems are usually compact, simple, fast, and of relatively low-cost. The TDS is inherently broadband therefore sources are of low power. CW sources provide much higher power and therefore higher dynamic range is easier to obtain. Unlike pulsed THz imaging, the CW imaging provides only intensity data and does not provide any depth, frequency-domain or time-domain information about the subject when a fixed frequency source and a single detector are used [111]. Active THz imager, utilising the swept-frequency FMCW radar technique, can be used to map a target in three dimensions [105, 106].

The above-mentioned systems are mainly farfield systems. For farfield imaging systems, the well-known Abbe limit sets the ultimate spatial resolution to $\sim \lambda/2$ [77]. The maximum resolution of these systems is limited by the apertures and the distance and generally it is not possible to resolve objects less than few wavelengths [76].

In contrast to farfield imaging systems, nearfield imaging systems can resolve features much smaller than a wavelength [112]. However, these systems are complex and require more stringent setups. In those systems, the position of the nearfield probe is a determining factor and planar surfaces are only realistic to image. Therefore, the practical deployment in general applications of those systems is limited.

In recent years, compact and integrated sources and receivers at THz frequencies are being developed. One of the driving forces behind developing those compact and integrated components is short-range THz imaging [113-115]. Short-range THz imaging applications are less power demanding due to low propagation or scattering losses. Moreover, precautions related to ambient noise and disturbances are greatly reduced.

However, practically feasible short-range imaging applications require compact, robust and easily deployable setup. Therefore the use of conventional quasioptical components, e.g. focusing mirrors, is inconvenient.

4.3 A short-range imaging system

As discussed before, the catadioptric lens provides an attractive solution as a focusing element. Therefore practically feasible short-range imaging systems will benefit from it. With a view to utilise the focusing property of the catadioptric lens and thereby to realise a short-range imaging system, a 3-axis automated stage was constructed with 40 cm travel length in each axis. The stage can provide micrometer precision (maximum resolution = 2.5 μm) with reasonable payload. The setup is completely automated and can be controlled by a computer. Figure 4.3 (a) shows the 3-axis stage.

The focusing property and the intensity profiles of the catadioptric lens, fed by a WR-10 standard gain conical horn, were studied at 108 GHz due to available sources. The

imaging examples that are presented in this chapter are obtained by CW short-range imaging at 108 GHz using the lens-horn configuration. The lens-horn configuration has been shown in the inset of Figure 4.3 (a). The imaging setup is shown in Figure 4.3 (b). A computer was used to readout the measured data from PM2 via a Keithley 2000 multimeter.

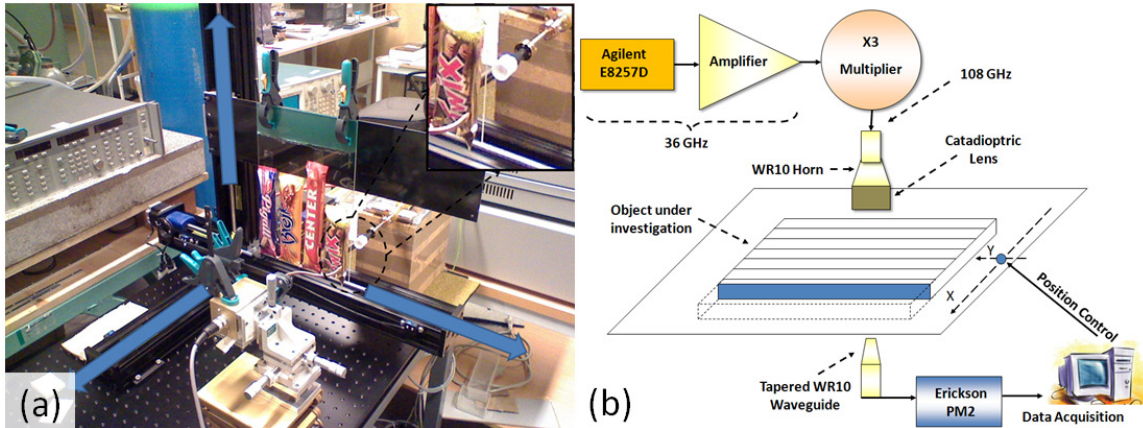


Figure 4.3: (a) The constructed 3-axis stage, and (b) the short-range THz imaging setup, working at 108 GHz.

4.4 Imaging system characterisation

Spatial resolution is a property that describes the ability of an imaging system to accurately depict objects in the two spatial dimensions. The classic notion of spatial resolution is the ability of an imaging system to distinctly depict two objects as they become closer to each other. At some point, the two objects become so close that they appear as one and at this point spatial resolution is lost. One conceptual way of understanding and measuring the spatial resolution of an imaging system in the spatial domain is to stimulate the system with a single point source and then observe its response. The image produced from a single point stimulus is called a point response function or a point spread function (PSF). PSF is the irradiance distribution that results from a single point source in object space. The degree of spreading (blurring) of the point object is a measure for the quality of an imaging system. The Fourier transform of PSF is called the optical transfer function (OTF) while modulation transfer function (MTF) is the magnitude of the complex-valued OTF.

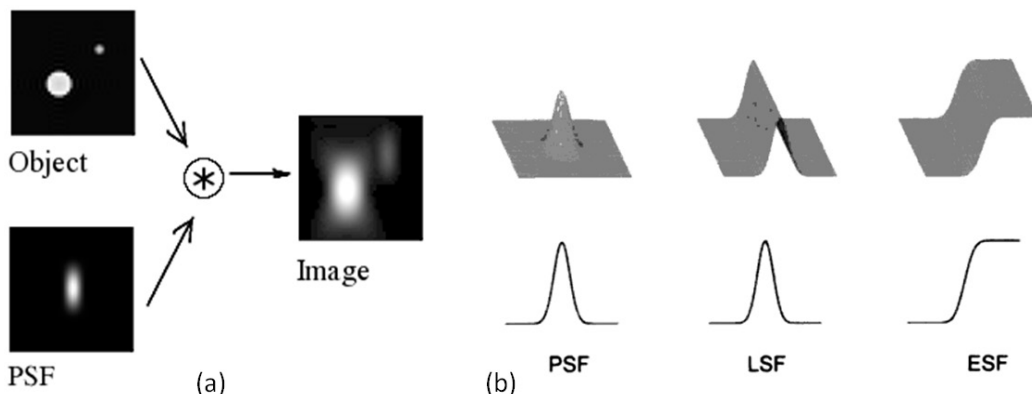


Figure 4.4: (a) Image formation in an optical system where the image is a convolution of the actual object and the PSF [116]. (b) PSF, LSF and ESF [117].

PSF plays an important role in the image formation theory of an imaging system. It is the main brick that builds up the whole acquired image. As shown in Figure 4.4(a), the image of an object is the convolution of the actual object and the PSF of the imaging system. Therefore, the image can be deconvolved in order to obtain the actual object if the PSF is known. The line spread function (LSF) describes the response of an imaging system to a linear stimulus. To determine the LSF, a slit image is acquired. The LSF can be thought of as a linear collection of a large number of PSFs. The edge spread function (ESF) a system is the image of an ideal step function. For instance, the edge of a completely opaque seminfinite screen can be used as the step function. LSF can be calculated by differentiating the ESF.

Direct measurement of the PSF is, however, uncommon because of the low signal levels available for measurement when the radiant flux is limited at the input by a pinhole. The standard method of calculating the PSF is to measure LSF or ESF. Determining ESF is more practical and more convenient than LSF and PSF. A knife-edge target is simpler to construct than a narrow slit and a small spot. Moreover, the knife-edge method can be used with lower radiance source as the measurements of LSF and PSF may suffer from poor *SNR*.

The imaging system, shown in Figure 4.3 (b), was characterised and results are presented in Paper B. In order to determine the focal diameter and the ESF of the lens-horn, the edge of an aluminium screen was moved across the focus ($Z = 12$ mm). Figure 4.5 (a) shows the ESF. LSF was derived from the ESF, normalised, fitted to Gaussian distribution and standard deviation (σ) = 0.4λ was obtained. Assuming rotational symmetry, PSF was constructed from the LSF. Figure 4.5 (b) shows the PSF. In order to study the resolution, a metallic pattern was made having holes ranging from 1 mm to 3 mm with 0.25 mm steps. The holes are spaced at 5 mm from each other. Figure 4.6 (a) shows the photograph of the metallic pattern. The pattern was imaged at 108 GHz using the setup illustrated in Figure 4.3 (b).

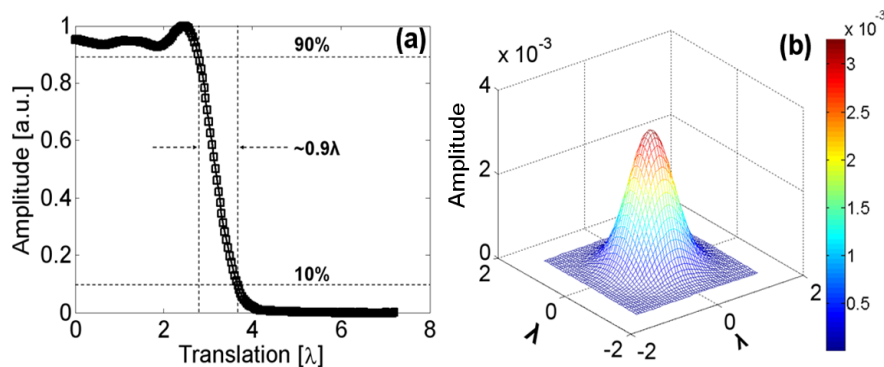


Figure 4.5: (a) Edge spread function (ESF), and (b) point spread function (PSF).

Figure 4.6 (b) shows the image of the pattern when only the horn was used as the transmitter while Figure 4.6 (c) shows the image for lens-coupled horn transmitter. The images are of 121×121 pixels and represent the contrast in dB. The contrast is defined as $(I - I_{min}) / (I_{max} + I_{min})$ where I_{max} and I_{min} are the maximum and minimum intensities, consecutively. It can be observed from the figures that the lens-coupled system provides significantly improved and comprehensible images. Later, the image, shown in Figure

4.6 (c), was deconvolved using the obtained PSF and the resulting image is shown in Figure 4.6 (d). This deconvolved image closely resembles the optical image.

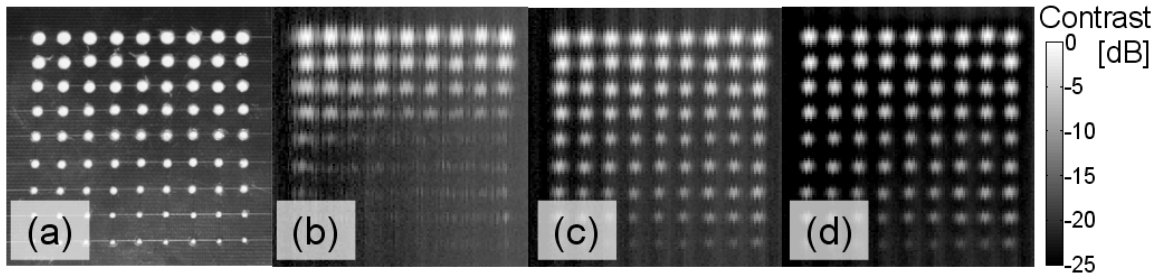


Figure 4.6: (a) Metallic pattern having holes ranging from 1 mm to 3 mm with 0.25 mm steps. Images of the metallic pattern (b) without and (c) with the lens, and (d) shows the deconvolved image of (c). The images represent the contrast in dB.

Figure 4.7 shows the contrast in dB and 3 dB-down points for a scan across the holes of different sizes of the metallic pattern, using lens-horn and only horn as transmitter. The figure indicates that due to the focusing of the lens, the *SNR* is increased making the smallest holes visible. Therefore, with the aid of the lens, features close to a wavelength are resolved, which are absent or indistinguishable otherwise.

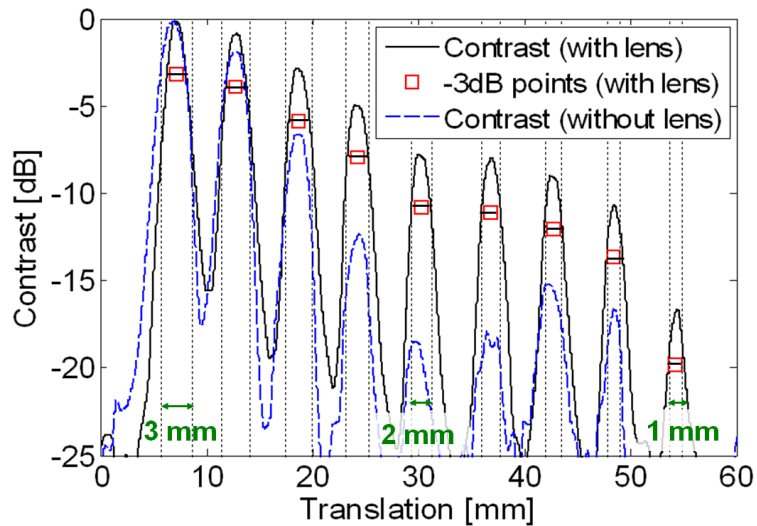


Figure 4.7: Contrast in dB for a scan across the holes of different sizes (3 mm to 1 mm with 0.25 mm steps) of the metallic pattern with and without the lens.

4.5 Application examples

The characterisation and measurement results of the catadioptric lenses, presented in Chapter 3, showed that the lens-antenna configurations are attractive for practical applications in MW and THz frequencies. In this section, several application examples are presented in both MW and THz frequencies.

4.5.1 Microwave applications

The 80 mm diameter Delrin lens was coupled to an 8.5 GHz bow-tie slot antenna. The focusing property of the lens is studied experimentally. The lens-antenna provides 60% bandwidth centred at ~ 6 GHz. At 6 GHz ($\lambda_0 \sim 50$ mm) the lens diameter D_{lens} is $\sim 1.6 \lambda_0$ or $\sim 3.1 \lambda_{\text{Delrin}}$ where λ_0 is free space wavelength and λ_{Delrin} is the wavelength in Delrin. The lens is electrically small (a few λ) and provides a compact solution for system integration. The lens-antenna configuration is attractive for applications requiring compact and wideband solution as well as focused beam.

In this section, several application examples are presented employing the catadioptric lens-antenna. 1-port measurements were performed and the obtained S_{11} parameters from 1 GHz – 10 GHz were converted into time domain by inverse Fourier transformation and the amplitude of the reflected signal was studied. Some of these results are also presented in Paper C.

Example 1: In the first example, shown in Figure 4.8 (a), reflections from two hardcover books of having thicknesses of 32 mm (Book 1) and 65 mm (Book 2) were investigated. As can be seen from the figure, reflections from front and back covers of the books are clearly distinguishable.

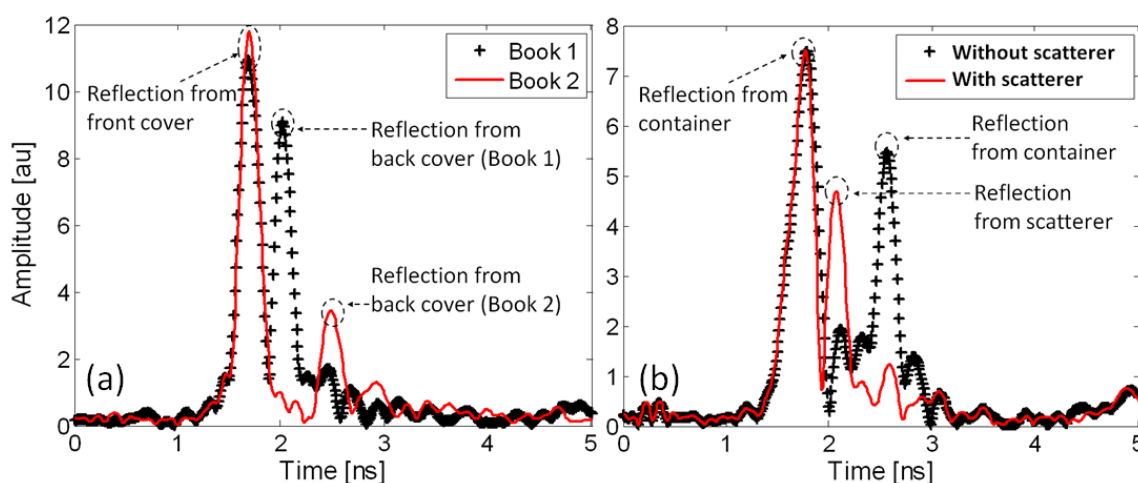


Figure 4.8: (a) Time domain reflected signal from hardcover books. (b) Time domain reflected signals from the container with and without the scatterer.

The detection of a scatterer and its location in a homogenous medium is of importance for various applications. However, the dimension of the scatterer and its dielectric contrast pose a practical challenge for NDE systems. The lens-antenna was employed to

detect and locate a dielectric scatterer in a homogenous medium. A potato, having nearly perfect spherical shape of 30 mm diameter, was used as the dielectric scatterer. The homogenous medium was represented by a plastic container with vegetable oil and measurements were performed with and without the presence of the scatterer. Figure 4.8 (b) shows the time domain reflected signals without and with the scatterer. Reflections from front and back walls of the container are noticed when no scatterer was present. However, when the scatterer is inserted into the container, the time domain reflected signal clearly shows its presence. Due to the focusing of the lens-antenna, the detection of scatterer is marked while the reflection from the back wall of the container is suppressed.

Example 2: The catadioptric lens-antenna was employed to scan several buried objects sandwiched by 30 mm thick Styrofoam. The dimensions of the buried objects and the spacing between them were ~ 20 mm. Figure 4.9 shows the amplitude of the reflected signal for a line scan along the sandwiched samples. The amplitude of the reflection is highest for the metal coin and lowest for the plastic object. Although the objects are spatially densely located, the focused beam of the lens-antenna reveals the buried objects successfully.

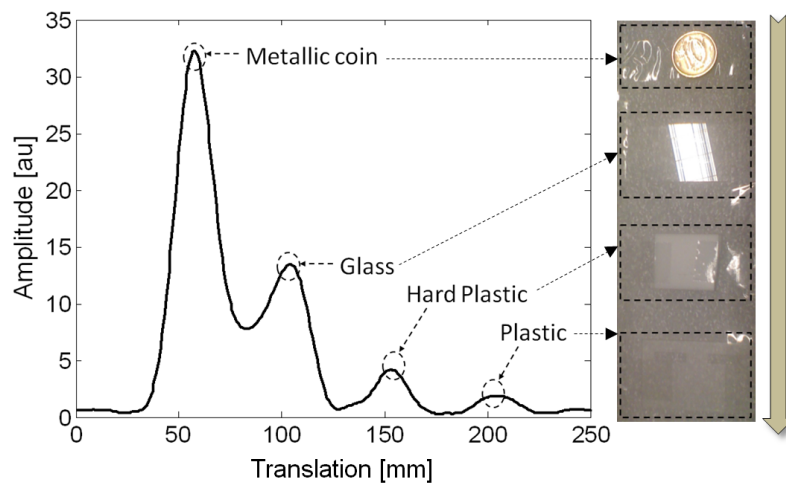


Figure 4.9: Reflected signal for a line scan of 4 different buried objects in Styrofoam.

4.5.2 Terahertz applications

Characterisation of a catadioptric dielectric lens-horn configuration has been presented in Chapter 3. The focusing property was investigated both numerically and experimentally at 108 GHz. The lens-horn provides a focal spot of $\sim 0.9\lambda$ at a distance of $\sim 4.5\lambda$. A test pattern was imaged and a marked improvement in image resolution was observed. With the aid of the lens, features close to the wavelength are resolved, which are absent or indistinguishable otherwise. In this section, several imaging examples, utilising the focusing ability of the lens are presented. The setup, illustrated in Figure 4.3 (b), was used for all the imaging examples. During the imaging procedures, different types of objects were chosen in order to explore the application areas for THz imaging.

Example 1: A chocolate bar, shown in Figure 4.10 (a), was imaged. The chocolate bar was particularly interesting as it contained randomly placed blobs of different type of chocolates. The dimensions of the blobs were several millimetres. However, the THz image, shown in Figure 4.10 (b), does not reveal the blobs probably due to the similar dielectric properties of the blobs and the rest of the chocolate. However, the elevation patterns of the chocolate bar and a notch are clearly visible as shown Figure 4.10.

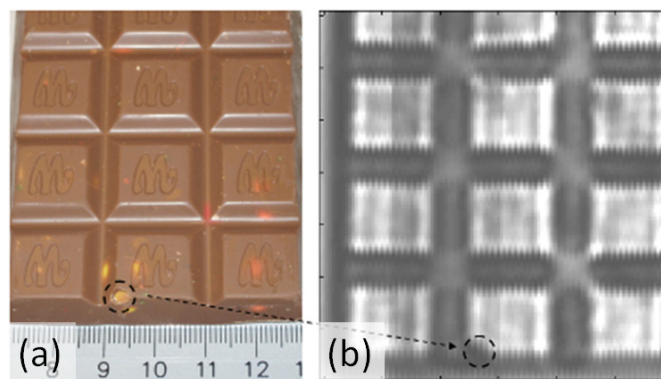


Figure 4.10: (a) Photograph of a chocolate bar, and (b) its THz image.

A number of commercially available chocolate products were imaged. Figure 4.11 (a) shows the used samples. In contrast to the previous investigation, the chocolate samples were imaged with their wrappers. Therefore, the composition and the shape of the chocolates were essentially unknown. Figure 4.11 (b) shows the THz image of the samples. The overall shapes with minute details of the first three samples have been revealed in the THz image. However, no information of the fourth sample was revealed due to the aluminium content in the wrapper.

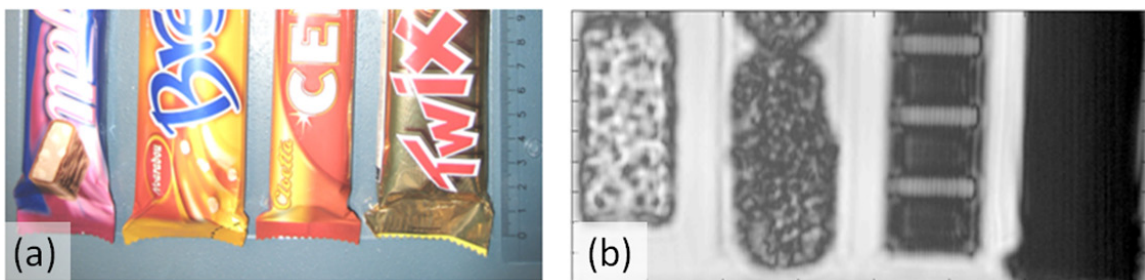


Figure 4.11: (a) Photograph of the chocolate samples, and (b) their THz image.

Example 2: The example presented here signifies the use of THz imaging for nondestructive evaluation. The object, shown in Figure 4.12 (a), is solid and visually homogenous. Therefore, non-invasive visual inspection of the inner structure is not possible. The THz image, shown in Figure 4.12 (b), reveals the actual structure and indicates that the object is partially filled with metal.

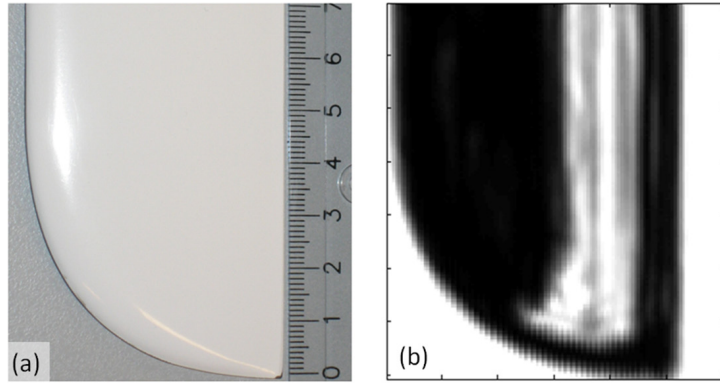


Figure 4.12: (a) Photograph of a solid and visually homogenous object (rotor blade of an R/C helicopter), and its (b) THz image, revealing the actual structure.

Example 3: The current example shows an imaging example of conventionally used RFID tags, shown in Figure 4.13 (a) and Figure 4.13 (c). The first tag, used in public transports, contains a microchip and an antenna. The THz image, shown in Figure 4.13 (b), reveals the microchip. The interconnections and the antenna are partially obscure due their subwavelength dimensions at the imaging frequency.

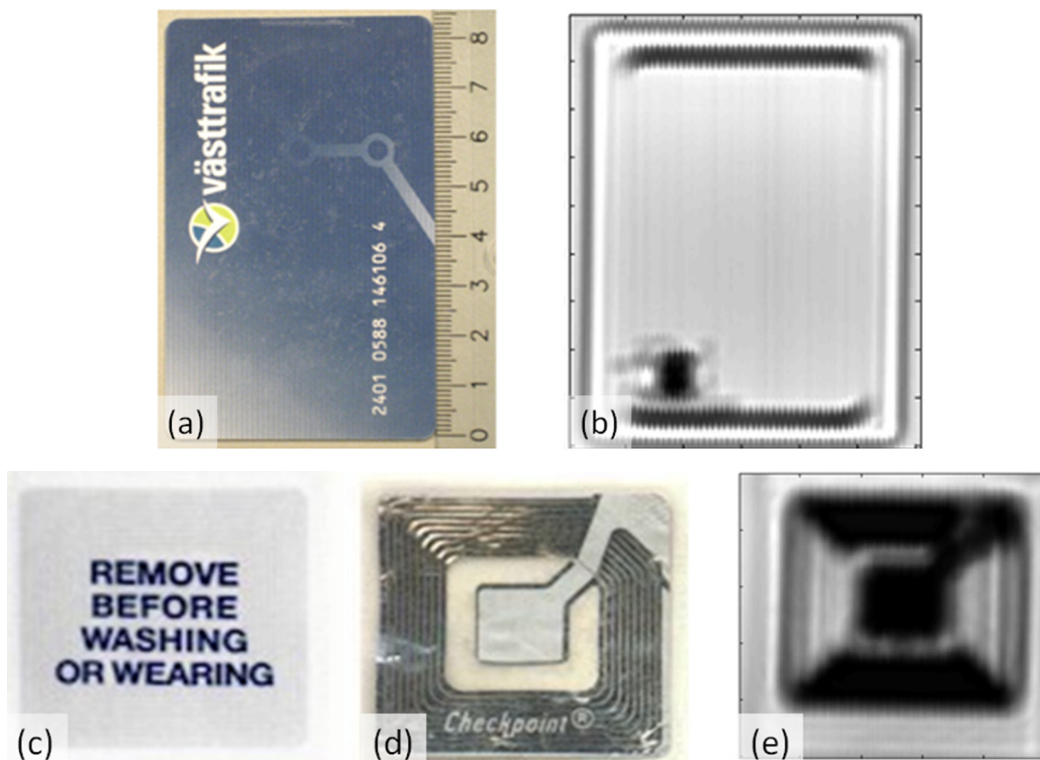


Figure 4.13: (a) A RFID tag, used in public transports, and (b) its THz image. (c) A conventionally used RFID tag (anti-theft device), and its (d) internal view. (e) THz image of the RFID tag.

In addition to performing a nondestructive evaluation, the second tag was particularly interesting as it contains a rectangular spiral antenna, shown in Figure 4.13 (c-d). The antenna can be thought as a rectangular array of parallel metallic wires. Therefore, the antenna acts as a wire-grid polariser. In the imaging setup, the radiated THz beam was linearly polarised. The THz image of the RFID tag, shown in Figure 4.13 (e), illustrates that the radiated THz beam was horizontally polarised. The example also illustrates a particularly challenging scenario for a linearly polarised beam when it is used for imaging an object having repetitive features smaller than the wavelength.

Example 4: The imaging setup was used to image partially dead leaves. Different parts of the leaf, e.g. veins, introduce different amounts of transmission losses which correspond to their water content. Figure 4.14 (a) shows the photograph of the first sample where the dark colours correspond to the “living” parts and therefore indicates more water content. Figure 4.14 (b) shows part of the leaf (6 cm × 6 cm), which was imaged while Figure 4.14 (c) shows the THz image. The second sample, shown in Figure 4.14 (d), had several parched regions. Figure 4.14 (e) shows the THz image of the second sample. Compared to the photographs, shown in Figure 4.14 (b) and Figure 4.14 (d), the leaf veins, watery and parched regions of the leaves are clearly distinguishable in Figure 4.14 (c) and Figure 4.14 (e).

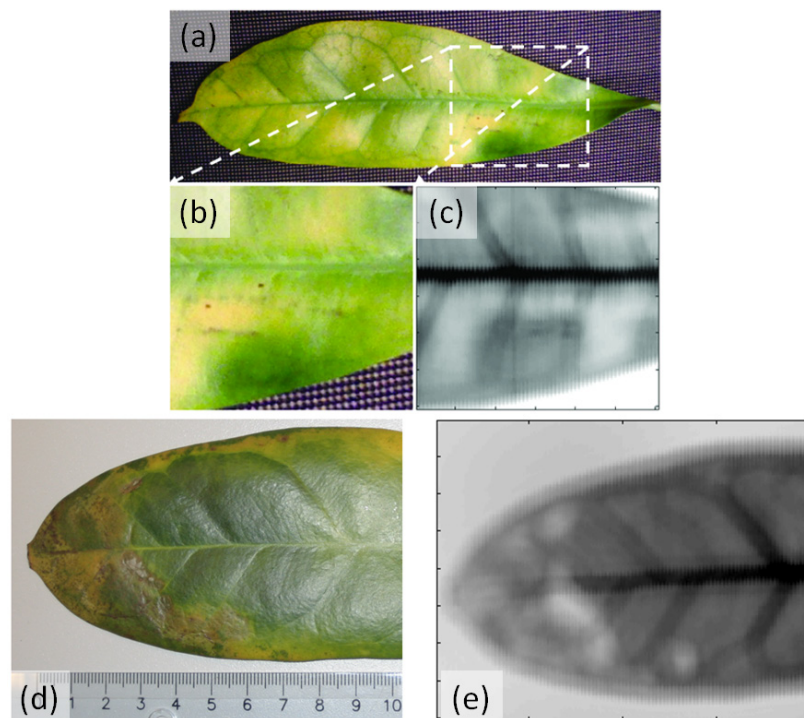


Figure 4.14: (a) Photograph of a partially dead leaf (b) part of the leaf and (c) its THz image. (d) Photograph of the second leaf sample, and (e) its THz image.

Example 5: The dielectric properties of different biological tissues are different [118, 119]. In order to explore the possibilities, a THz imaging was performed on commercially available bacon slices, shown in Figure 4.15 (a). The bacon slices are particularly interesting because of the presence of both regular and fat tissues. The dielectric properties of fat tissues are different than other types of tissues. The bacon slices were wrapped with very thin plastic film, commercially known as Saran Wrap

(polyvinylidene chloride) or cling film, in order to avoid water loss in the form of evaporation. Thus, constant water content was assured throughout the measurement. The plastic film was $\sim 10 \mu\text{m}$ thick and is used mainly for food packaging. The THz transmittance of a single layer of this film is above 98% [120], including the reflection losses, which makes it an ideal material for sample support. The THz image of the bacon samples reveals high contrast between the fat tissues and others, as shown in Figure 4.15 (a). Furthermore, minute details are also visible in the image.

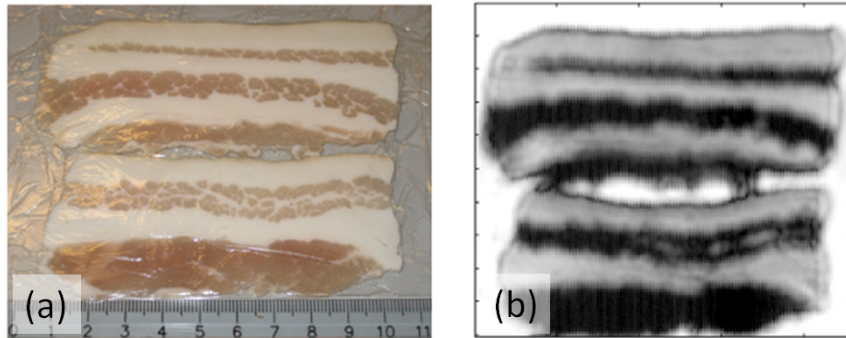


Figure 4.15: (a) Photograph of the bacon slices, and (b) their THz image.

Chapter 5. Conclusion and Future Directions

Research summary

THz technology, considering its tremendous potential, is expected to establish a pronounced presence in communication, imaging and security systems. In order to utilise the THz technology to the fullest extent, the need of viable wave generation and detection components and systems has been dominating the research-focus. Room temperature, compact, low cost and tunable THz sources, detectors, waveguiding, and beam steering elements will play a vital role in realising the THz systems. Moreover, compact THz systems are required for practical applications.

UTC-PDs, as discussed so far, are extremely promising for THz generation and can be integrated in suitable systems for any specific application. UTC-PDs provide wide tunability and decent amounts of output power at room temperature. In this thesis, a number of issues have been addressed as a part of an optimisation procedure for improving the performance of the UTC-PD. An example of the UTC-PD epitaxial layer optimisation has been shown. Furthermore, several UTC-PD integrated antennas have been presented. However, possible design issues related to the UTC-PD optical injection and array fabrication need to be addressed. Further studies are required regarding intermodulation distortion (IMD) and noise in UTC-PDs.

Imaging systems, nondestructive evaluation systems etc. employ focusing components in order to attain a high resolution. The catadioptric dielectric lens, presented in this thesis, provides an attractive and simple solution as a focusing element. The lens and its focal length are electrically small. Radiating elements and sensors can be physically coupled to the lens in order to achieve short-range focusing ability, therefore, enabling a compact system. However, further investigation is necessary to identify potential engineering materials for the lens and to optimise the lens geometry.

Several application examples were presented at microwave and terahertz frequencies employing the catadioptric lenses. A short-range THz imaging system has been described. The results and images have shown that the imaging system, with the aid of the catadioptric lens, is a promising and attractive solution to realise compact and practically feasible systems.

The results and perspectives, presented in this thesis, are expected to assist the quest for compact THz systems. A prudent vision to construct a compact THz imaging system would be to incorporate UTC-PDs with the catadioptric lens. UTC-PD based photomixers can be integrated with antennas and can even be used in the array configuration. The catadioptric lens provides focusing capability. Therefore the integrated solution, incorporating UTC-PD based sources and the catadioptric lens, can be effectively used in imaging systems.

Future directions

Fostering THz applications and assuring its benefits to reach masses require a stagnant issue to be resolved: the absence of compact, tunable, inexpensive and room temperature THz sources with relatively high output power. From practical point of view, the THz CW sources are highly sought after for applications such as high resolution THz spectroscopy, imaging and ultra-broadband communications. Therefore, the need of room temperature THz CW sources is becoming more pronounced with considerable emphasis on tunability.

A number of methods can be used to generate THz radiation of different wavelength ranges, either pulsed or CW with varying degrees of success. Although being the precursors of THz technology, most of the existing sources can be ruled out due to their operating temperature, bulkiness and price tag. In fact, only few viable room temperature solutions exist for THz generation. Even though there are encouraging perspectives regarding the photonic THz generation at room temperature, the low output power or the accompanying instruments (e.g. laser sources) curtain this photonic technique from general application environments. A paradigm shift is necessary in order to explore realistic and practical THz systems based on photonic generation. Researchers are working on photomixers with integrated excitation schemes using technologies such as VCSEL [121]. It is, however, not clear when this approach will be materialised and matured for practical THz applications. Other types of broadband THz generation schemes are yet to depart the laboratory environment for general applications [14].

The state-of-the-art trends in THz research accentuate electronic devices such as resonant tunnelling diodes, Gunn diodes, Impatt diodes, graphene devices, Schottky diodes and HBV multipliers etc. More recently, CMOS THz electronics has joined the race [122]. However, carrier transit times or parasitic RC -time constants still prevail. Nevertheless, CW systems are in a favourable position being nurtured by these technologies. Compact and room temperature THz sources and front-ends are now more realistic to visualise. Therefore, it is justifiable to presume that THz application areas will be acquired by CW systems.

An example scenario can be resorted to understand the need of viable components at THz frequencies. At present, stand-off imaging techniques are being extensively explored for security concerns. Active THz imagers with heterodyne detection are preferred for high sensitivity and high speed. Moreover, stand-off THz applications are particularly challenging due to atmospheric losses and therefore atmospheric windows in the THz regime must be used. This example scenario suggests CW THz sources. However, the major limitation of general CW systems is the lack of depth and phase information, unlike time domain systems. One way to overcome this limitation is to utilise the swept-frequency FMCW radar technique and thereby mapping a target in three dimensions. Consequently, the CW sources need to be tunable to achieve frequency modulation. The all-embracing perspective of this example scenario is the need of compact, tunable, and room temperature THz sources.

As a conclusion, the quest for compact, tunable, and room temperature THz sources and systems will continue.

Epilogue

Sustainability is a term which, nowadays, has lost its pace with the technological advancements. Once valves were thought to be a sustainable technology for computers but now almost disappeared. One of the main determinant factors for sustainability is cost. Prudent research and the following mass manufacturing have stretched out the mmw radar technology in civilian automobiles. The numerous technological breakthroughs in THz research areas will probably continue but many will phase out with time. However, some technologies will certainly make THz applications more accessible and affordable for common people.

At present, it is not evident which technologies will sustain to cultivate the THz regime. It is also probably unimportant for researchers to determine sustainability. It is, however, important that the greater humanity is benefited from all technological advancements, including the ones from the fascinating THz regime.

References

- [1] P. H. Siegel, "Terahertz technology," *IEEE Transactions on Microwave Theory and Techniques*, vol. 50, pp. 910-928, 2002.
- [2] J. C. Wiltse, "History of Millimeter and Submillimeter Waves," *IEEE Transactions on Microwave Theory and Techniques*, vol. 32, pp. 1118-1127, 1984.
- [3] T. G. Phillips and J. Keene, "Submillimeter Astronomy," *Proceedings of the IEEE*, vol. 80, pp. 1662-1678, Nov 1992.
- [4] L. Ho, R. Muller, M. Romer, K. C. Gordon, J. Heinamaki, P. Kleinebudde, M. Pepper, T. Rades, Y. C. Shen, C. J. Strachan, P. F. Taday, and J. A. Zeitler, "Analysis of sustained-release tablet film coats using terahertz pulsed imaging," *Journal of Controlled Release*, vol. 119, pp. 253-261, 2007.
- [5] M. Tonouchi, "Cutting-edge terahertz technology," *Nat Photon*, vol. 1, pp. 97-105, 2007.
- [6] R. Appleby and H. B. Wallace, "Standoff detection of weapons and contraband in the 100 GHz to 1 THz region," *IEEE Transactions on Antennas and Propagation*, vol. 55, pp. 2944-2956, Nov 2007.
- [7] R. J. Dengler, K. B. Cooper, G. Chattopadhyay, I. Mehdi, E. Schlecht, A. Skalare, C. Chen, and P. H. Siegel, "600 GHz Imaging radar with 2 cm range resolution," *IEEE/MTT-S International Microwave Symposium Digest, Vols 1-6*, pp. 1367-1370, 2007.
- [8] I. Gresham, A. Jenkins, R. Egri, C. Eswarappa, N. Kinayman, N. Jain, R. Anderson, F. Kolak, R. Wohlert, S. P. Bawell, J. Bennett, and J. P. Lanteri, "Ultra-wideband radar sensors for short-range vehicular applications," *IEEE Transactions on Microwave Theory and Techniques*, vol. 52, pp. 2105-2122, Sep 2004.
- [9] P. H. Siegel, "Terahertz technology in biology and medicine," *IEEE Transactions on Microwave Theory and Techniques*, vol. 52, pp. 2438-2447, 2004.
- [10] T. W. Crowe, T. Globus, D. L. Woolard, and J. L. Hesler, "Terahertz sources and detectors and their application to biological sensing," *Philosophical Transactions of the Royal Society of London Series a-Mathematical Physical and Engineering Sciences*, vol. 362, pp. 365-374, Feb 15 2004.
- [11] R. J. Trew, "High-frequency solid-state electronic devices," *IEEE Transactions on Electron Devices*, vol. 52, pp. 638-649, 2005.
- [12] G. I. Haddad and R. J. Trew, "Microwave solid-state active devices," *IEEE Transactions on Microwave Theory and Techniques*, vol. 50, pp. 760-79, 2002.
- [13] C. Walther, M. Fischer, G. Scalari, R. Terazzi, N. Hoyler, and J. Faist, "Quantum cascade lasers operating from 1.2 to 1.6 THz," *Applied Physics Letters*, vol. 91, pp. -, Sep 24 2007.
- [14] D. Dragoman and M. Dragoman, "Terahertz fields and applications," *Progress in Quantum Electronics*, vol. 28, pp. 1-66, 2004.
- [15] P. Penfield and R. P. Rafuse, *Varactor Applications*. Cambridge: M.I.T. Press, 1962.

- [16] M. Lee and M. C. Wanke, "Searching for a Solid-State Terahertz Technology," *Science*, vol. 316, pp. 64-65, 6 April 2007.
- [17] P. R. Smith, D. H. Auston, and M. C. Nuss, "Subpicosecond Photoconducting Dipole Antennas," *IEEE Journal of Quantum Electronics*, vol. 24, pp. 255-260, Feb 1988.
- [18] C. M. Penchina, "Theory of optical beating in photoconductors (phenomenological modification of semiclassical treatment)," *Physical Review*, vol. 136, pp. 911-917, 1964.
- [19] A. T. Forrester, W. E. Parkins, and E. Gerjuoy, "On the Possibility of Observing Beat Frequencies between Lines in the Visible Spectrum," *Physical Review*, vol. 72, pp. 728-728, 1947.
- [20] T. Ishibashi, N. Shimizu, S. Kodama, H. Ito, T. Nagatsuma, and T. Furuta, "Uni-traveling-carrier photodiodes," Incline Village, NV, USA, 1997, pp. 83-7.
- [21] H. Ito, T. Nagatsuma, A. Hirata, T. Minotani, A. Sasaki, Y. Hirota, and T. Ishibashi, "High-power photonic millimetre wave generation at 100 GHz using matching-circuit-integrated uni-travelling-carrier photodiodes," *Optoelectronics, IEE Proceedings -*, vol. 150, pp. 138-142, 2003.
- [22] C. C. Renaud, M. Robertson, D. Rogers, R. Firth, P. J. Cannard, R. Moore, and A. J. Seeds, "A high responsivity, broadband waveguide uni-travelling carrier photodiode," Strasbourg, France, 2006, p. 61940.
- [23] E. R. Brown, F. W. Smith, and K. A. McIntosh, "Coherent Millimeter-Wave Generation by Heterodyne Conversion in Low-Temperature-Grown GaAs Photoconductors," *Journal of Applied Physics*, vol. 73, pp. 1480-1484, Feb 1 1993.
- [24] D. M. Mittleman, R. H. Jacobsen, and M. C. Nuss, "T-ray imaging," *IEEE Journal of Selected Topics in Quantum Electronics*, vol. 2, pp. 679-692, Sep 1996.
- [25] A. Hirata, M. Harada, and T. Nagatsuma, "120-GHz wireless link using photonic techniques for generation, modulation, and emission of millimeter-wave signals," *Journal of Lightwave Technology*, vol. 21, pp. 2145-53, 2003.
- [26] V. Krozer, B. Leone, H. G. Roskos, T. Löffler, G. Loata, G. H. Döhler, F. Renner, S. Eckardt, S. Malzer, A. SchwanhauBer, T. O. Klaassen, A. Adam, P. Lugli, A. Di Carlo, M. Manenti, G. Scamarcio, M. S. Vitiello, and M. Feiginov, "Optical far-IR wave generation - state-of-the-art and advanced device structures," Strasbourg, France, 2004, pp. 178-92.
- [27] *Web Page*, http://science.nasa.gov/newhome/headlines/msad05feb98_1.htm.
- [28] ALMA, www.alma.nrao.edu.
- [29] H. Inaba and A. E. Siegman, "Microwave photomixing of optical maser outputs with a pin-junction photodiode," *Proceedings of the Institute of Radio Engineers*, vol. 50, pp. 1823-1824, 1962.
- [30] S. M. Duffy, S. Verghese, K. A. McIntosh, A. Jackson, A. C. Gossard, and S. Matsuura, "Accurate modeling of dual dipole and slot elements used with photomixers for coherent terahertz output power," *IEEE Transactions on Microwave Theory and Techniques*, vol. 49, pp. 1032-1038, Jun 2001.
- [31] K. A. McIntosh, E. R. Brown, K. B. Nichols, O. B. McMahon, W. F. Dinatale, and T. M. Lyszczarz, "Terahertz photomixing with diode lasers in low-temperature-grown GaAs," *Applied Physics Letters*, vol. 67, pp. 3844-6, 1995.

-
- [32] R. K. Lai, J.-R. Hwang, T. B. Norris, and J. F. Whitaker, "A photoconductive, miniature terahertz source," *Applied Physics Letters*, vol. 72, pp. 3100-3102, 1998.
- [33] V. Krozer, B. Leone, H. Roskos, T. Löffler, G. Loata, G. Dohler, F. Renner, S. Eckardt, S. Malzer, A. Schwanhüsser, T. O. Klaassen, A. Adam, P. Lugli, A. Di Carlo, M. Manenti, G. Scamarcio, M. S. Vitiello, and M. Feiginov, "Optical far-IR wave generation - State-of-the-art and advanced device structures," Strasbourg, France, 2004, pp. 178-192.
- [34] L. K. Anderson, "Measurement of the microwave modulation frequency response of junction photodiodes," *Proceedings of the IEEE*, vol. 51, pp. 846-847, 1963.
- [35] P. D. Coleman, R. C. Eden, and J. N. Weaver, "Mixing and detection of coherent light in bulk photoconductor," *IEEE Transactions on Electron Devices*, vol. ED-11, pp. 488-497, 1964.
- [36] J. M. Didomenico and O. Svelto, "Solid-state photodetection -- Comparison between photodiodes and photoconductors," *IEEE Proceedings*, vol. 52, pp. 136-144, 1964.
- [37] H. Ito, F. Nakajima, T. Furuta, and T. Ishibashi, "Continuous THz-wave generation using antenna-integrated uni-travelling-carrier photodiodes," *Semiconductor Science and Technology*, vol. 20, pp. 191-8, 2005.
- [38] S. Kodama and H. Ito, "UTC-PD-based optoelectronic components for high-frequency and high-speed applications," *IEICE Transactions on Electronics*, vol. E90-C, pp. 429-435, 2007.
- [39] T. Nagatsuma and H. Ito, "Ultrafast applications of uni-traveling-carrier photodiodes from measurement to signal processing," San Jose, CA, USA, 2003, pp. 90-104.
- [40] H. Ito, S. Kodama, Y. Muramoto, T. Furuta, T. Nagatsuma, and T. Ishibashi, "High-speed and high-output InP-InGaAs unitraveling-carrier photodiodes," *IEEE Journal of Selected Topics in Quantum Electronics*, vol. 10, pp. 709-27, 2004.
- [41] M. Gustavsson, "Fabrication and characterisation of Uni-travelling-carrier photodiodes," in *Department of Microtechnology and Nanoscience*. vol. Licentiate Thesis Göteborg: Chalmers University of Technology, 2004.
- [42] T. J. Maloney and J. Frey, "Transient and Steady-State Electron-Transport Properties of Gaas and Inp," *Journal of Applied Physics*, vol. 48, pp. 781-787, 1977.
- [43] S. M. Sze and K. K. Ng, *Physics of Semiconductor Devices*: Wiley InterScience, 2006.
- [44] *Web Page*, <http://www.ecse.rpi.edu/~schubert/Light-Emitting-Diodes-dot-org/>.
- [45] O. Madelung, *Semiconductors: Data Handbook*: Springer, 2004.
- [46] S. M. Duffy, S. Verghese, A. McIntosh, A. Jackson, A. C. Gossard, and S. Matsuura, "Accurate modeling of dual dipole and slot elements used with photomixers for coherent terahertz output power," *IEEE Transactions on Microwave Theory and Techniques*, vol. 49, pp. 1032-8, 2001.
- [47] S. Srivastava and K. P. Roenker, "Numerical modeling study of the InP/InGaAs uni-travelling carrier photodiode," *Solid-State Electronics*, vol. 48, pp. 461-70, 2004.
- [48] T. Ishibashi, T. Furuta, H. Fushimi, S. Kodama, H. Ito, T. Nagatsuma, N. Shimizu, and Y. Miyamoto, "InP/InGaAs uni-traveling-carrier photodiodes," *IEICE Transactions on Electronics*, vol. E83-C, pp. 938-49, 2000.

- [49] M. Gustavsson, P. O. Hedekvist, and P. A. Andrekson, "Uni-travelling-carrier photodiode performance with X-band modulation at high optical power," *IEEE Microwave and Wireless Components Letters*, vol. 15, pp. 297-299, May 2005.
- [50] ADS, http://eesof.tm.agilent.com/products/ads_main.html.
- [51] K. H. Yang, J. R. East, and G. I. Haddad, "Numerical Modeling of Abrupt Heterojunctions Using a Thermionic-Field Emission Boundary-Condition," *Solid-State Electronics*, vol. 36, pp. 321-330, Mar 1993.
- [52] H. Ito, T. Furuta, S. Kodama, N. Watanabe, and T. Ishibashi, "InP/InGaAs uni-travelling-carrier photodiode with 220 GHz bandwidth," *Electronics Letters*, vol. 35, pp. 1556-1557, 1999.
- [53] T. Grasser, T. Ting-Wei, H. Kosina, and S. Selberherr, "A review of hydrodynamic and energy-transport models for semiconductor device simulation," *Proceedings of the IEEE*, vol. 91, pp. 251-274, 2003.
- [54] Y. Apanovich, E. Lyumkis, B. Polsky, A. Shur, and P. Blakey, "Steady-state and transient analysis of submicron devices using energy balance and simplified hydrodynamic models," *Computer-Aided Design of Integrated Circuits and Systems, IEEE Transactions on*, vol. 13, pp. 702-711, 1994.
- [55] TCAD, www.synopsys.com.
- [56] S. M. M. Rahman, H. Hjelmgren, J. Vukusic, J. Stake, P. A. Andrekson, and H. Zirath, "Hydrodynamic Simulations of Unitraveling-Carrier Photodiodes," *Quantum Electronics, IEEE Journal of*, vol. 43, pp. 1088-1094, 2007.
- [57] J. M. Ruiz-Palmero, U. Hammer, and H. Jackel, "A physical hydrodynamic 2D model for simulation and scaling of InP/InGaAs(P) DHBTs and circuits with limited complexity," *Solid-State Electronics*, vol. 50, pp. 1595-1611, Sep-Oct 2006.
- [58] B. Banik, J. Vukusic, H. Hjelmgren, and J. Stake, "Optimization of the UTC-PD Epitaxy for Photomixing at 340 GHz," *International Journal of Infrared and Millimeter Waves*, vol. 29, pp. 914-923, 2008.
- [59] Sentaurus, "Device User guide."
- [60] H. Ito, T. Nagatsuma, A. Hirata, T. Minotani, A. Sasaki, Y. Hirota, and T. Ishibashi, "High-power photonic millimetre wave generation at 100 GHz using matching-circuit-integrated uni-travelling-carrier photodiodes," *IEE Proceedings On Optoelectronics*, vol. 150, pp. 138-142, 2003.
- [61] T. Furuta, H. Fushimi, T. Yasui, Y. Muramoto, H. Kamioka, H. Mawatari, H. Fukano, T. Ishibashi, and H. Ito, "Highly reliable uni-travelling-carrier photodiodes for 40 Gbit/s optical transmission systems," *Electronics Letters*, vol. 38, pp. 332-334, Mar 28 2002.
- [62] Comsol, www.comsol.com.
- [63] T. Yasui, T. Furuta, T. Ishibashi, and H. Ito, "Comparison of power dissipation tolerance of InP/InGaAs UTC-PDs and pin-PDs," *Ieice Transactions on Electronics*, vol. E86c, pp. 864-866, May 2003.
- [64] P. H. Siegel, "THz instruments for space," *IEEE Transactions on Antennas and Propagation*, vol. 55, pp. 2957-2965, Nov 2007.

-
- [65] H. Ito, T. Furuta, F. Nakajima, K. Yoshino, and T. Ishibashi, "Photonic generation of continuous THz wave using uni-traveling-carrier photodiode," *Journal of Lightwave Technology*, vol. 23, pp. 4016-21, 2005.
- [66] K. Kato, "Ultrawide-band/high-frequency photodetectors," *IEEE Transactions on Microwave Theory and Techniques*, vol. 47, pp. 1265-81, 1999.
- [67] T. Nagatsuma, "Generating Millimeter and Terahertz Waves," *IEEE Microwave Magazine*, vol. 10, pp. 64-74, Jun 2009.
- [68] F. D. Paolo, *Networks and Devices Using Planar Transmission Lines*: CRC Press LLC, 2000.
- [69] D. Zhengwei, G. Ke, J. S. Fu, F. Zhenghe, and G. Baoxin, "CAD models for asymmetrical, elliptical, cylindrical, and elliptical cone coplanar strip lines," *IEEE Transactions on Microwave Theory and Techniques*, vol. 48, pp. 312-16, 2000.
- [70] I. S. Gregory, W. R. Tribe, B. E. Cole, M. J. Evans, E. H. Linfield, A. G. Davies, and M. Missous, "Resonant dipole antennas for continuous-wave terahertz photomixers," *Applied Physics Letters*, vol. 85, pp. 1622-4, 2004.
- [71] I. S. Gregory, C. Baker, W. R. Tribe, I. V. Bradley, M. J. Evans, E. H. Linfield, A. G. Davies, and M. Missous, "Optimization of photomixers and antennas for continuous-wave terahertz emission," *IEEE Journal of Quantum Electronics*, vol. 41, pp. 717-728, 2005.
- [72] M. Tani, O. Morikawa, S. Matsuura, and M. Hangyo, "Generation of terahertz radiation by photomixing with dual- and multiple-mode lasers," *Semiconductor Science and Technology*, vol. 20, pp. 151-63, 2005.
- [73] E. R. Brown, K. A. McIntosh, K. B. Nichols, and C. L. Dennis, "Photomixing up to 3.8 THz in low-temperature-grown GaAs," *Applied Physics Letters*, vol. 66, pp. 285-7, 1995.
- [74] S. Verghese, K. A. McIntosh, and E. R. Brown, "Highly tunable fiber-coupled photomixers with coherent terahertz output power," *IEEE Transactions on Microwave Theory and Techniques*, vol. 45, pp. 1301-9, 1997.
- [75] HFSS, www.ansoft.com.
- [76] R. Appleby and H. B. Wallace, "Standoff Detection of Weapons and Contraband in the 100 GHz to 1 THz Region," *Antennas and Propagation, IEEE Transactions on*, vol. 55, pp. 2944-2956, 2007.
- [77] E. Abbe, "Beiträge zur Theorie des Mikroskops und der mikroskopischen Wahrnehmung," *Archiv für Mikroskopische Anatomie*, vol. 9, pp. 413-418, 1873.
- [78] D. R. Gagnon, "Highly sensitive measurements with a lens-focused reflectometer," Boston, MA, USA, 1991, pp. 1017-18.
- [79] P. F. Goldsmith, C. T. Hsieh, G. R. Huguenin, J. Kapitzky, and E. L. Moore, "Focal plane imaging systems for millimeter wavelengths," *IEEE Transactions on Microwave Theory and Techniques*, vol. 41, pp. 1664-75, 1993.
- [80] G. M. Rebeiz, "Millimeter-wave and terahertz integrated circuit antennas," *Proceedings of the IEEE*, vol. 80, pp. 1748-70, 1992.
- [81] D. F. Filipovic, S. S. Gearhart, and G. M. Rebeiz, "Double-slot antennas on extended hemispherical and elliptical silicon dielectric lenses," *IEEE Transactions on Microwave Theory and Techniques*, vol. 41, pp. 1738-49, 1993.

- [82] S. Enoch, G. Tayeb, P. Sabouroux, N. Guerin, and P. Vincent, "A metamaterial for directive emission," *Physical Review Letters*, vol. 89, pp. -, Nov 18 2002.
- [83] *Web Page*, http://en.wikipedia.org/wiki/Catadioptric_system.
- [84] A. V. Boriskin, S. V. Boriskina, and A. I. Nosich, "Exact near-fields of the dielectric lenses for sub-mm wave receivers," Munich, Germany, 2003, pp. 65-8.
- [85] J. B. Pendry and S. A. Ramakrishna, "Near-field lenses in two dimensions," *Journal of Physics: Condensed Matter*, vol. 14, pp. 8463-79, 2002.
- [86] X. Wu, G. V. Eleftheriades, and T. E. Van Deventer-Perkins, "Design and characterization of single- and multiple-beam MM-wave circularly polarized substrate lens antennas for wireless communications," *IEEE Transactions on Microwave Theory and Techniques*, vol. 49, pp. 431-441, 2001.
- [87] P. Uhd Jepsen and S. R. Keiding, "Radiation patterns from lens-coupled terahertz antennas," *Optics Letters*, vol. 20, pp. 807-9, 1995.
- [88] M. J. M. Van der Vorst, P. J. I. De Maagt, A. Neto, A. L. Reynolds, R. M. Heeres, W. Luinge, and M. H. A. J. Herben, "Effect of internal reflections on the radiation properties and input impedance of integrated lens antennas - Comparison between theory and measurements," *IEEE Transactions on Microwave Theory and Techniques*, vol. 49, pp. 1118-1125, 2001.
- [89] A. Nato, L. Borselli, S. Maci, and P. J. I. de Maagt, "Input impedance of integrated elliptical lens antennas," *IEE Proceedings-Microwaves, Antennas and Propagation*, vol. 146, pp. 181-6, 1999.
- [90] W. B. Dou and E. K. N. Yung, "FDTD simulation for the focusing property of extended hemispherical lens as receiving antenna," *International Journal of Infrared and Millimeter Waves*, vol. 21, pp. 2077-86, 2000.
- [91] D. F. Filipovic, G. V. Eleftheriades, and G. M. Rebeiz, "Off-axis imaging properties of substrate lens antennas," Tucson, AZ, USA, 1995, pp. 106-13.
- [92] CST, www.cst.com.
- [93] A. Monorchio, A. R. Bretones, R. Mittra, G. Manara, and R. G. Martin, "A hybrid time-domain technique that combines the finite element, finite difference and method of moment techniques to solve complex electromagnetic problems," *IEEE Transactions on Antennas and Propagation*, vol. 52, pp. 2666-2674, Oct 2004.
- [94] Dupont, www.dupont.com.
- [95] Macor, www.corning.com.
- [96] Y. J. Gao, A. Lauer, Q. M. Ren, and I. Wolff, "Calibration of electric coaxial near-field probes and applications," *IEEE Transactions on Microwave Theory and Techniques*, vol. 46, pp. 1694-1703, Nov 1998.
- [97] W. Mertin, "Two-dimensional field mapping of monolithic microwave integrated circuits using electrooptic sampling techniques," *Optical and Quantum Electronics*, vol. 28, pp. 801-817, Jul 1996.
- [98] J. Vukusic, T. Bryllert, T. A. Emadi, M. Sadeghi, and J. Stake, "A 0.2-W Heterostructure Barrier Varactor Frequency Tripler at 113 GHz," *Electron Device Letters, IEEE*, vol. 28, pp. 340-342, 2007.

-
- [99] K. J. Siebert, H. Quast, R. Leonhardt, T. Löffler, M. Thomson, T. Bauer, H. G. Roskos, and S. Czasch, "Continuous-wave all-optoelectronic terahertz imaging," *Applied Physics Letters*, vol. 80, pp. 3003-3005, 2002.
- [100] A. Csendes, V. Szekely, and M. Rencz, "Thermal mapping with liquid crystal method," *Microelectronic Engineering*, vol. 31, pp. 281-290, Feb 1996.
- [101] *Web Page*, http://en.wikipedia.org/wiki/Electromagnetic_spectrum.
- [102] T. Nozokido, J. Bae, and K. Mizuno, "Scanning near-field millimeter-wave microscopy using a metal slit as a scanning probe," *Microwave Theory and Techniques, IEEE Transactions on*, vol. 49, pp. 491-499, 2001.
- [103] A. W. M. Lee, B. S. Williams, S. Kumar, Q. Hu, and J. L. Reno, "Real-time imaging using a 4.3-THz quantum cascade laser and a 320 \times 240 microbolometer focal-plane array," *IEEE Photonics Technology Letters*, vol. 18, pp. 1415-1417, 2006.
- [104] T. Löffler, K. J. Siebert, H. Quast, N. Hasegawa, G. Loata, R. Wipf, T. Hahn, M. Thomson, R. Leonhardt, and H. G. Roskos, "All-optoelectronic continuous-wave terahertz systems," *Philosophical Transactions of the Royal Society London, Series A (Mathematical, Physical and Engineering Sciences)*, vol. 362, pp. 263-81, 2004.
- [105] K. B. Cooper, R. J. Dengler, N. Llombart, T. Bryllert, G. Chattopadhyay, E. Schlecht, J. Gill, C. Lee, A. Skalare, I. Mehdi, and P. H. Siegel, "Penetrating 3-D Imaging at 4-and 25-m Range Using a Submillimeter-Wave Radar," *IEEE Transactions on Microwave Theory and Techniques*, vol. 56, pp. 2771-2778, Dec 2008.
- [106] C. am Weg, W. von Spiegel, R. Henneberger, R. Zimmermann, T. Loeffler, and H. Roskos, "Fast Active THz Cameras with Ranging Capabilities," *Journal of Infrared, Millimeter and Terahertz Waves*.
- [107] A. J. Miller, A. Luukanen, and E. N. Grossman, "Micromachined antenna-coupled uncooled microbolometers for terahertz imaging arrays," *Terahertz for Military and Security Applications II*, vol. 5411, pp. 18-24, 2004.
- [108] A. Luukanen, A. J. Miller, and E. N. Grossman, "Active millimeter-wave video rate imaging with a staring 120-element microbolometer array," *Radar Sensor Technology Viii and Passive Millimeter-Wave Imaging Technology Vii*, vol. 5410, pp. 195-201, 2004.
- [109] R. Appleby, "Passive millimetre-wave imaging and how it differs from terahertz imaging," *Philosophical Transactions of the Royal Society of London Series a-Mathematical Physical and Engineering Sciences*, vol. 362, pp. 379-392, 2004.
- [110] D. M. Mittleman, S. Hunsche, L. Boivin, and M. C. Nuss, "T-ray tomography," *Optics Letters*, vol. 22, pp. 904-906, Jun 15 1997.
- [111] N. Karpowicz, H. Zhong, J. Z. Xu, K. I. Lin, J. S. Hwang, and X. C. Zhang, "Comparison between pulsed terahertz time-domain imaging and continuous wave terahertz imaging," *Semiconductor Science and Technology*, vol. 20, pp. S293-S299, Jul 2005.
- [112] B. T. Rosner and D. W. van der Weide, "High-frequency near-field microscopy," *Review of Scientific Instruments*, vol. 73, pp. 2505-2525, 2002.
- [113] A. Tessmann, "220-GHz metamorphic HEMT amplifier MMICs for high-resolution imaging applications," *IEEE Journal of Solid-State Circuits*, vol. 40, pp. 2070-2076, 2005.

- [114] F. Rodriguez-Morales, K. S. Yngvesson, R. Zannoni, E. Gerecht, D. Z. Gu, X. Zhao, N. Wadefalk, and J. J. Nicholson, "Development of integrated HEB/MMIC receivers for near-range terahertz imaging," *IEEE Transactions on Microwave Theory and Techniques*, vol. 54, pp. 2301-2311, Jun 2006.
- [115] S. E. Gunnarsson, N. Wadefalk, J. Svedin, S. Cherednichenko, I. Angelov, H. Zirath, I. Kallfass, and A. Leuther, "A 220 GHz single-chip receiver MMIC with integrated antenna," *IEEE Microwave and Wireless Components Letters*, vol. 18, pp. 284-286, Apr 2008.
- [116] *Web Page*, http://en.wikipedia.org/wiki/Point_spread_function.
- [117] J. T. Bushberg, J. A. Seibert, E. M. L. Jr., and J. M. Boone, *The Essential Physics of Medical Imaging (2nd Edition)*, 2003.
- [118] C. Gabriel, S. Gabriel, and E. Corthout, "The dielectric properties of biological tissues .1. Literature survey," *Physics in Medicine and Biology*, vol. 41, pp. 2231-2249, Nov 1996.
- [119] S. Gabriel, R. W. Lau, and C. Gabriel, "The dielectric properties of biological tissues .2. Measurements in the frequency range 10 Hz to 20 GHz," *Physics in Medicine and Biology*, vol. 41, pp. 2251-2269, Nov 1996.
- [120] A. Dobroiu, M. Yamashita, Y. N. Ohshima, Y. Morita, C. Otani, and K. Kawase, "Terahertz imaging system based on a backward-wave oscillator," *Applied Optics*, vol. 43, pp. 5637-5646, Oct 20 2004.
- [121] F. Koyama, "Recent Advances of VCSEL Photonics," *Journal of Lightwave Technology*, vol. 24, pp. 4502-4513, 2006.
- [122] K. O. Kenneth, "Affordable terahertz electronics," *Microwave Magazine, IEEE*, vol. 10, pp. 113-116, 2009.

Acknowledgement

First and foremost, I would like to thank my supervisor, Prof. Jan Stake, for his constant support, encouragement, minute supervision, great mentorship and for giving me the opportunity to perform this work. I am thankful to him for all the fruitful discussions and suggestions which have always been exceptionally motivating. I would also like to express my heartiest appreciation to my co-supervisor, Dr. Josip Vukusic, for his extraordinary guidance, inspiration, support and patience.

I am grateful to Dr. Serguei Cherednichenko for providing me guidance and encouragement. I am indebted to Dr. Hans Hjelmgren for all the fruitful discussions on numerous occasions. I am grateful to Dr. Erik Kollberg for helpful discussions and providing comments on this thesis. I would like to express my gratitude to Prof. Spartak Gevorgian for his support. I am thankful to Dr. Vessen Vassilev for helpful discussions.

I would like to thank my dearest friends and colleagues Peter Sobis, Martin Norling, Aik Yean Tang, John Berge, Vladimir Drakinskiy, Huan Zhao, Omid Habibpour, Wei Wei and others.

I would also like to acknowledge and extend my heartiest gratitude to Andres Olausson, Jan Andersson, Catharina Forssén and Ann-Marie Frykestig.

Thank you all for creating such an inspiring and comforting environment.

I am grateful to my parents, Badal Banik and Gayatri Banik, for all the sacrifices they made. I would like to thank my wife, Tanuja Banik, for being supportive, patient and caring.

This work was financially supported by the Swedish Foundation of Strategic Research (SSF) and VINNOVA.

